



**fire**  
cci


---

## ESA Climate Change Initiative – Fire\_cci D5.1 Climate Assessment Report (CAR)

---

<b>Project Name</b>	ECV Fire Disturbance: Fire_cci Phase 2
<b>Contract N°</b>	4000115006/15/I-NB
<b>Issue Date</b>	16/11/2018
<b>Version</b>	1.4
<b>Author</b>	Pierre Laurent, M. Vanesa Moreno, Florent Mouillot, Swanni Alvarado, Joana M.P. Nogueira, Chao Yue, Philippe Ciais
<b>Document Ref.</b>	Fire_cci_D5.1_CAR_v1.4
<b>Document type</b>	Public

*To be cited as: P. Laurent, M. V. Moreno, F. Mouillot, S. Alvarado, J.M.P. Nogueira, C. Yue, P. Ciais (2018) ESA CCI ECV Fire Disturbance: D5.1. Climate Assessment Report, version 1.4. Available at: <http://www.esa-fire-cci.org/documents>*

	<b>Fire_cci</b> <b>Climate Assessment Report</b>	Ref.:	Fire_cci_D5.1_CAR_v1.4			
		Issue	1.4	Date	16/11/2018	
				Page	2	

## Project Partners

Prime Contractor/ Scientific Lead & Project Management	UAH – University of Alcalá (Spain)
Earth Observation Team	UAH – University of Alcalá (Spain)
	EHU – University of the Basque Country (Spain)
	UL – University of Leicester (United Kingdom)
	UCL – University College London (United Kingdom)
	ISA – School of Agriculture, University of Lisbon (Portugal)
System Engineering	BC – Brockmann Consult (Germany)
Climate Research Group	MPIC – Max Planck Institute for Chemistry (Germany)
	IRD - Research Institute for Development (France)
	LSCE - Climate and Environmental Sciences Laboratory (France)
	VUA - Vrije Universiteit Amsterdam (Netherlands)



## Distribution

Affiliation	Name	Address	Copies
ESA	Stephen Plummer (ESA)	stephen.plummer@esa.int	electronic copy
Project Team	Emilio Chuvieco (UAH)	emilio.chuvieco@uah.es	electronic copy
	M. Lucrecia Pettinari (UAH)	mlucaresia.pettinari@uah.es	
	Joshua Lizundia (UAH)	joshua.lizundia@uah.es	
	Gonzalo Otón (UAH)	gonzalo.oton@uah.es	
	Mihai Tanase (UAH)	mihai.tanase@uah.es	
	Miguel Ángel Belenguer (UAH)	miguel.belenguer@uah.es	
	Aitor Bastarrika (EHU)	aitor.bastarrika@ehu.es	
	Ekhi Roteta (EHU)	ekhi.roteta@gmail.com	
	Kevin Tansey (UL)	kjt7@leicester.ac.uk	
	Marc Padilla Parellada (UL)	mp489@leicester.ac.uk	
	James Wheeler (UL)	jemw3@leicester.ac.uk	
	Philip Lewis (UCL)	ucfalew@ucl.ac.uk	
	José Gómez Dans (UCL)	j.gomez-dans@ucl.ac.uk	
	James Brennan (UCL)	james.brennan.11@ucl.ac.uk	
	Jose Miguel Pereira (ISA)	jmocpereira@gmail.com	
	Duarte Oom (ISA)	duarte.oom@gmail.com	
	Manuel Campagnolo (ISA)	mlc@isa.ulisboa.pt	
	Thomas Storm (BC)	thomas.storm@brockmann-consult.de	
	Johannes Kaiser (MPIC)	j.kaiser@mpic.de	
	Angelika Heil (MPIC)	a.heil@mpic.de	
	Florent Mouillot (IRD)	florent.mouillot@cefe.cnrs.fr	
	M. Vanesa Moreno (IRD)	mariavanesa.morenodominguez @cefe...	
	Philippe Ciaï (LSCE)	philippe.ciaï@lsce.ipsl.fr	
Chao Yue (LSCE)	chaoyuejoy@gmail.com		
Pierre Laurent (LSCE)	pierre.laurent@lsce.ipsl.fr		
Guido van der Werf (VUA)	guido.vander.werf@vu.nl		
Ioannis Bistinas (VUA)	i.bistinas@vu.nl		



## Summary

This document is the version 1.4 of the Climate Assessment Report for the Fire\_cci project. It presents the methodology used to create the Fire\_cci fire patch database from the MERIS Fire\_cci v4.1 (FireCCI41), MODIS Fire\_cci v5.0 (FireCCI50), MODIS Fire\_cci v5.1 (FireCCI51), MCD45A1 collection 5, MCD64A1 collection 6 Global Burned Area (BA) products, and from the SFD v1.0 (FireCCISFD10) product for Africa. It includes a comparison at the regional and continental scales, and an intercomparison between the global databases. The report also focuses on trait-based approach and beta diversity, and on finding relationships between climatic variables and fire morphological features at the global scale.

	Affiliation/Function	Name	Date
<b>Prepared</b>	LSCE	Pierre Laurent	16/11/2018
	IRD	M. Vanesa Moreno	
	IRD	Florent Mouillot	
	LSCE	Swanni Alvarado	
	LSCE	Chao Yue	
	LSCE	Philippe Ciais	
<b>Reviewed</b>	UAH – Project Manager	M. Lucrecia Pettinari	16/11/2018
<b>Authorized</b>	UAH - Science Leader	Emilio Chuvieco	16/11/2018
<b>Accepted</b>	ESA - Technical Officer	Stephen Plummer	

This document is not signed. It is provided as an electronic copy.

## Document Status Sheet

Issue	Date	Details
<b>1.0</b>	31/03/2017	First Document Issue
<b>1.1</b>	30/09/2017	Revised document, including answers to the comments on CCI-FIRE-EOPS-MM-17-0045, new analysis, and the inclusion and analysis of Sentinel-2 SFD BA information.
<b>1.2</b>	23/04/2018	Revised document, including answers to the comments on CCI-FIRE-EOPS-MM-18-0004, and new analysis of the MODIS Fire_cci v5.0 product.
<b>1.3</b>	22/06/2018	Revised document, including answers to the comments on CCI-FIRE-EOPS-MM-18-0159
<b>1.4</b>	16/11/2018	Update of the document

## Document Change Record

Issue	Date	Request	Location	Details
1.1	30/09/2017	ESA, LSCE-IRD	Summary Figures 3 and 4 Section 3.1 Section 3.2, Section 4, Conclusion	Update of the summary of the document. Figures updated to include MCD64A1. Minor changes in the text The sections have been expanded with new analyses and a new datasets. The conclusions were updated to include the new analyses performed.
1.2	23/04/2018	ESA, LSCE-IRD	Summary Section 1 Section 2 Section 3 Section 3.1 Section 3.2	Update of the summary of the document. Small changes in the text to address MODIS Fire_cci v5.0. Parameter units corrected, and ellipse main features expanded. Text expanded Small changes in the text. The analysis was changed to include



			Section 4.1 Section 4.2.1 Section 4.2.2 Section 4.4 Section 6	MCD64A1 C6 instead of MCD45A1 C5. The figures and text were updated. Small changes in the text. Text updated (was previously Section 4.2) New section added Added comparison of SFD and MCD64A1 Conclusions updated
1.3	22/06/2018	ESA, LSCE-IRD	All document Figure 1 Figure 5 Section 3.2	Inclusion of acronyms of the products. Figure updated Caption updated Clarification added to the first paragraph.
1.4	16/11/2018	LSCE-IRD	All document Sections 3.3, 5.3 Sections 4.2.1, 4.4 Section 4.2.2 Previous Sections 5.1 and 5.2 Section 6	Inclusion of FireCCI51 analysis New sections added Small changes in the text Text updated to include FireCCI51 Sections replaced by new Section 5.1  Text updated

## **Table of Contents**

1. Introduction.....	10
2. Methodology.....	11
3. Assessing the conservation of fire patch morphological features across fire products	14
3.1. At the local scale in the Brazilian Savanna .....	16
3.2. At the continental scale in North America .....	18
3.3. At the global scale .....	32
4. Uncertainty on fire patch morphology: comparing the assemblage of patches between different BA products and between cut-off thresholds for a given BA product.....	40
4.1. Morphological traits and power law maps .....	40
4.2. Comparison between BA global products .....	43
4.2.1. Comparison between FireCCI41, MCD45A1 and MCD64A1.....	43
4.2.2. Comparison between FireCCI50, FireCCI51 and MCD64A1.....	47
4.3. Influence of the cut-off on fire morphological traits .....	51
4.4. Fire patch morphological traits with the FireCCISFD10 BA product.....	52
5. Looking for relationships between different driving factors and fire size.....	56
5.1. Relationship between fire intensity and fire size.....	56
5.2. Influence of wind speed and wind orientation on fire patch geometry and orientation.....	63
5.3. Burned Pixel-derived fire patch morphology as an indicator of spreading process and their environmental drivers.....	64
5.3.1. Fire patch pattern across continents.....	66
5.3.2. Drivers of fire patch pattern.....	67
6. Conclusion .....	69
7. References.....	70
8. Annex 1: Acronyms and abbreviations.....	74





**List of Tables**

**Table 1:** Descriptions of global burned area data used for fire patch studies ..... 17  
**Table 2:** Description of the morphology of fire patches features (updated from Nogueira et al. 2016) ..... 65

**List of Figures**

**Figure 1:** Example of fire patch reconstruction. Figures a to d show the fire patches calculated from individual burned pixels, with a cut-off of 3, 5, 9 and 14, for MCD64A1 in a region of northern hemisphere Africa. Continuous areas with the same colour indicate the same fire patch. Figure e shows the burn dates of the pixels (in days). Figures f and g show examples of the Standard Deviation Ellipses (SDE, dark blue) for three patches with a cut-off of 5 and 14. The half-axes and azimuthal angle are displayed in red..... 12  
**Figure 2:** Flowchart of the fire patches processing (from Nogueira et al. 2016)..... 12  
**Figure 3:** Difference between the areas computed from the ellipse and from pixel, normalized by the area of the ellipse, with respect to ellipse area. The left plot displays the result for the MERIS Fire\_cci product, the centre one for MCD45A1 collection 5 and the right one for MCD64A1 collection 6..... 13  
**Figure 4:** Same as Figure 3, but with perimeter to area ratio. The discontinuities arise from the fact that perimeter to area ratio for small patches will take discrete values. ... 14  
**Figure 5:** Example of a 3.75×3.75° tile in Africa, which illustrates the removal of the 0.625° bands on the borders of the tile. The patches located on the borders are added to the database when the neighbouring tiles are processed, to avoid double-counting. .... 14  
**Figure 6:** Illustration of a theoretical 2-D fire ellipse (from Alexander 1985)..... 15  
**Figure 7:** Illustration of the modification of patch morphological features because of commission (in red) and omission errors (in grey). ..... 16  
**Figure 8:** Administrative map of Brazil..... 17  
**Figure 9:** Coefficients of determination (R) and regression slope (s) (Y axis) as a function of patch size (in ha, X axis) for patch size, eccentricity, perimeter and patch orientation (Θ), for the different BA products. (R) solid line: coefficient of determination; (s) dotted line: slope. .... 18  
**Figure 10:** Adapted example of three different functional diversity indices in functional space from Villéger et al. (2008): Functional Evenness (FEve), Functional Divergence (FDiv), Functional Richness (FRic). ..... 20  
**Figure 11:** Conceptual framework for the decomposition of functional β-diversity from Villéger et al. (2013) with theoretical examples of complete trait overlap (b), partial trait inclusion (e), partial overlap (c, f) and total mismatch (d,g). ..... 21  
**Figure 12:** Example of Functional Richness (FRic) and Functional Dispersion (FDis) obtained from FireCCI41 cut-off 14 (Left) and GeoMAC\_CNFD forest service (Right). ..... 22  
**Figure 13:** Bivariate relationships between Functional Richness (FRic, top) and Functional Dispersion (FDis, bottom) obtained from GeoMAC\_CNFD forest service (x-axis) and FireCCI41 cut-off 14 (y-axis). ..... 23  
**Figure 14:** Example of Functional Richness (FRic) and Functional Dispersion (FDis) obtained from MCD64A1 collection 6 cut-off 14 (Left) and GeoMAC\_CNFD forest service (Right). ..... 24



**Figure 15:** Bivariate relationships between Functional Richness (FRic, top) and Functional Dispersion (FDis, bottom) obtained from GeoMAC\_CNFD forest service (x-axis) and MCD64A1 collection 6 (y-axis). ..... 24

**Figure 16:** Functional  $\beta$ -diversity ( $\beta$ -div) maps for North America obtained from GeoMAC\_CNFD forest service and FireCCI41 cut-offs 3, 5, 9 and 14. .... 25

**Figure 17:** Functional  $\beta$ -diversity ( $\beta$ -div) maps for North America obtained from MERIS Fire\_cci v4.1 (FireCCI41) and MCD64A1 collection 6 cut-off 3, 5, 9 and 14. 26

**Figure 18:** Bivariate relationships between functional  $\beta$ -diversity ( $\beta$ -div) obtained from MERIS Fire\_cci v4.1 (FireCCI41) and MCD64A1 collection 6 cut-off 3, 5, 9 and 14. 26

**Figure 19:** Interpretation of colour composition of functional  $\beta$ -diversity ( $\beta$ -div), functional Turnover (Turn) and functional Nestedness (Nest) with theoretical examples of partial trait inclusion (e), partial overlap (c, f), total mismatch (d, g) and total match (b) from Vileger et al. (2013). High values of Nest are under the black line, while low values of Nest over the black line..... 27

**Figure 20:** Colour composition of functional  $\beta$ -diversity ( $\beta$ -div), functional Turnover (Turn) and functional Nestedness (Nest) obtained from GeoMAC\_CNFD forest service and MERIS Fire\_cci v4.1 (FireCCI41) cut-off 14. .... 28

**Figure 21:** Colour composition of functional  $\beta$ -diversity ( $\beta$ -div), functional Turnover (Turn) and functional Nestedness (Nest) obtained from MERIS Fire\_cci v4.1 (FireCCI41) and MCD64A1 collection 6 cut-off 3. .... 29

**Figure 22:** Example of (c) theoretical example of partial overlap from Vileger et al. 2013 obtained from MERIS Fire\_cci v4.1 (FireCCI41) (Blue) and MCD64A1 collection 6 (Red) cut-off 3 for a tile with latitude = 52 and longitude = -93. FireCCI41 + MCD64A1 collection 6 white convex hull.  $\beta$ -diversity ( $\beta$ -div) = 0.597, functional Turnover (Turn) = 0.466 and functional Nestedness (Nest) = 0.1. .... 29

**Figure 23:** Example of functional diversity indices obtained from MERIS Fire\_cci v4.1 (FireCCI41) (Blue) and MCD64A1 collection 6 (Red) cut-off 3 for a tile with latitude = 52 and longitude = -93. Functional Richness (FRic) and Functional Dispersion (FDis). ..... 30

**Figure 24:** Example of (e) theoretical example partial trait inclusion from Vileger et al. 2013 obtained from MERIS Fire\_cci v4.1 (FireCCI41) (Blue) and MCD64A1 collection 6 (Red) cut-off 3 for a tile with latitude = 27 and longitude = -81. FireCCI41 + MCD64A1 collection 6 white convex hull.  $\beta$ -diversity ( $\beta$ -div) = 0.278, functional Turnover (Turn) = 0.230 and functional Nestedness (Nest) = 0.049. .... 31

**Figure 25:** Example of functional diversity indices obtained from MERIS Fire\_cci v4.1 (FireCCI41) (Blue) and MCD64A1 collection 6 (Red) cut-off 3 for a tile with latitude = 27 and longitude = -81. Functional Richness (FRic) and Functional Dispersion (FDis). ..... 31

**Figure 26:** Functional Richness (FRic; Left) and Functional Dispersion (FDis; Right) obtained from MERIS Fire\_cci v4.1 (FireCCI41) cut-off 3, 5, 9 and 14..... 33

**Figure 27:**  $R^2$  (p-value < 0.001) of the bivariate relationship of Functional Richness (FRic; Left) and Functional Dispersion (FDis; Right) obtained from MERIS Fire\_cci v4.1 (FireCCI41) at different cut-offs 3, 5, 9 and 14..... 33

**Figure 28:** Functional  $\beta$ -diversity ( $\beta$ -div) maps at global scale obtained from MERIS Fire\_cci v4.1 (FireCCI41) cut-offs 3, 5, 9 and 14. .... 34

**Figure 29:** Colour composition of functional  $\beta$ -diversity ( $\beta$ -div), functional Turnover (Turn) and functional Nestedness (Nest) obtained from MERIS Fire\_cci v4.1 (FireCCI41) cut-off 5-9. .... 34



**Figure 30:** Functional Richness (FRic; Left) and Functional Dispersion (FDis; Right) obtained from MCD64A1 collection 6 cut-off 3, 5, 9 and 14. .... 35

**Figure 31:**  $R^2$  (p-value < 0.001) of the bivariate relationship of Functional Richness (FRic; Right) Functional Dispersion (FDis; Left) obtained from MCD64A1 collection 6 at different cut-offs 3, 5, 9 and 14. .... 36

**Figure 32:** Functional  $\beta$ -diversity ( $\beta$ -div) maps at global scale obtained from MCD64A1 collection 6 cut-offs 3, 5, 9 and 14. .... 36

**Figure 33:** Colour composition of functional  $\beta$ -diversity ( $\beta$ -div), functional Turnover (Turn) and functional Nestedness (Nest) obtained from MCD64A1 collection 6 cut-off 9-14. .... 37

**Figure 34:**  $R^2$  (p-value < 0.001) of the bivariate relationship of Functional Richness (FRic; Left) Functional Dispersion (FDis; Right) obtained from MERIS Fire\_cci v4.1 (FireCCI41; Top) and MCD64A1 collection 6 (Left) at different cut-offs 3, 5, 9 and 14. .... 38

**Figure 35:** Functional  $\beta$ -diversity ( $\beta$ -div) maps at global scale obtained from MERIS Fire\_cci v4.1 (FireCCI41) cut-offs 3 (Left) and 5 (Right) and MCD64A1 collection 6 cut-offs 3, 5, 9 and 14. .... 38

**Figure 36:** Functional  $\beta$ -diversity ( $\beta$ -div) maps at global scale obtained from MERIS Fire\_cci v4.1 (FireCCI41) cut-offs 9 (Left) and 14 (Right) and MCD64A1 collection 6 cut-offs 3, 5, 9 and 14. .... 39

High  $\beta$ -div located in tropical Asia, temperate and boreal forests as well as in the Australian savannas, was driven by a high Turn (e.g dark purplish grid cells in Figure 37), so that the fire trait hyper-volumes tend to only partly overlap. High  $\beta$ -div located in the tropical forest and savannas in the south hemisphere, was driven by a high Nest (e.g dark bluish grid cells in Figure 38), suggesting that the fire trait hyper-volume from one sensor is included in the other, with missing some fire types. .... 39

**Figure 39:** Colour composition of functional  $\beta$ -diversity ( $\beta$ -div), functional Turnover (Turn) and functional Nestedness (Nest) obtained from FireCCI41 cut-off 14 and MCD64A1 collection 6 cut-off 5. .... 39

**Figure 40:** Example of a power law fit ..... 41

**Figure 41:** Difference between  $\beta$  parameter computed from  $A_{\text{ellipse}}$  and from  $A_{\text{pixel}}$  from FireCCI41 (top), MCD45A1 collection 5 (middle) and MCD64A1 collection 6 (bottom). .... 42

**Figure 42:** Fire density ( $\text{km}^{-2}$ ) for FireCCI41 (top left), and MCD45A1 collection 5 (top right). The difference between the two products is displayed for the years 2005-2011. 44

**Figure 43:** Same as **Figure 42**, with the MCD64A1 collection 6 product instead of MCD45A1 collection 5. .... 44

**Figure 44:** Map of  $\beta$  parameter for the FireCCI41 (2005-2011) product (top left) and its uncertainty (middle left), for the MCD45A1 collection 5 product (2000-2016) (top right) and its uncertainty (middle right), the difference between the two products (bottom right) and the level of agreement between the two products (bottom right). The power law is only computed when there are more than 10 detected individual fires in the cell. .... 45

**Figure 45:** Same as **Figure 44**, with MCD64A1 collection 6 instead of MCD45A1 collection 5. .... 46

**Figure 46:** Shape Index for the FireCCI41 product (top left), for the MCD45A1 collection 5 product (top right). .... 47

**Figure 47:** Same as **Figure 47**, with MCD64A1 collection 6. .... 47



**Figure 48:** Same as **Figure 42** and **Figure 43**, with the FireCCI50 instead of FireCCI41. .... 48

**Figure 49:** Same as **Figure 46** and **Figure 47**, with FireCCI50 instead of FireCCI41. The 107 ha cut is applied. .... 48

**Figure 50:** Same as **Figure 44** and **Figure 45**, with FireCCI50 instead of FireCCI41. 49

**Figure 51:** Same as Figure 41 and Figure 42, with FireCCI51 instead of FireCCI41... 50

**Figure 52:** Same as Figure 45 and Figure 46, with FireCCI51 instead of FireCCI41. The 107 ha cut is applied. .... 50

**Figure 53:** Same as Figure 31 and Figure 32, with FireCCI51 instead of FireCCI41... 51

**Figure 54:** Averaged values of the  $\beta$  parameter (top left), Shape Index (top right) and Ellipse Ratio (bottom) for MCD45A1 collection 5 (blue), MCD64A1 collection 6 (green) and FireCCI41 (red). The results for 4 cut-off values are displayed. .... 52

**Figure 55:** Fire density ( $\text{km}^{-2}$ ) for the FireCCISFD10 BA product (from January to September 2016)..... 53

**Figure 56:** Beta parameter for the FireCCISFD10 BA product (from January to September 2016)..... 53

**Figure 57:** Shape Index for the FireCCISFD10 BA product (from January to September 2016)..... 53

**Figure 58:** Ellipse Ratio for the FireCCISFD10 BA product (from January to September 2016)..... 54

**Figure 59:** Fire density ( $\text{km}^{-2}$ ) for the FireCCISFD10 product (top left), MCD64A1 collection 6 (top right). The difference between the two products is displayed during the time span covered by the FireCCISFD10 product. For the sake of product inter-comparison, only fires bigger than 107 ha are displayed. .... 54

**Figure 60:** Map of  $\beta$  parameter for the FireCCISFD10 product (top left) and its uncertainty (middle left), for the MCD64A1 collection 6 product (top right) and its uncertainty (middle right). The difference between the two products (bottom left) and the level of agreement between the two products (bottom right) are also displayed. The power law is only computed when there are more than 10 detected individual fires in the cell. .... 55

**Figure 61:** Maps of Shape Index for the FireCCISFD10 product (left) and the MCD64A1 Collection 6 product (right). Only fires bigger than 107 ha have been used to compute the maps. .... 55

**Figure 62:** Maps of Ellipse Ratio for the FireCCISFD10 product (top left) and the MCD64A1 Collection 6 product (top right). The difference between the two products (bottom left) and the level of agreement (bottom right) are also displayed. Only fires bigger than 107 ha have been used to compute the maps..... 56

**Figure 63:** Median fire size (from MCD64A1,  $\text{co}=14$  days) vs fire intensity from the MCDML14 datasets. The error bars show the 25<sup>th</sup> and 75<sup>th</sup> percentiles of fire size. The colour of the dots and error bars represent the median burn date of fire patches in each bins. The background bars (associated with the right scale on the plots) represent the histograms of the number of fire patches in each FRP bins. .... 57

**Figure 64:** Same as **Figure 63**, with  $\text{co}=3$  days..... 58

**Figure 65:** Same as **Figure 63**, with FireCCI41 (2005-2011). .... 58

**Figure 66:** Same as **Figure 63**, with FireCCI41 (2005-2011) and  $\text{co}=3$  days..... 59

**Figure 67:** Same as **Figure 63**, with FireCCI50 and  $\text{co}=5$  days. .... 59

**Figure 68:** Same as **Figure 63**, with FireCCI51 and  $\text{co}=5$  days. .... 60

**Figure 69:** Values of  $\beta_{\text{begin}}$ ,  $\beta_{\text{middle}}$  and  $\beta_{\text{end}}$  for MCD64A1 ( $\text{co}=14$  days), and differences between  $\beta_{\text{begin}}$  and  $\beta_{\text{end}}$ . .... 61



**Figure 70:** Values of  $\beta_{begin}$ ,  $\beta_{middle}$  and  $\beta_{end}$  for FireCCI41 (co=14 days), and differences between  $\beta_{begin}$  and  $\beta_{end}$ . ..... 61

**Figure 71:** Values of  $\beta_{begin}$ ,  $\beta_{middle}$  and  $\beta_{end}$  for FireCCI50 (co=5 days), and differences between  $\beta_{begin}$  and  $\beta_{end}$ . ..... 62

**Figure 72:** Values of  $\beta_{begin}$ ,  $\beta_{middle}$  and  $\beta_{end}$  for FireCCI51 (co=5 days), and differences between  $\beta_{begin}$  and  $\beta_{end}$ . ..... 62

**Figure 73:** Fire size (derived from the fitted ellipse) versus mean wind speed (in m.s<sup>-1</sup>) from the minimum BD to the maximum BD. .... 63

**Figure 74:** Correlation factor r between wind orientation and ellipse orientation. .... 64

**Figure 75:** Box-and-whisker plots of the distribution of the fire patch morphological features by GFED regions from the Global Fire Emissions Database (Ellis et al., 2010) and by Land cover from MODIS Land Cover Global product (MCD12C1) for 2012 (Friedl *et al.*, 2010). ..... 67

**Figure 76:** A. Box-and-whisker plot of theta angle of fire scars by GFED region. Red line cut the y-axis at 90°. B. Proportion of prevailing wind direction by GFED region. C. Model generalized additive model (GAM) fit of theta angle relationship with the prevailing wind direction across GFED regions. D. Box-and-whisker plot of ROSL (fire spread) by GFED region. E. Box-and-whisker plot of wind speed by GFED region. F. Model generalized additive model (GAM) fit of ROSL relationship with wind speed across GFED regions. .... 68

**Figure 77:** A. Relationship between ellipse ration and ROSL. B. Fractal dimension index variation in function of tree cover percent. .... 68





## 1. Introduction

Natural fires play an important role in the Earth system. The perturbation of vegetation dynamics through biomass burning and post-fire recovery (Bond et al. 2005) has an impact on the carbon cycle (Bond-Lamberty et al. 2007), and the various chemical emissions from wildfires (CO<sub>2</sub>, methane, etc.) (van der Werf et al. 2010) are susceptible to have significant impacts on the atmospheric radiative forcing balance and on human health. Those processes are then included in most of Dynamic Global Vegetation Models (DGVM) (Hantson et al. 2016). Understanding them is vital to produce reliable climatic forecasts of biosphere–atmosphere interactions, which are necessary to study future changes in the carbon cycle. At the same time, various global burned area (BA) products have been derived from remote sensing (Mouillot et al. 2014, Giglio et al. 2009, 2013, Chuvieco et al. 2016) in order to help model the key processes related to vegetation fires, and to verify if DGVMs are able to accurately reproduce global BA, fire seasonality and fire emissions.

Most of the fire modules simulate fire spread as a theoretical ellipse centred on the ignition point, where the elongation of the ellipse is proportional to the wind speed (Rothermel 1972). Burned area is usually estimated as the product of the number of fires times the area of the simulated ellipse. However, this method neglects the fact that fire propagation can be locally modified by wind orientation and topography gradient (Barros et al. 2012, 2013). Moreover, recent studies have shown that fire patch complexity is important to understand post-fire recovery, since remaining islands of living vegetation can accelerate the recolonization process after a fire (Roman-Cuesta et al. 2009, Oliveira et al. 2015). Regional analyses of fire shapes exist, but it has never been brought to a global scale. This new step is necessary in order to refine fire modules, and to allow for proper calibration of fire shape distribution in DGVM. This Climate Assessment Report focuses on the assessment of global fire patch databases from satellite Burned Area (BA) products and their subsequent use in climate research.

Two types of data sets can be used to characterize fire patches. The first type consists in information provided by Forest Agencies, where fire patches are directly observed and recorded either by sight, photography, helicopters or ground GPS; the second is burned area observation derived from satellite data. None of those data sets are perfect, as they exhibit different biases and different fire detection completeness. It is, for example, difficult for forest service data to estimate human-bias in fire-shape reports, which can arise from visual misidentification of fire patch boundaries and from sampling limitation due to the necessity of presence of an operator for each fire event. The coverage of such reports is moreover limited to specific regions of Earth. On the other hand, satellite data reliability is known to depend on land type, cloud cover (Giglio et al. 2009), algorithms used to reconstruct fire patches from pixels of BA and no data availability. However, satellite data allow for a continuous and global coverage of burned area. Since the Fire\_cci fire patch database aims to provide a global and unbiased description of fire patch morphology, satellite data are more suitable for such a task. But still, fire patch determination from Forest Services remains extremely useful to control the reliability of the satellite derived fire patch database. It is, however, very difficult to combine the two types of datasets for analyses purposes, since their sampling biases differ greatly.

The Fire\_cci fire patch database has been created by the Fire\_cci team from the MERIS Fire\_cci v4.1 (FireCCI41), MODIS Fire\_cci v5.0 (FireCCI50), MODIS Fire\_cci v5.1 (FireCCI51), the MCD45A1 collection 5.1 and MCD64A1 collection 6 BA data sets.

 <b>fire</b> cci	<b>Fire_cci</b> Climate Assessment Report		Ref.:	Fire_cci_D5.1_CAR_v1.4	
			Issue	1.4	Date
					Page

The FireCCI41 product uses the MERIS sensor to provide a global coverage of burned area every three days (at equator) from 2005 to 2011, with approx. 300x300m spatial resolution at Nadir (Oliva et al. 2011, Chuvieco et al. 2016). Using a similar algorithm than for FireCCI41 and based on the MODIS instrument on the Terra satellite, the FireCCI50 and FireCCI51 products provide BA over a longer time series (2001-2016, 2017 in the case of FireCCI51), and with a resolution of approx. 250x250m at equator. The MCD45A1 collection 5 and MCD64A1 collection 6 BA products provide a global coverage every day (at equator) for the time series (2000-2017), but with a lower spatial resolution (approx. 500x500m) (Roy et al. 2008, Giglio et al. 2016). As described in Section 4, these two data sets will be used for intercomparison of the Fire\_cci derived fire patch databases. A regional fire patch database has also been derived from the SFD BA product (based on Sentinel-2 data), which has also been generated by the Fire\_cci team. With its very high spatial resolution (approximately 20x20m at Nadir), it provides a very accurate determination of fire morphological features in Northern Hemisphere Africa. We have also compared the features of the fire patches of the SFD product with those of the MCD64A1 product, over their overlapping time series.

## 2. Methodology

Fire patches were obtained by grouping pixels of burned area into fire patches. This was done using the “flood-fill” algorithm (Loepfe et al. 2014), which behaves as follows:

- Starting from the top-left corner, the algorithm selects the first pixel with an identified burned date and attributes it an ID number.
- The algorithm reads all neighbouring pixels (following a chess “queen scheme”): all pixels whose burned dates are smaller than an arbitrary threshold (the cut-off) receive the same ID number as the central pixel.
- This process is repeated for each new pixel added to the group, until no more new pixels can be added following this method.
- The algorithm looks for the next pixel with an identified burned date, and which does not already belong to another identified pixel group.

Figure 1 shows that the choice of the cut-off can influence the size of the reconstructed patches. This effect is discussed and quantified in Section 4 for 3 different cut-off values identified as keystone thresholds for fire patch identification in Oom et al. (2016). These different values were chosen because they span the majority of cut-off values used in other analyses.

From the yearly patch ID maps, where each burned pixel is referenced by its patch ID, individual patch description metrics were calculated. For each patch, its surface area (A, in ha), the length of its perimeter (P, in number of pixel side) and its core area (CA in ha) were calculated, the last parameter defined for each fire patch as the area covered by the pixels totally surrounded by other pixels belonging to the same fire patch. Patch shape complexity was evaluated from its fractal dimension (FD) calculated as  $2 \times \ln(0.25 \cdot P) / \ln(A)$  and its shape index (SI) calculated as  $0.25 \cdot P / A^{0.5}$ . The full process is summarized on Figure 2.



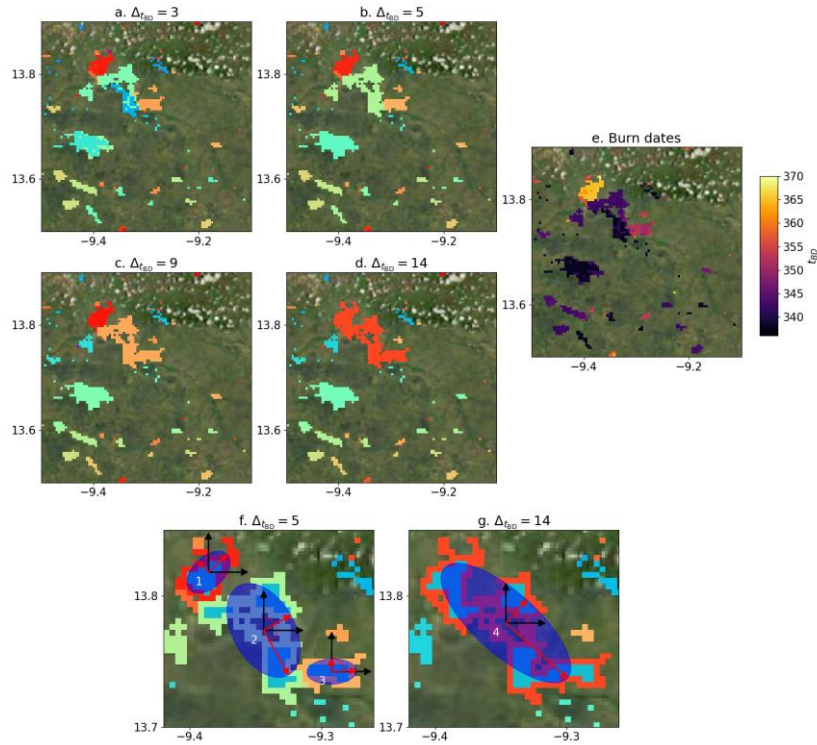


**Figure 1:** Example of fire patch reconstruction. Figures a to d show the fire patches calculated from individual burned pixels, with a cut-off of 3, 5, 9 and 14, for MCD64A1 in a region of northern hemisphere Africa. Continuous areas with the same colour indicate the same fire patch. Figure e shows the burn dates of the pixels (in days). Figures f and g show examples of the Standard Deviation Ellipses (SDE, dark blue) for three patches with a cut-off of 5 and 14. The half-axes and azimuthal angle are displayed in red.

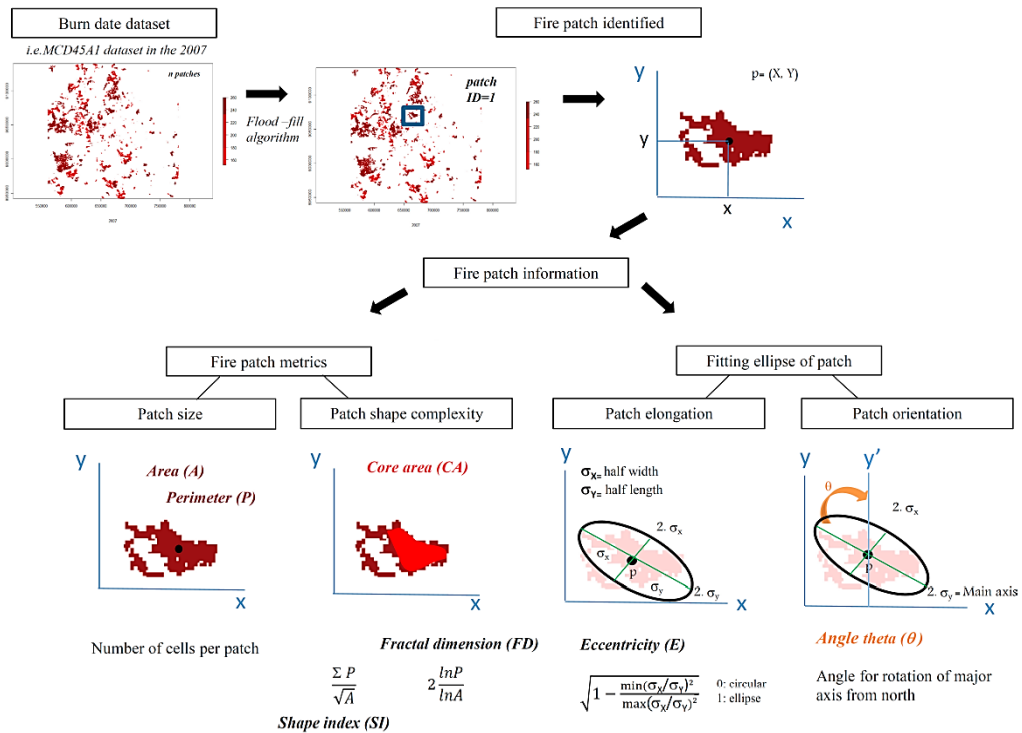


**Figure 2:** Flowchart of the fire patches processing (from Nogueira et al. 2016).

These commonly used patch metrics in landscape ecology were first developed in the Fragstats software and were used with the corresponding R CRAN package “SDMtools” (Species Distribution Modelling Tools). The ellipse fitting the spatial distribution of burned pixels within a patch was also computed, to capture the directional azimuthal angle and the elongation of the patch, two key variables describing fire spread processes. In addition, ellipses are the theoretical shapes simulated in DGVMs, and with which they can be benchmarked. Pixels belonging to the same patch ID were converted into points with geographic coordinates corresponding to the centre of the pixels. Then the “aspace” R CRAN package (Levine 2010) was used to fit the ellipse. From this ellipse, the main features were extracted, including:

- The projection of the longest axis along X and Y coordinates respectively named  $\sigma_x$  and  $\sigma_y$  and the azimuthal angle  $\theta$ , corresponding to the clockwise deviation of the longest axis of the ellipse from the northern direction, computed from lat/lon coordinates (in degree).
- The projection of the longest axis along X and Y coordinates respectively named  $\sigma_{x,km}$  and  $\sigma_{y,km}$  computed from local flat coordinate system (in km) and the azimuthal angle  $\theta_{km}$ , corresponding to the clockwise deviation of the longest axis of the ellipse from the northern direction (in degree).
- The eccentricity (E) as an index of patch elongation calculated as the square root of 1 minus the ratio of the squared lengths of the shortest and longest axis of the ellipse so that  $E = 0$  corresponds to the most elongated shape, and  $E = 1$  corresponds to a perfect circle.

Figure 3 shows the difference between the area of the fire patch computed from the ellipse  $A_{ellipse}$  and the area computed from the BA pixels  $A_{pixel}$ , scaled by  $A_{ellipse}$ , versus  $A_{ellipse}$ . The distribution is centred on a negative value (around 25 % for the Fire\_cci product, and 40% for MCD45A1 collection 5 and MCD64A1 collection 6), with a longer distribution tail toward positive values. This means that the ellipse tends to underestimate fire patch size compared to the one computed at the pixel level. This bias is independent of the fire size, and seems only related to the resolution of the spectrometer. Figure 4 shows the evolution of this area bias with perimeter to area ratio. For low values of perimeter to area ratio,  $A_{pixel}$  is generally bigger than  $A_{ellipse}$ , but as the perimeter to area gets higher, the difference reduces. For bigger patches, the tendency changes and  $A_{ellipse}$  starts to be bigger than  $A_{pixel}$ . This behaviour is expected, since larger and longer fires have a higher probability to encounter natural obstacles, and are therefore susceptible to have more complex fire shapes.

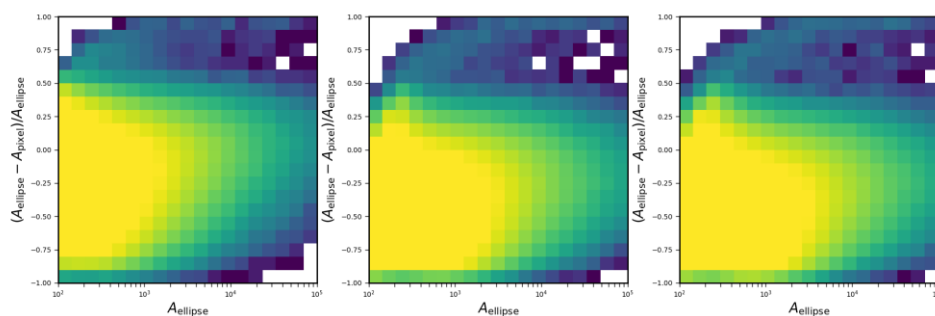


**Figure 3:** Difference between the areas computed from the ellipse and from pixel, normalized by the area of the ellipse, with respect to ellipse area. The left plot displays the result for the MERIS Fire\_cci product, the centre one for MCD45A1 collection 5 and the right one for MCD64A1 collection 6.

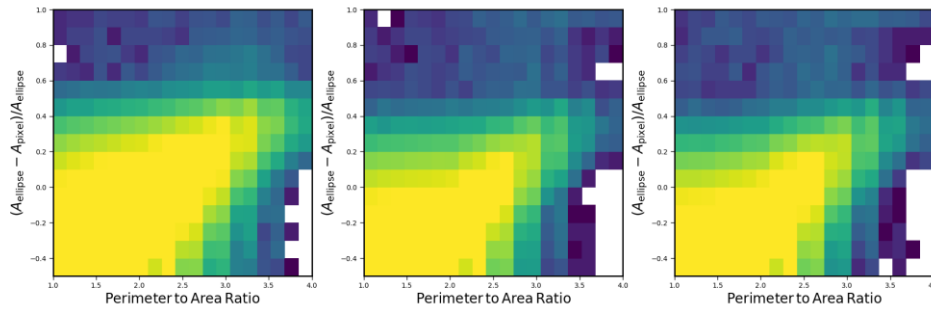


**Figure 4:** Same as Figure 3, but with perimeter to area ratio. The discontinuities arise from the fact that perimeter to area ratio for small patches will take discrete values.

Because both BA products are very large data sets, both of them were separated in  $3.75 \times 3.75^\circ$  tiles in order to parallelize the process. This method exposes us to a bias in the database since fire patches located close to the tile borders can be cut. This is why bands of  $0.625^\circ$  from each border of the tiles overlap with neighbouring tiles. All fire patches whose centres are within the central  $2.5 \times 2.5^\circ$  area were attributed to the tile to avoid double counting. An example is displayed on Figure 5.

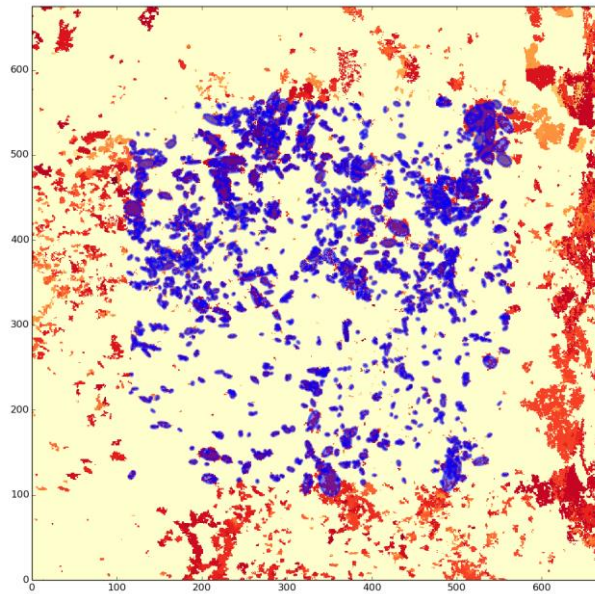


**Figure 5:** Example of a  $3.75 \times 3.75^\circ$  tile in Africa, which illustrates the removal of the  $0.625^\circ$  bands on the borders of the tile. The patches located on the borders are added to the database when the neighbouring tiles are processed, to avoid double-counting.

### 3. Assessing the conservation of fire patch morphological features across fire products

Fire spread processes are driven by the spatial arrangement of fuel, its water content status, and the combined effect of wind and topography. The Rothermel's equation (Albini 1976, Rothermel 1972):

$$R_{surface} = \frac{I_R(1 + \phi_w + \phi_s)}{\rho_b \epsilon Q_{ig}}$$

synthesizes these combined effects used in spatially-explicit fire spread modelling (Burgan and Rothermel 1984), and is usually applied in landscape fire succession

models (Cary et al. 2006) for simulating fire contours.  $R$  is the rate of fire spread,  $I_R$  is fire intensity,  $\Phi_w$   $\Phi_s$  are modifiers for wind ( $w$ ) and slope ( $S$ ),  $\rho$  is fuel bulk density,  $\epsilon$  is effective heating number, and  $Q$  is heat of pre-ignition. In turn, the final shape of fires, and fire intensity within the fire event, are driven by wind conditions (wind speed and direction) and topography. At the global scale, fire modules use a similar empirical formulation to simulate a theoretical ellipse of fire shape, but only driven by wind speed (Figure 6), with no information on landscape composition and structure or topography being available at this level. We then hypothesize here, for future climate modelling development including fire emissions, that pixel level information from global burned area remote sensing products can provide the keystone morphological features of fire shapes. However, global remote sensing products have usually been assessed according to the total burned area (Mouillot et al. 2014), its seasonal pattern (Giglio et al. 2013) and more recently the patch size distribution (Hantson et al. 2015). Instead of comparing the two datasets pixel to pixel, and deriving the usual overall accuracy and commission and omission errors, it is proposed here to investigate the conservation of fire patch morphological features in pixel level global remote sensing products compared to fine resolution observations. Fire patches, as an assemblage of adjacent pixels of quasi-similar burn-date, can be described by their complexity, their elongation in space and the orientation of the major direction of the patch, as a key indicator of their underlying spreading conditions. Similar commission and omission errors, important to quantify pixel to pixel accuracy, can however have contrasted consequences on the final fire shape as illustrated in Figure 7. Accuracy of fire patch morphology has never been evaluated yet in global remote sensing, despite the potential interest in extracting key spreading information.

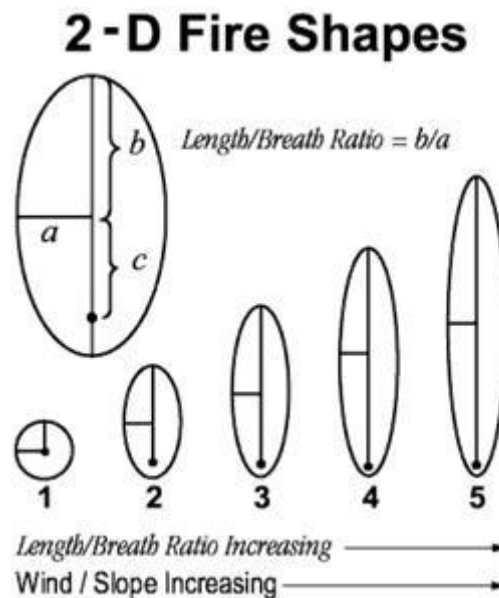


**Figure 6:** Illustration of a theoretical 2-D fire ellipse (from Alexander 1985).

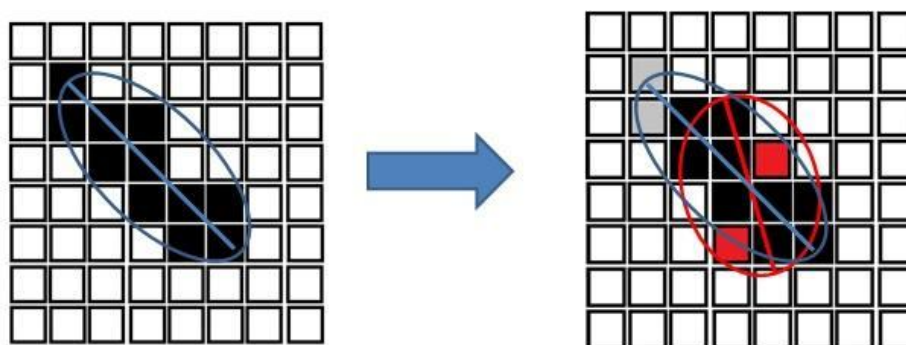


**Figure 7:** Illustration of the modification of patch morphological features because of commission (in red) and omission errors (in grey).

### 3.1. At the local scale in the Brazilian Savanna

The study was focused on a selected site in the South American savanna (Brazil) (Figure 8), one of the most fire-prone biomes globally, and one of the validation test sites for the MERIS Fire-cci v3.1 (FireCCI31) global BA product. This first part presents the methodological development based on the early FireCCI31 and the keystone information derived from the pixel level product, to be further implemented at the continental (Section 3.2) and global scale. LANDSAT-based fire patch dataset and both MODIS MCD45A1 collection 5, and FireCCI31 were used. The consistency of fire patch metrics among these three datasets as a quality assessment were tested. The study area (250,000 km<sup>2</sup>) is located in the north-western part of the Tocantins state (TO) in central Brazil extending from 7°47'0" – 9°33'0"S to 48°55'0" – 50°26'0" W at the boundary between the savanna biome (Cerrado) and the Amazonian forest, a fire-prone region as a consequence of a flammable and dry vegetation type, and with high likelihood of human ignitions. MCD45A1 collection 5 and FireCCI31 were characterized by a burned date layer indicating the day of the year when a fire occurred, and the corresponding quality flag indicating the level of confidence in the fire occurrence varying between 0 (low confidence) to 100 (high confidence). Some MERIS Archives were missing in this area (Ramo et al. 2014) potentially leading to additional missing fires in this study site. Only the burned dates with confidence level higher than 50% were selected for MCD45A1 collection 5 and FireCCI31. The confidence level in the two products is derived from different calculations, difficult to compare. The same threshold in the two datasets was selected, acknowledging the potential bias related to this choice. All the datasets were re-projected at 30m resolution in the UTM 22S datum WGS84 projection over the LANDSAT 7 scene 223/066 of the Worldwide Referencing System 2 (WRS2) Path/Row. The burn date (BD) dataset from MCD45A1 collection 5 and MERIS Fire\_cci v3.1 was used to identify individual burned patches (ID), using the spatio-temporal flood fill algorithm. The main characteristics of the surveys compared in this section are displayed on Table 1.





**Figure 8:** Administrative map of Brazil

**Table 1:** Descriptions of global burned area data used for fire patch studies

Burned area dataset	Satellite	Temporal and spatial resolution	Temporal series used
LANDSAT	Landsat 5, Thematic Mapper (TM), Landsat 7, enhance thematic mapper (ETM+)	15 days, 30m	2002-2009
MCD45A1 collection 5	TERRA MODIS	Daily, 500m	2002-2009
FireCCI31	ENVISAT-MERIS	2-3 days, 300m	2006-2008

The overall agreement between the three BA products inter-comparisons was 0.97, with an omission error varying between 0.49 for the comparison between the two global products MCD45A1 collection 5 and FireCCI31, to 0.81 for the FireCCI31 and LANDSAT comparison. The commission error varied between 0.64 for the MCD45A1 collection 5 and LANDSAT comparison to 0.74 for FireCCI31 and LANDSAT. When examining the omission and commission errors for each fire size class, higher errors ( $>0.9$ ) for the smallest fire size class were obtained. The fire patch database were divided according to patch size classes with thresholds of 90ha, 270ha, 450ha, 630ha and 900 ha, similar for all datasets whatever their resolution. We observe in the 90ha-270ha size class (called 90ha class), that FireCCI31 captured more patches overlapping with LANDSAT than MCD45A1 collection 5, due to its highest spatial resolution detecting more small fires, and in turn a better accuracy in properly locating these small fires, although remaining below 30%. No bias in the number of patches was observed in the other classes (Nogueira et al. 2016). Then, patch to patch correlations for each patch metric were investigated. For each cross tabulation and patch size threshold, the coefficients of determination  $R^2$  indicating the fraction of the variance explained by the best-fitted linear regression, and the slope indicating the potential bias to the 1:1 line expected if the sensors are fully conservative of the patch metrics are illustrated in Figure 9. For the patch area, the highest  $R^2$  were obtained for the FireCCI31 and MCD45A1 collection 5 ( $R^2 > 0.8$  for all patch sizes) and slopes close to 1, indicating very similar patch sizes between the two global BA products. When comparing global BA products to LANDSAT,  $R^2$  were also high for FireCCI31 ( $R^2 > 0.8$ ) and lower for the MCD45A1 collection 5 product ( $R^2$  varies between 0.4 and 0.8). Slopes of the regression for both global BA products FireCCI31 and MCD45A1 collection 5 cross-tabulated with LANDSAT varied between 0.8 for all fire size classes and 0.6 for larger



fire  
cci

Fire\_cci  
Climate Assessment Report

Ref.: Fire\_cci\_D5.1\_CAR\_v1.4

Issue 1.4 Date 16/11/2018

Page 18

fire sizes, indicating an underestimation of patch areas of similar magnitude for both global BA products. The correlation coefficients for the core area were similar to the total patch area, but with regression slopes reaching (0.6–0.9), indicating a slightly lower error in patch areas when removing the patch boundary buffer zone (500 m), where uncertainty seems to be the highest. Patch perimeters were also well correlated ( $R^2$  varying between 0.4 and 0.85) but with much higher perimeter values for LANDSAT patches performed at 30m resolution compared to MCD45A1 collection 5 and FireCCI31 performed at 500m and 300m, so that regression slopes vary between 0.3 and 0.65. Shape index and Fractal dimensions were correlated with  $R^2$  around 0.5 between the two global products FireCCI31 and MCD45A1 collection 5 but poorly correlated when compared to LANDSAT with  $R^2 < 0.3$ , an expected result regarding the higher resolution of the LANDSAT fire patches. The largest patches ( $> 900$  ha), however, experience better, yet still low, correlations for the fractal dimension ( $R^2 > 0.4$ ). When analysing the comparison of the fitted ellipse features (eccentricity and azimuthal direction of the longest axis),  $R^2$  were low for all comparisons, but reached values  $R^2 > 0.3$  for patches larger than 450 ha for eccentricity and  $R^2 > 0.4$  for patches larger than 450 ha for  $\theta$ . Under this patch size threshold,  $R^2$  was below 0.5. Slopes of the regressions between eccentricities vary between 0.3 and 0.7 for patches larger than 450 ha, lower than the expected 1:1 line, indicating an underestimation of patch elongation and missing pixels at the extremes of patches. Slopes of the regressions for  $\theta$  varied between 0.7 and 1.1 for all product comparisons, close to the expected unbiased 1:1 line.

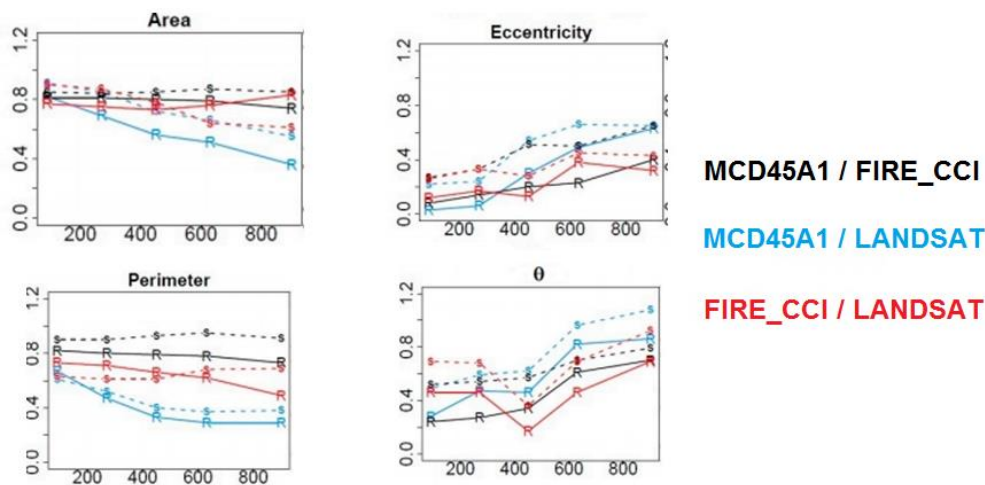


**Figure 9:** Coefficients of determination (R) and regression slope (s) (Y axis) as a function of patch size (in ha, X axis) for patch size, eccentricity, perimeter and patch orientation ( $\theta$ ), for the different BA products. (R) solid line: coefficient of determination; (s) dotted line: slope.

### 3.2. At the continental scale in North America

The fire patch analysis initially developed at the local scale on FireCCI31 in Brazil was extended with the FireCCI41 and MCD64A1 collection 6 products at the continental level in North America (United States and Canada), where additional local level information on fire shapes is available. For Canada, fire polygons from the Canadian National Fire Database (CNFD) were used, which can be downloaded from the Canadian Wildland Fire Information System (CWFIS). For United States (US), fire polygons from Geospatial Multi-Agency Coordination (GeoMAC) were used. GeoMAC



	<b>Fire_cci</b> <b>Climate Assessment Report</b>		Ref.:	Fire_cci_D5.1_CAR_v1.4	
			Issue	1.4	Date
					Page

fire polygons are collected in the field using tools such as GPS or infrared flights. Similarly, CNFD fire polygons are collected from several sources.

The whole North American continent was first divided into  $2^\circ \times 2^\circ$  resolution tiles. Each tile was reprojected into equal area projection. The BD dataset from FireCCI41 and MCD64A1 collection 5 were used to identify individual burned patches (ID) for the 2005-2011 period for which FireCCI41 is available, using the similar spatio-temporal flood fill algorithm as developed at the local level. Regarding the sensitivity of the patch identification to the cut-off value (maximum burned date difference between two neighbouring cells to be considered for belonging to the same fire patch) as illustrated in Oom et al. (2016), FireCCI41 and MCD64A1 collection 6 with cut-off values of 3, 5, 9 and 14 days were processed. Besides, fire polygons from forest services for the same period were projected and rasterized, for each tile, on the projection of the FireCCI41 and MCD64A1 collection 6 datasets so that each burned pixel belongs to a patch identification number ID. For all fire datasets (FireCCI41, MCD45A1 collection 6, and GeoMAC\_CNFD forest service), for each tile fire morphological features were computed for each fire patch larger than 100 ha, according to the threshold determined to compute reliable fire morphological features ( $> 5$  pixels). In turn, for each tile, a list of fire patch IDs were obtained. For each dataset, each fire patch was characterized by the following fire morphological features by considering more specifically direction, size, spread and complexity: area, the directional angle of the longest ellipse axis, and eccentricity.

To build and assess the quality of the fire patch assemblage and compare datasets from the various sources in each  $2^\circ$  tile, we hypothesized that the community of fire patches defined by their morphological features should be as similar as possible. To compare the lists of fire patches derived from the fire datasets over the North American continent, we relied on a novel approach initially developed in community ecology. When a list of fire patches (called 'assemblage') is considered, characterized by a set of  $n$  morphological features (called 'traits'), each fire patch (called 'species') can be located in an  $n$ -dimensional space, each axis representing the values of a trait. In turn, each assemblage (or list) of fire patches representing a pyro-region (or community), is defined by the  $n$ -dimensional (volume or space) distribution of points, defined by their trait values. Comparing two assemblages then relies on comparing the  $n$ -dimensional distribution (morphological space) of fire patches defined by their morphological traits. We hypothesize here that the fire regime in a given region, obtained from two datasets, should have similar  $n$ -dimensional (morphological space) distribution of fire patches.

Statistical frameworks describing  $n$ -dimensional volume of traits have already been developed in the field of community ecology to assess the distribution of species (vegetal or animal) defined by their functional traits for each assemblage across space or time (Schleuter et al. 2010, Mason et al. 2005). As illustrated on Figure 10, among different indices, the Functional Richness (FRic) describes the whole volume defined by its extreme traits (Figure 10b). The Functional Evenness (FEve) indices measure whether mean species traits are distributed regularly within the occupied trait space, i.e. with equal distances between nearest neighbours and equal abundances (Figure 10c). Functional Divergence (FDiv) indices measure the variance of the species functions and the position of their clusters in trait space (a high FDiv is caused by the clustering of species and/or abundances at the edges of the traits space) (Figure 10d). Functional Dispersion (FDis) indices measure the weighted mean distance to the average position of the species present in an assemblage. Functional Specialization (FSpe) indices

measure the weighted mean distance of a species to species pool centroid. Functional Originality (FOri) indices measures the weighted mean distance of a species to the nearest from the species pool. Comparing functional structure of fire patch datasets then relied comparing the values of FRic, FEve, FDiv, FDis, FSpe and FOri indices ranging from 0 to 1.

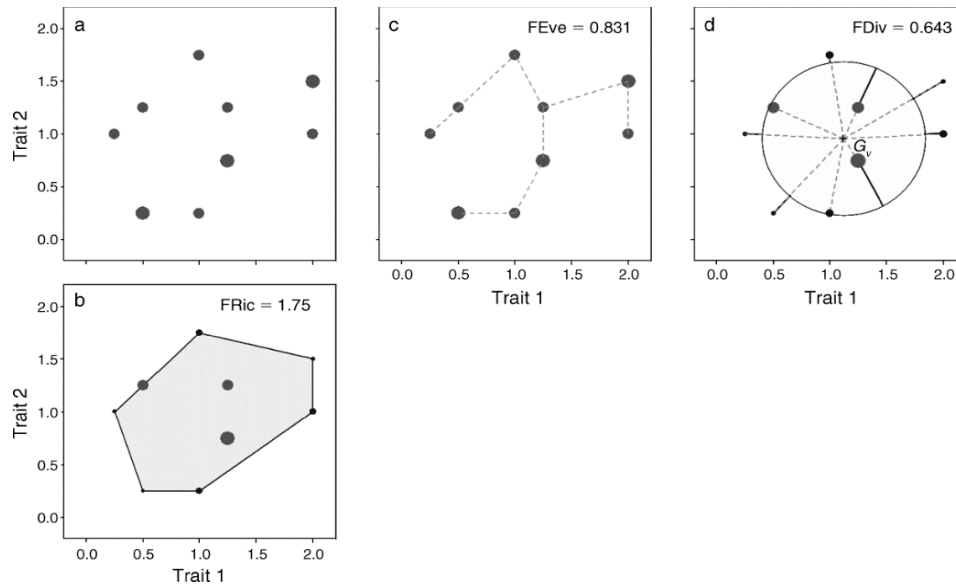


**Figure 10:** Adapted example of three different functional diversity indices in functional space from Villéger et al. (2008): Functional Evenness (FEve), Functional Divergence (FDiv), Functional Richness (FRic).

Another approach developed in community ecology used the concept of  $\beta$ -diversity ( $\beta$ -div) (Figure 11, Villéger et al. 2013) to investigate how two co-occurring n-dimensional volumes overlap ( $\beta$ -div), which can be decomposed in how two co-occurring n-dimensional volumes are translated (Turnover, Turn) in the functional space, or are included (Nestedness, Nest) in each other. The two volumes can completely overlap ( $\beta$ -div = 0, Turn = 0, and Nest = 0, Figure 11b) or completely mismatch ( $\beta$ -div = 1, Turn = 1, and Nest = 0, Figure 11d, g). In between, the two volumes can partially overlap, either one volume being completely ( $\beta$ -div = Nest, and Turn = 0, Figure 11e) or partially ( $\beta$ -div, Turn and Nest > 0, Figure 11f) included in the other or both volumes being the same size (similar richness) but translated in the n dimensional space ( $\beta$ -div = Turn, and Nest = 0, Figure 11c). Comparing the dissimilarity of morphological structure of fire patch datasets then relied in comparing the overlap (functional  $\beta$ -div), translation (functional Turn) and inclusion (functional Nest) in the functional space.

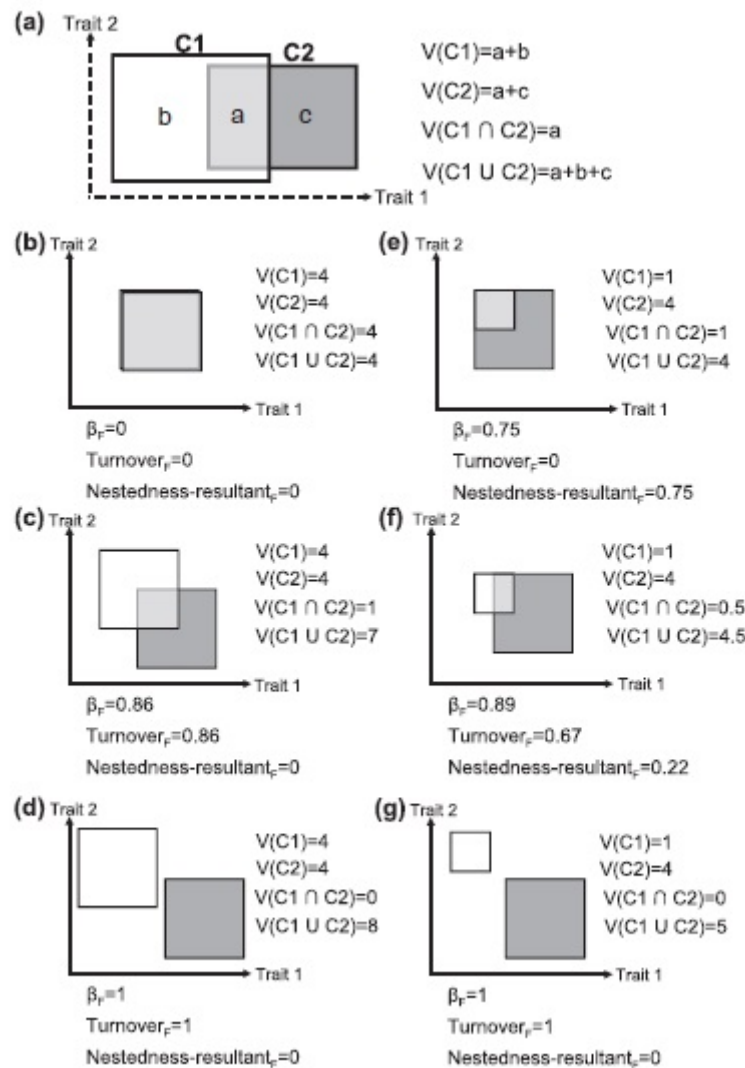


**Figure 11:** Conceptual framework for the decomposition of functional  $\beta$ -diversity from Villéger et al. (2013) with theoretical examples of complete trait overlap (b), partial trait inclusion (e), partial overlap (c, f) and total mismatch (d,g).

The structure of the fire patches was evaluated by computing the functional diversity indices for each sensor at each of the cut-off thresholds. The analysis was focused on the comparison between each sensors and the forest service dataset. Figure 12 illustrates the continental map of FRic and FDis for FireCCI41 and the forest service data GeoMAC\_CNFD. When comparing cell to cell values of functional diversity indices obtained for the North American continent for FireCCI41 and for GeoMAC\_CNFD forest service (Figure 12), FireCCI41 present higher values than GeoMAC\_CNFD forest service suggesting that the volume of FireCCI41 is larger and defined by more extreme functional traits than the volume of the forest service, for example more extended fire patches, more elongated or more complex. When plotting the pixel to pixel comparison of the two dataset, no clear relationship on the continental pattern between the two dataset was identified. Higher FRic in FireCCI41 are actually located in the central USA, at the boundary between mountainous forests and grasslands, so that grassland fires might be accounted for in FireCCI41 data and not in the forest service's dataset. Nevertheless, it could be concluded that FireCCI41 might generate fire patches with extreme morphological features not observed with local observations, as for



example two neighbouring fires happening at the same time in forest services but considered as one joined fire from the flood fill algorithm.

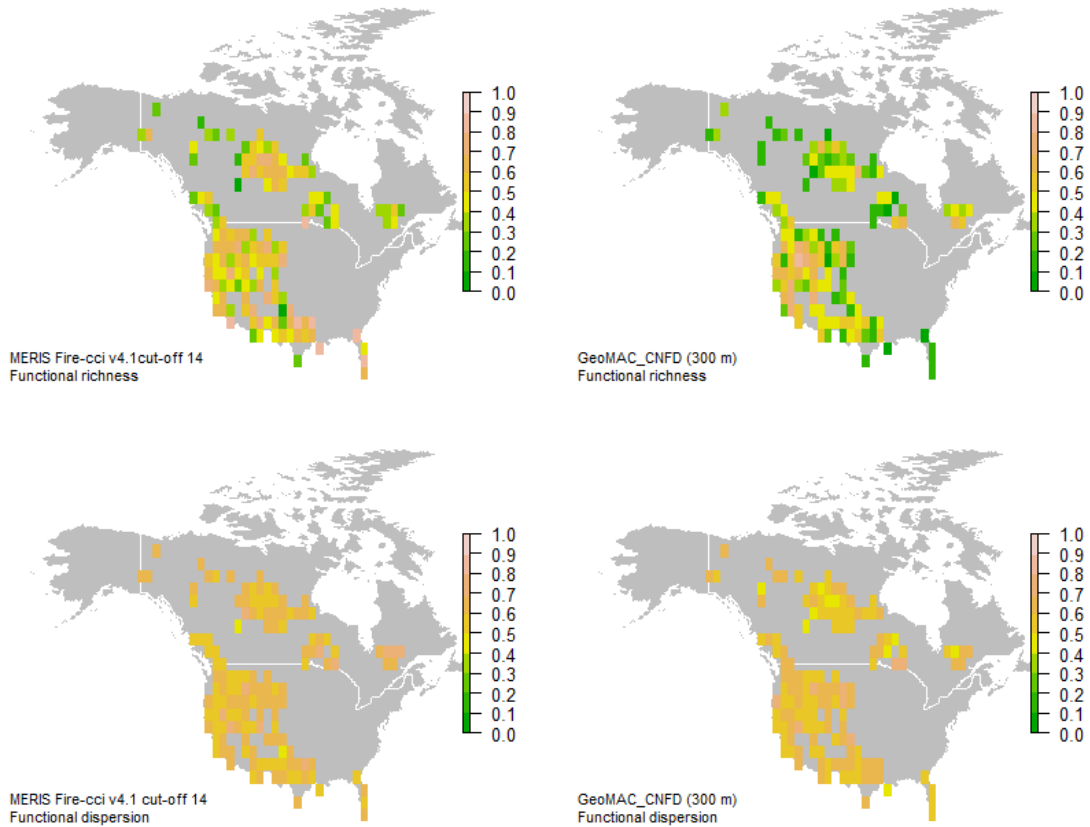


**Figure 12:** Example of Functional Richness (FRic) and Functional Dispersion (FDis) obtained from FireCCI41 cut-off 14 (Left) and GeoMAC\_CNFD forest service (Right).

When looking at FDis, representing how dispersed are fire types within the n-dimensional space, more similarities between datasets were obtained, with a linear correlation when comparing tile to tile indices (Figure 13), suggesting that both datasets present similar assemblage of fire patches beside the extremes driving FRic. These results then tend to acknowledge the accuracy of the assemblage of patch morphological features between FireCCI41 and local observations for most fire patches, but the flood-fill algorithm might generate potential extreme fire size or complexity actually not happening, or not referenced the same way (in the case of multiple joined fires) in forest service data. Our statistical framework captures in few indices a complex comparison, usually performed with the Gini index (Oom et al. 2016), but with special emphasis on morphological features explaining fire spread processes generating fire patches, a keystone information for global fire model benchmarking.

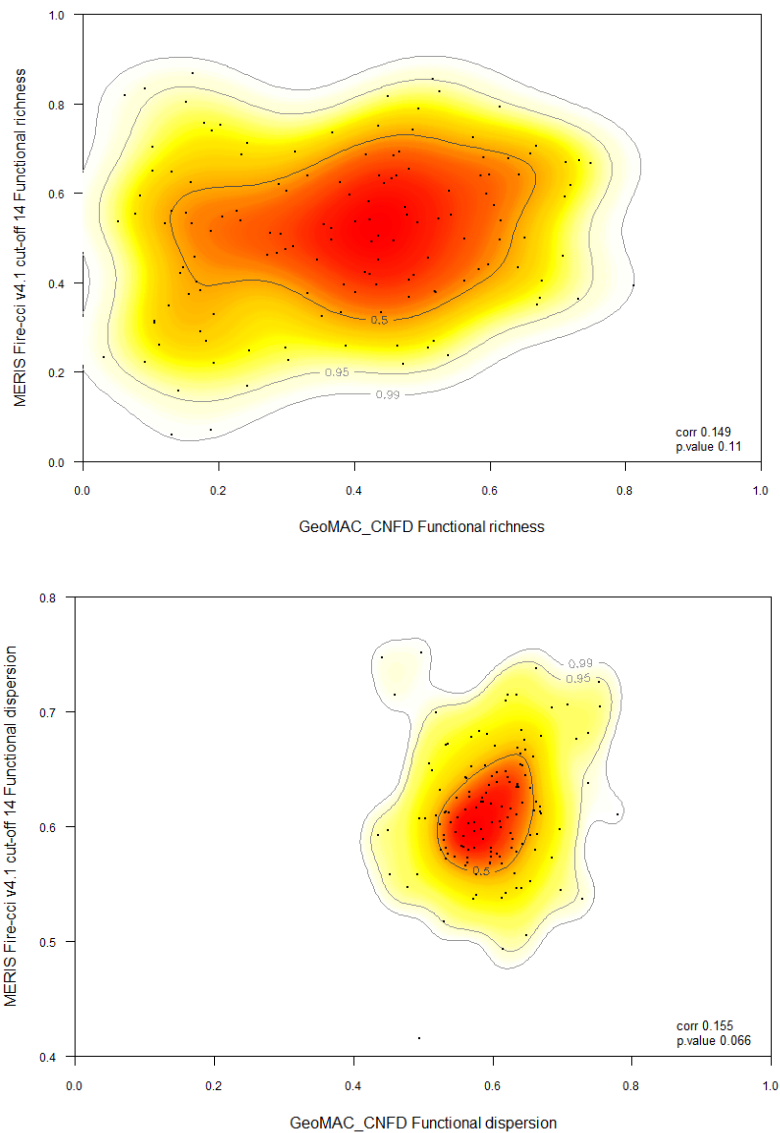


**Figure 13:** Bivariate relationships between Functional Richness (FRic, top) and Functional Dispersion (FDis, bottom) obtained from GeoMAC\_CNFD forest service (x-axis) and FireCCI41 cut-off 14 (y-axis).

Similarly, when comparing tile-to-tile values of FRic obtained from GeoMAC\_CNFD forest services and MCD64A1 collection 6 (Figure 14), MCD64A1 collection 6 presents higher values than GeoMAC\_CNFD forest service with a low spatial correlation (Figure 15). When looking at FDis, similar results as in the FireCCI41 comparison were obtained, with a significant correlation of the spatial pattern of these indices at the continental level, suggesting a good agreement between the two datasets when omitting extreme patches.

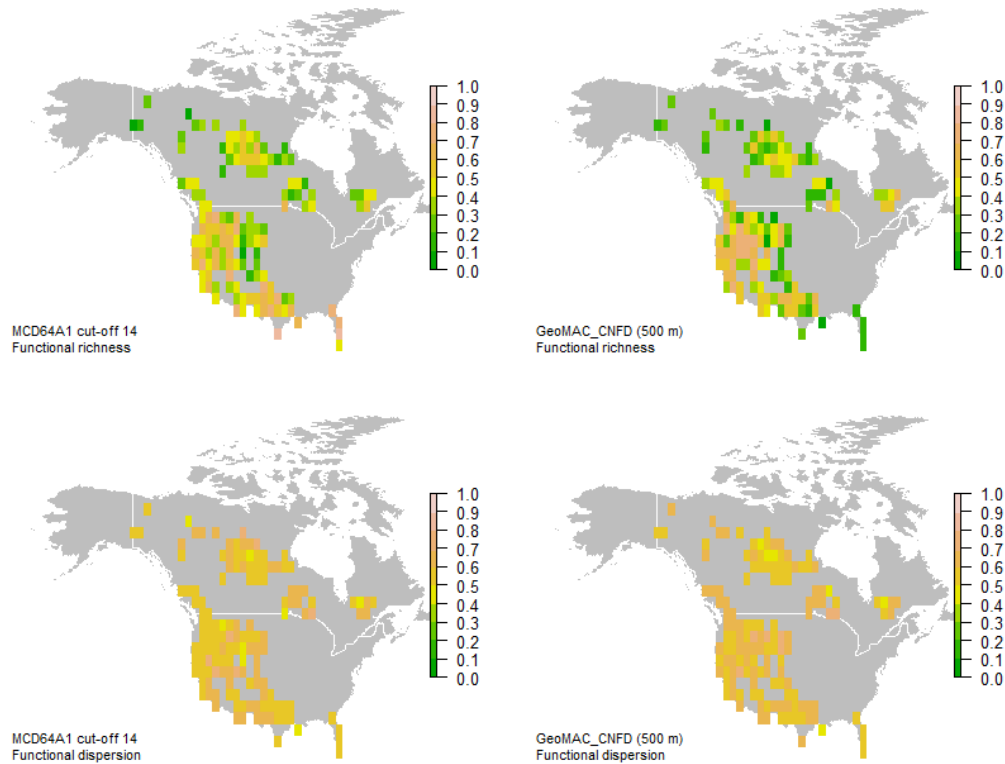


**Figure 14:** Example of Functional Richness (FRic) and Functional Dispersion (FDIs) obtained from MCD64A1 collection 6 cut-off 14 (Left) and GeoMAC\_CNFD forest service (Right).

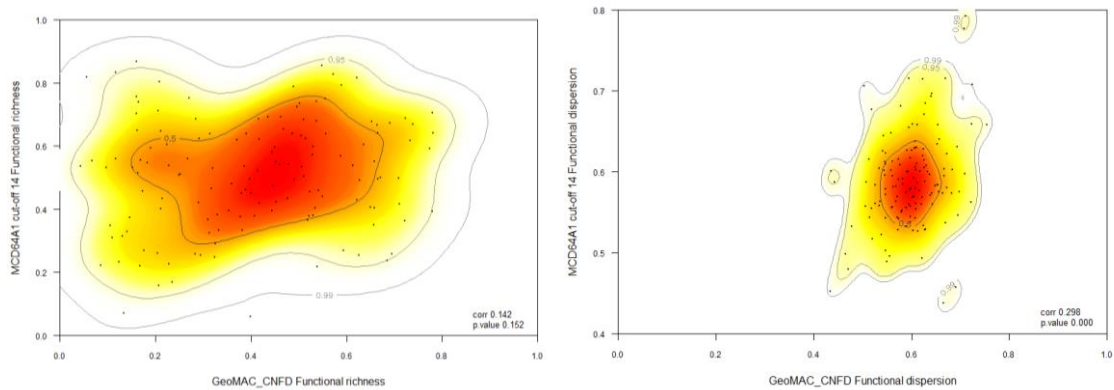


**Figure 15:** Bivariate relationships between Functional Richness (FRic, top) and Functional Dispersion (FDIs, bottom) obtained from GeoMAC\_CNFD forest service (x-axis) and MCD64A1 collection 6 (y-axis).



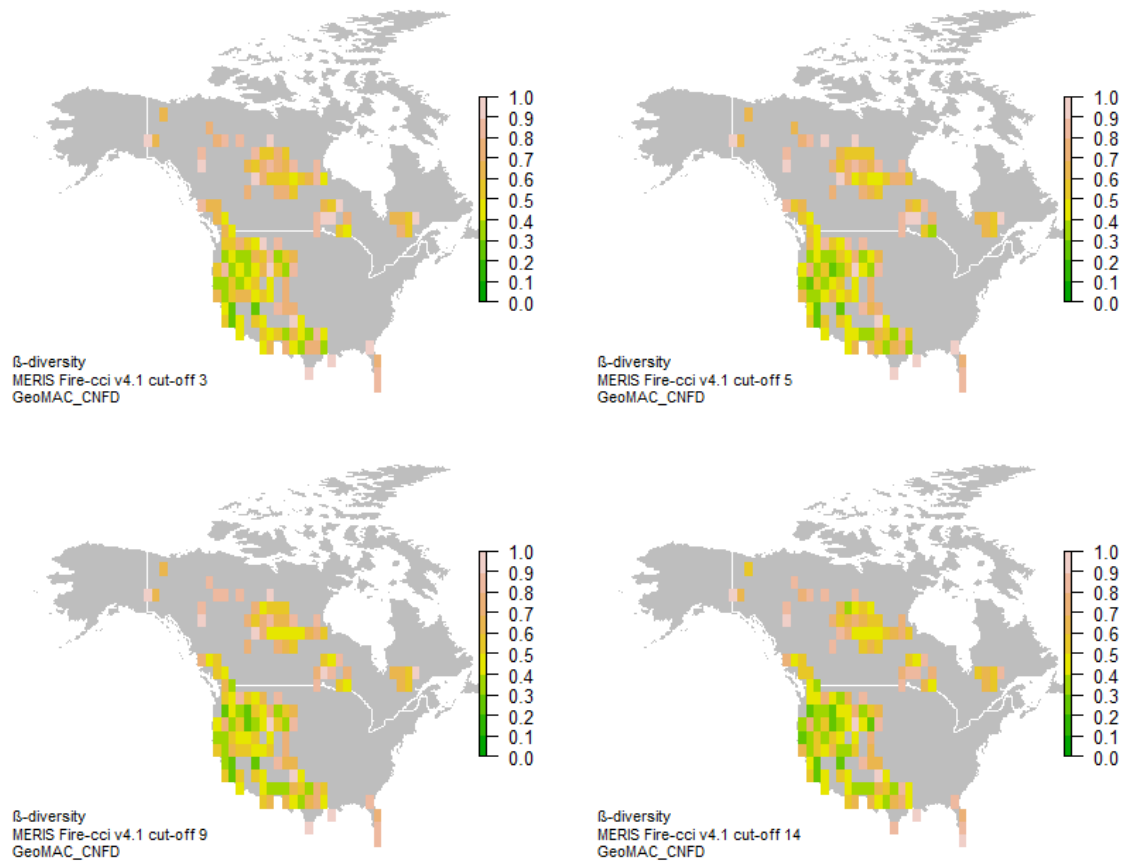


**Figure 16:** Functional  $\beta$ -diversity ( $\beta$ -div) maps for North America obtained from GeoMAC\_CNFD forest service and FireCCI41 cut-offs 3, 5, 9 and 14.

Then the dissimilarity between the assemblages of fires patches were evaluated by computing the volume overlap (i.e. functional  $\beta$ -div) of the pairwise comparison and decomposing it into the volume translation (i.e. functional Turn) and inclusion (i.e. functional Nest). Figure 16 illustrates  $\beta$ -div maps between GeoMAC\_CNFD and FireCCI41 cut-off 3, 5, 9 and 14.  $\beta$ -div higher than 0.2 were obtained, suggesting partial overlapping between functional spaces, whatever the cut-off values for the patch identification algorithm, and supporting previous results on the FRic difference. However, it can be observed that  $\beta$ -div slightly decreased with higher cut-offs, suggesting better agreement between remote sensing and forest service products with high cut-off values.

When looking at the functional  $\beta$ -div maps obtained from comparison of the remote sensing-derived products MCD64A1 collection 6 and FireCCI41, high values of  $\beta$ -div can still be observed, but decreasing to 0.2 (Figure 17), suggesting a larger overlap between remote sensing derived products than considering forest services. When comparing different cut-off values, it can be observed that  $\beta$ -div slightly decreased with lower cut-offs, suggesting better agreement between remote sensing products with low cut-off values. Burn date uncertainties and mismatch between remote sensing products might then generate stronger differences for high cut-off values, generating abnormally and inconsistently large fires between products. When comparing  $\beta$ -div spatial pattern between cut-off values (Figure 18), a strong linear correlation is observed, suggesting that the spatial pattern of mismatch between FireCCI41 and MCD64A1 collection 6 is not influenced by cut-off values.



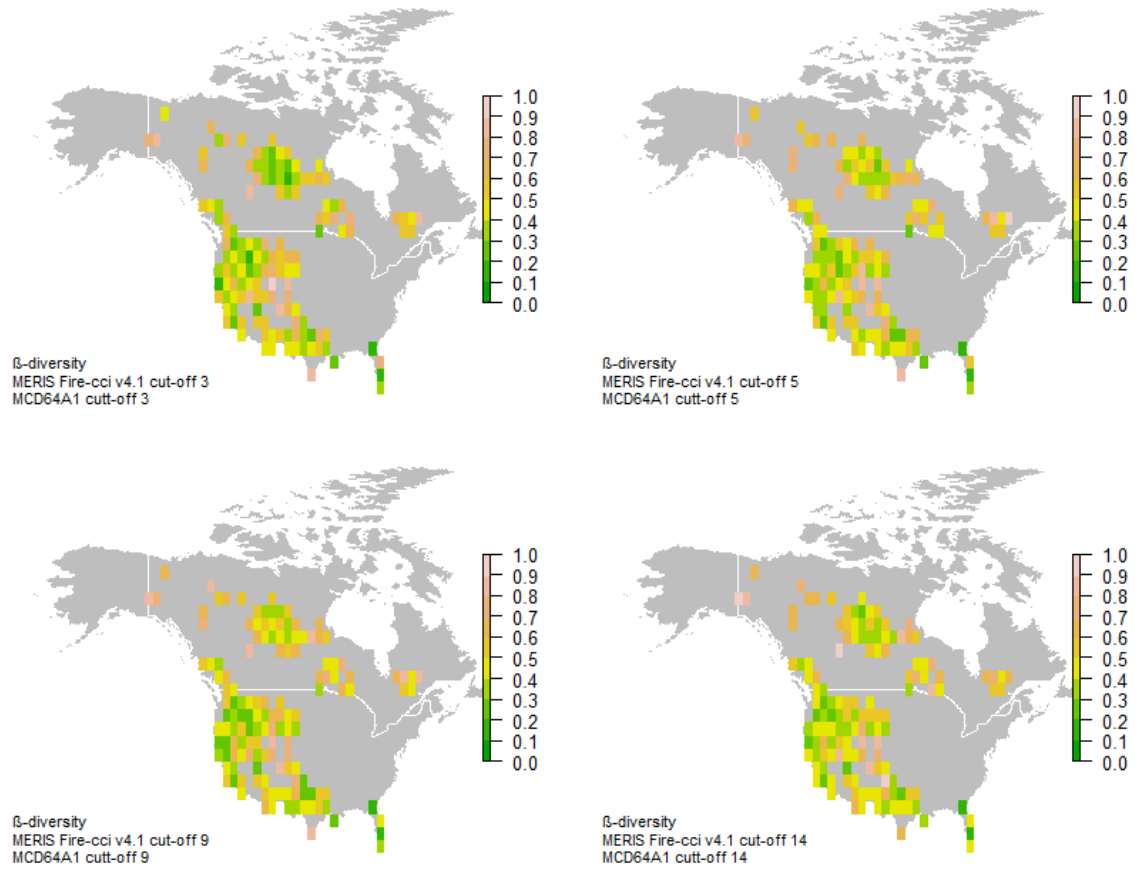


**Figure 17:** Functional  $\beta$ -diversity ( $\beta$ -div) maps for North America obtained from MERIS Fire\_cci v4.1 (FireCCI41) and MCD64A1 collection 6 cut-off 3, 5, 9 and 14.

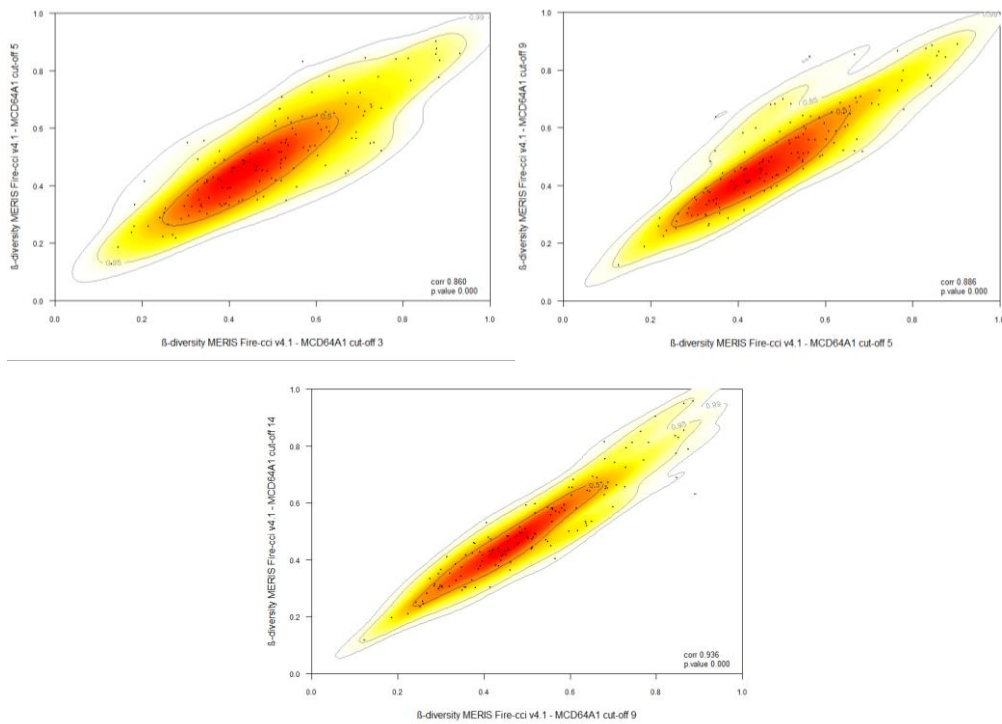


**Figure 18:** Bivariate relationships between functional  $\beta$ -diversity ( $\beta$ -div) obtained from MERIS Fire\_cci v4.1 (FireCCI41) and MCD64A1 collection 6 cut-off 3, 5, 9 and 14.

In order to better capture the three components of the n-dimensional hypervolumes, as overlap ( $\beta$ -div) is decomposed in volume translation (Turn) and volume inclusion (Nest), a colour composition of functional  $\beta$ -div, Turn and Nest was created. Figure 19 shows the colour interpretation of theoretical examples of partial trait inclusion, partial overlap, total mismatch and total match following Vileger et al. (2013). We present in Figure 19 the correspondence between types of hypervolumes overlap and the colour legend further used in the continental maps (Figure 20 and Figure 21). In short, the lighter the colour, the higher is the agreement. Blue corresponds with cases where Nest is higher than Turn, while purple corresponds with cases where Turn is higher than Nest.

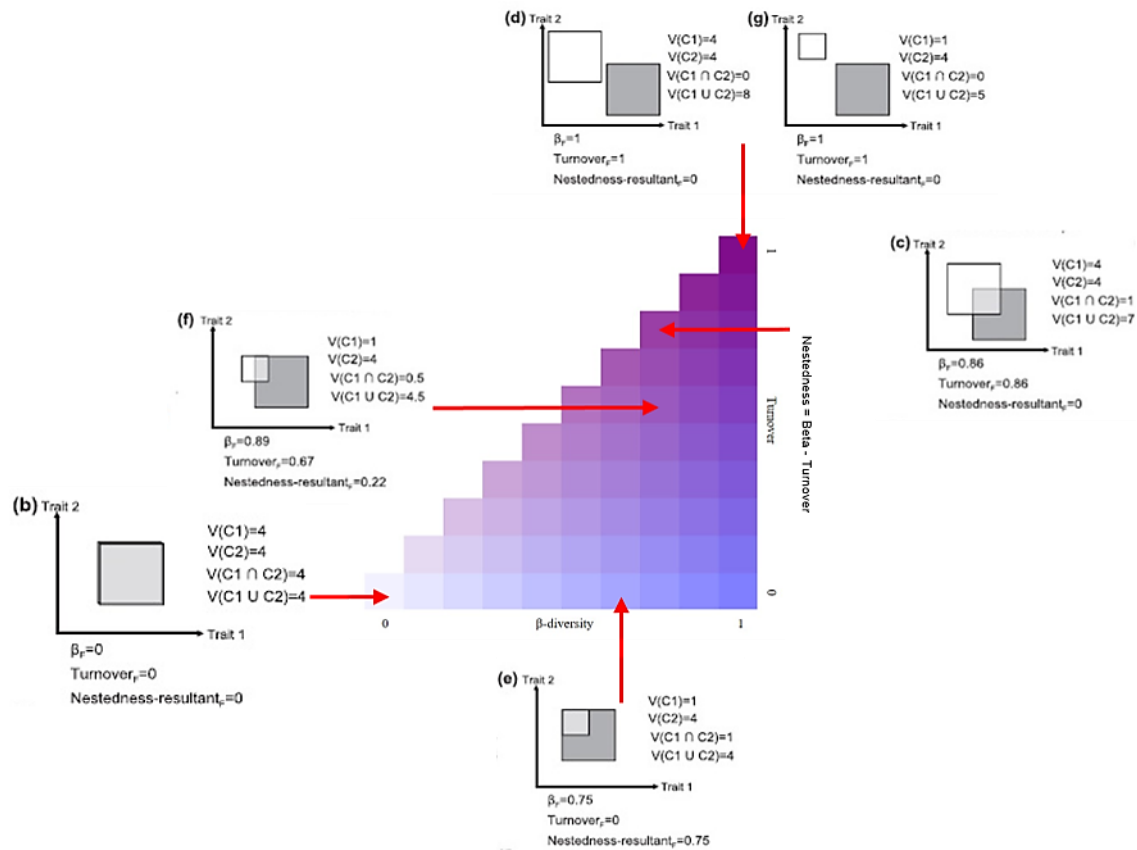


**Figure 19:** Interpretation of colour composition of functional  $\beta$ -diversity ( $\beta$ -div), functional Turnover (Turn) and functional Nestedness (Nest) with theoretical examples of partial trait inclusion (e), partial overlap (c, f), total mismatch (d, g) and total match (b) from Vileger et al. (2013). High values of Nest are under the black line, while low values of Nest over the black line.

Figure 20 illustrates the colour composition of  $\beta$ -div, Turn and Nest over North America between GeoMAC\_CNFD and FireCCI41 cut-off 14. For most of the continent “purplish” combinations were obtained, representing a partial overlap (cases f and c from Vileger et al. 2013, Figure 19), mostly identified in the rocky mountains of the USA. The second dominant composition is the ‘bluish’ case, representing of partial trait inclusion (case e from Vileger et al. 2013, Figure 19), mostly identified in the eastern part of the rocky mountains of the USA and Central Plains. Combinations “dark purplish” were mostly identified in boreal areas, representing a high  $\beta$ -div value and Turn and a low Nest, describing a low overlap between products (cases d and g from Vileger et al. 2013, Figure 19).



We note here that a mismatch on one single trait can lead to high  $\beta$ -div values. For example, as observed for Brazil, fire patches from global remote sensing are usually smaller in area than local observations, a result that was also captured in North America. Lower  $\beta$ -div values are observed in the US Rockies, indicating the best agreement between the two products in cells located in this region. When looking at the functional Turn and the functional Nest, higher Turn values were observed in the boreal forests of Canada, which, combined with high  $\beta$ -div values, indicate a similar functional richness (similar diversity of fire traits), but translated in the n-dimensional hypervolume, which in turn suggests that global remote sensing is somehow systematically biased from local observation with small fire sizes, small core area, or smaller perimeter, for example. On the contrary, in the US Eastern Rockies and Central Plains, Nest values are higher, indicating for these regions that FireCCI41 captures only a fraction of all the fire shape diversity observed from local forest services, suggesting potential missing fires in one of the datasets, potentially due to forest services not registering grassland fires. It is necessary to note that forest service fire databases were used, while the FireCCI41 includes all types of fires, so discrepancies are higher in this region of mixed vegetation types.

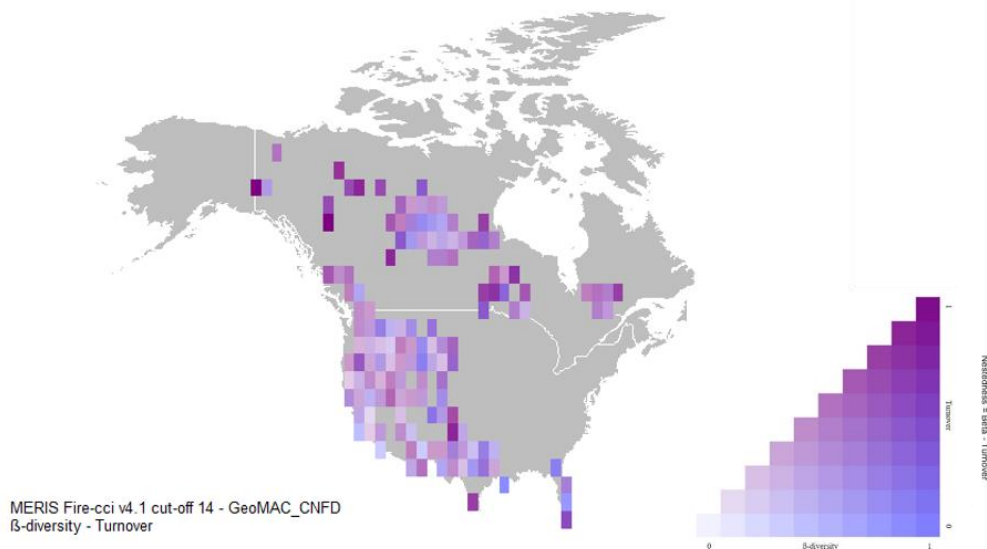


**Figure 20:** Colour composition of functional  $\beta$ -diversity ( $\beta$ -div), functional Turnover (Turn) and functional Nestedness (Nest) obtained from GeoMAC\_CNFD forest service and MERIS Fire\_cci v4.1 (FireCCI41) cut-off 14.

The same methodology was then applied to compare patch assemblages obtained from FireCCI41 and MCD64A1 collection 6 (Figure 21), represented on a colour composition legend. Dominance was found of “purplish” cases with a partial overlap, and corresponding to a translation of hypervolumes (case c and f from Vileger et al. 2013, Figure 19). The second dominant type of patch assemblage is the “bluish” case with a partial trait inclusion (case e from Vileger et al. 2013, Figure 19). In this case, extreme morphological traits are then captured by one sensor but not observed on the other. Most of these cases are found in the boreal forest and southwestern United States where most grassland fire occur. Likewise, as when comparing GeoMAC\_CNFD and FireCCI41 cut-off 14, ‘dark bluish’ and ‘dark purplish’ cases representing the higher disagreement, where mostly found in the boreal areas and south of United States.

Overall, both patterns (GeoMAC\_CNFD and FireCCI41 cut-off 14; FireCCI41 and MCD64A1 collection 6) present a similar direction but a different magnitude.

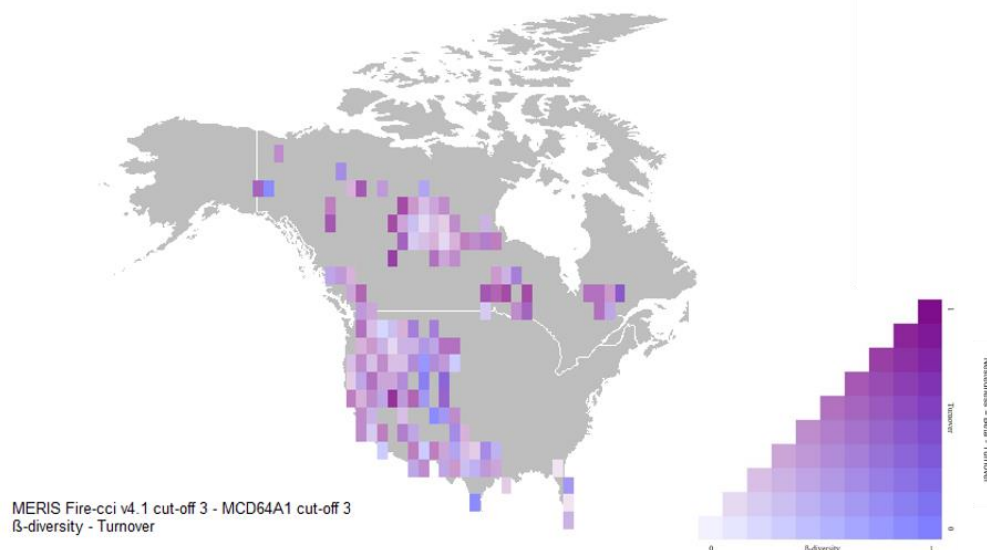


**Figure 21:** Colour composition of functional  $\beta$ -diversity ( $\beta$ -div), functional Turnover (Turn) and functional Nestedness (Nest) obtained from MERIS Fire\_cci v4.1 (FireCCI41) and MCD64A1 collection 6 cut-off 3.

Cases are better illustrated by plotting the n-dimensional hypervolumes of the two patch assemblages and their functional diversity indices. As a first study case, Figure 22 represents the ‘purplish’ case of partial overlap between two n-dimensional hypervolumes (tile with latitude = 52 and longitude = -93 from the map of Figure 21). The blue points represent patches obtained from FireCCI41 and the red points from MCD64A1 collection 6. In this case, fire types observed in one sensor are not observed in the other, mostly driven on area morphological feature, and as a consequence on direction and elongation traits. Figure 23 more particularly represents the FDis index as the sum of the distance between each fire patch on the trait axis and the barycentre of the assemblage, describing the dispersion of fire types within the FRic volume.

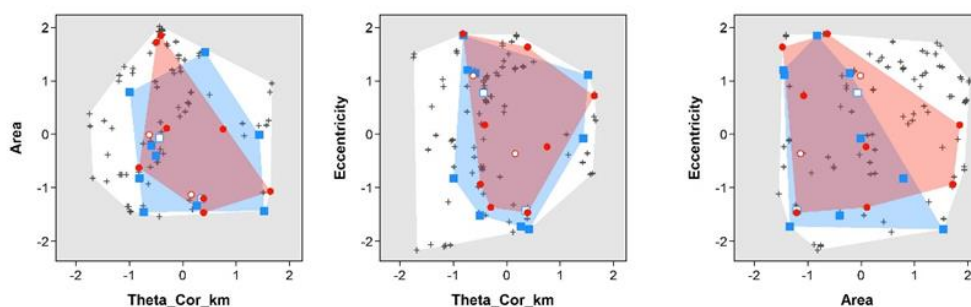


**Figure 22:** Example of (c) theoretical example of partial overlap from Villeger et al. 2013 obtained from MERIS Fire\_cci v4.1 (FireCCI41) (Blue) and MCD64A1 collection 6 (Red) cut-off 3 for a tile with latitude = 52 and longitude = -93. FireCCI41 + MCD64A1 collection 6 white convex hull.  $\beta$ -diversity ( $\beta$ -div) = 0.597, functional Turnover (Turn) = 0.466 and functional Nestedness (Nest) = 0.1.



fire  
cci

Fire\_cci  
Climate Assessment Report

Ref.: Fire\_cci\_D5.1\_CAR\_v1.4

Issue 1.4 Date 16/11/2018

Page 30

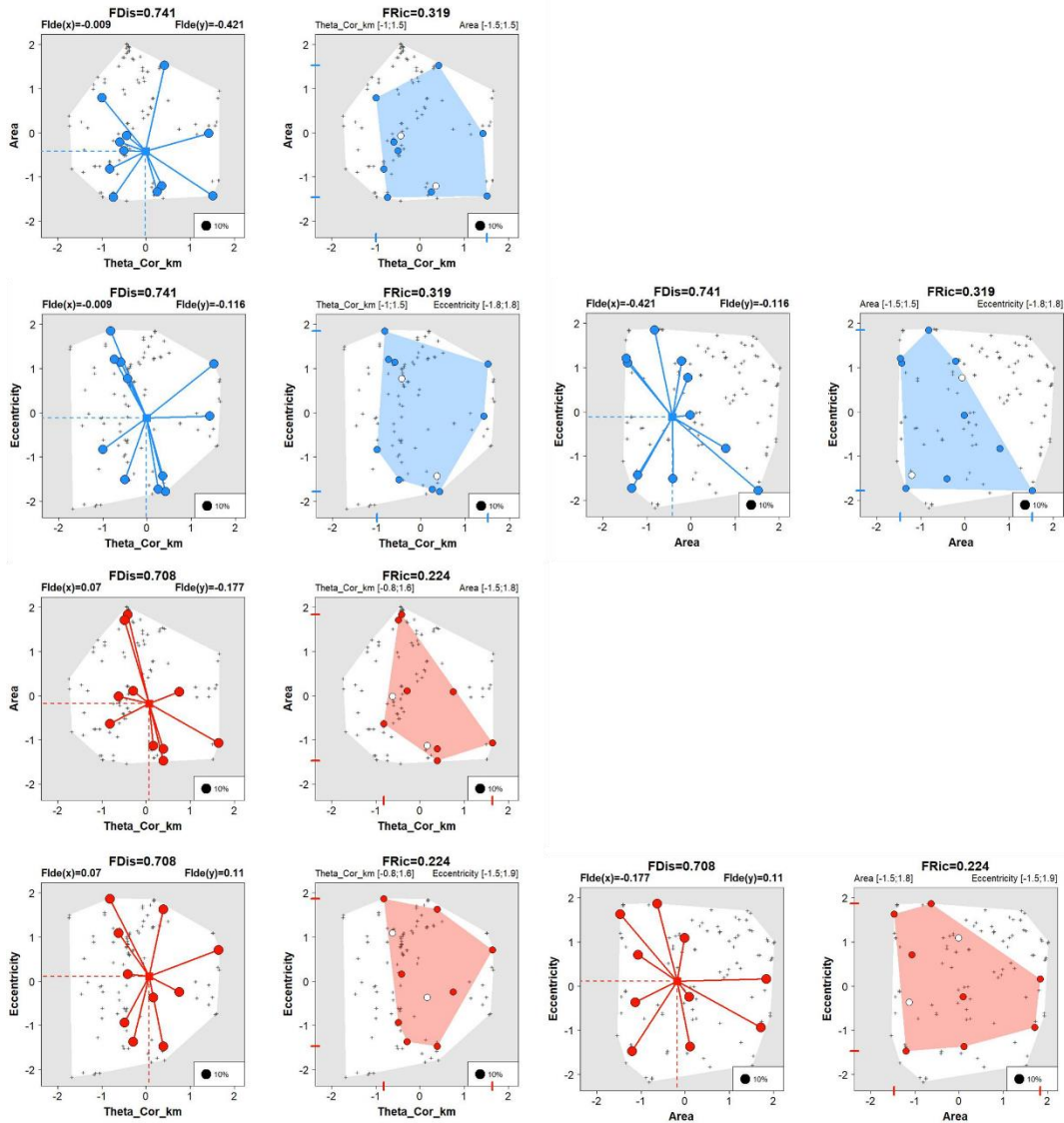


**Figure 23:** Example of functional diversity indices obtained from MERIS Fire\_cci v4.1 (FireCCI41) (Blue) and MCD64A1 collection 6 (Red) cut-off 3 for a tile with latitude = 52 and longitude = -93. Functional Richness (FRic) and Functional Dispersion (FDIs).

Figure 24 and Figure 25 represents the ‘bluish’ case with partial trait inclusion with high  $\beta$ -div and low Turn, suggesting the inclusion of a hypervolume within the other. In this case (tile with latitude = 27 and longitude = -81 from the map of Figure 21), two fires are observed on the MCD64A1 collection 6 (red circles) with high values on area, and not observed on FireCCI41 sensor (blue circles), so that two large fires are captured by MCD64A1 collection 6 and not in FireCCI41 sensor (blue circles). This peculiar case indicates an extreme case of fire morphological traits where they are built from the pixel level information in one sensor and not the other, highlighting potential sensibilities of the flood fill algorithm to different burn dates registered in the sensors. Despite high differences in the hypervolumes generated from the two sensors, and due to few extreme fire shapes, the overall FDis is mostly driven by the numerous smaller fires so that these indices are quite similar between the products.





fire  
cci

Fire\_cci  
Climate Assessment Report

Ref.: Fire\_cci\_D5.1\_CAR\_v1.4

Issue 1.4 Date 16/11/2018

Page 31

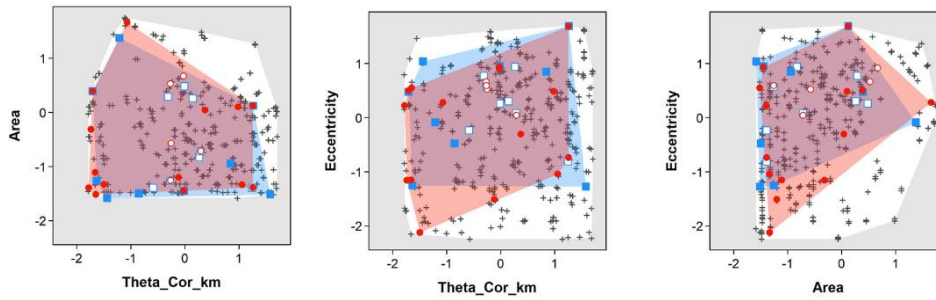


**Figure 24:** Example of (e) theoretical example partial trait inclusion from Villegier et al. 2013 obtained from MERIS Fire\_cci v4.1 (FireCCI41) (Blue) and MCD64A1 collection 6 (Red) cut-off 3 for a tile with latitude = 27 and longitude = -81. FireCCI41 + MCD64A1 collection 6 white convex hull.  $\beta$ -diversity ( $\beta$ -div) = 0.278, functional Turnover (Turn) = 0.230 and functional Nestedness (Nest) = 0.049.

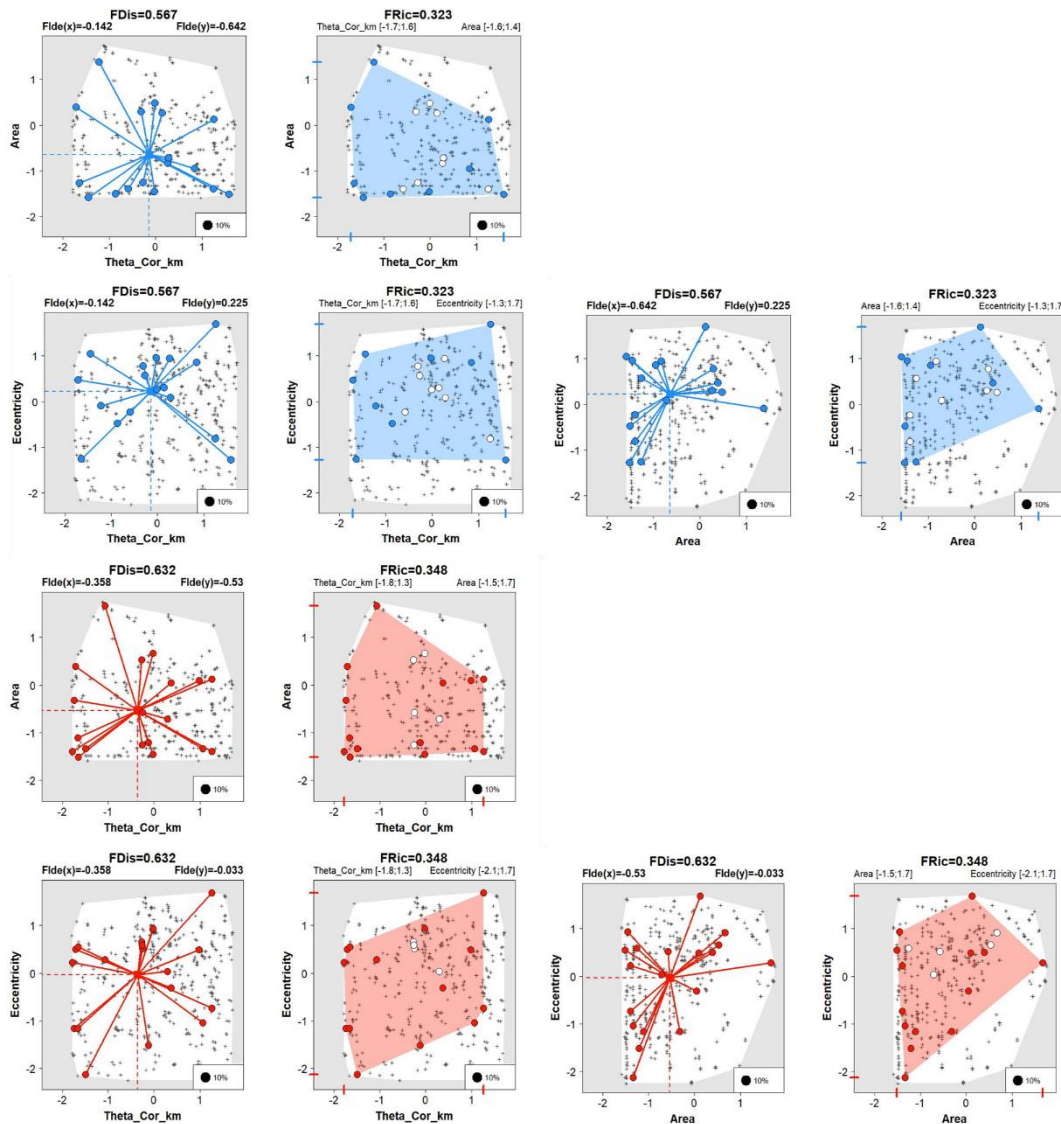


**Figure 25:** Example of functional diversity indices obtained from MERIS Fire\_cci v4.1 (FireCCI41) (Blue) and MCD64A1 collection 6 (Red) cut-off 3 for a tile with latitude = 27 and longitude = -81. Functional Richness (FRic) and Functional Dispersion (FDis).

From this continental scale analysis and our statistical framework based on fire patch morphological features derived from the pixel level information delivered in global BA products, the following conclusions can be obtained:

 <b>fire</b> cci	<b>Fire_cci</b> Climate Assessment Report		Ref.:	Fire_cci_D5.1_CAR_v1.4		
			Issue	1.4	Date	16/11/2018
					Page	32

- The statistical framework of comparative ecology applied to pyrogeography is a useful tool to compare assemblages of fire patches, synthesizing complex information into few meaningful indices.
- The comparison between FireCCI41 and MCD64A1 collection 6 could lead to encouraging conclusions on the matching between the two products. The spatial pattern of patch assemblage at the continental scale is conserved across products. A potential bias on extreme fire sizes was noticed, affecting the FRic component of the comparison, so that extreme fire shapes can be identified in one product and not the other. Again, the sensitivity of the statistical framework to identify these discrepancies should be valued. Overall, however, the other component of the functional indices revealed similar values across remote sensing products indicating a general agreement in detecting patch assemblages. Differences in large patches can arise from uncertainties in the burn date and the sensitivity of the flood fill algorithm to this variable rather than uncertainties in the burned pixel detection between products. The patch identification derived from pixel-level products, both MCD64A1 collection 6 and FireCCI41, should be taken into consideration, leading to similar mismatches with local observations for extreme fire shapes.

### 3.3. At the global scale

Based on previous results at the local level in the Brazilian Savanna and at the continental level in North America, similar analyses were performed on  $1^\circ \times 1^\circ$  resolution tiles at global scale. Global morphological fire patch products from the FRY database (Laurent et al. 2018) at cut-offs 3, 5, 9 and 14 were used. Each cut-off product were derived from FireCCI41 and MCD64A1 collection 6 BA products. Thus, the spatial global pattern of the FRic and FDis between 8 products were analysed by testing for linear grid-cell to grid-cell relationships on global maps and by analysing the trait hyper-volume dissimilarities with the  $\beta$ -div index. To study the differences between products sources and the impact of the cut offs, an inter comparison between the cut-off products based on both sensors and an intra comparison within the cut-off products based on the same sensor were included in the analysis.

The intra comparison of the products based on MERIS BA product (FireCCI41) showed a similar spatial pattern with the different cut-off thresholds. High FRic was found across biomes with high burned area such as savanna, chaparral, and temperate forest and grassland indicating more extreme morphological fire trait values when burned area is high. Medium-low FRic was found spatially dispersed in the boreal forest and in the borders between savannas and tropical forests (Figure 26). On the contrary, medium FDis was found in the savannas indicating that most fires have average morphological traits. Higher FDis was found in the temperate and boreal forest indicating that extreme trait values are more frequent than average ones.



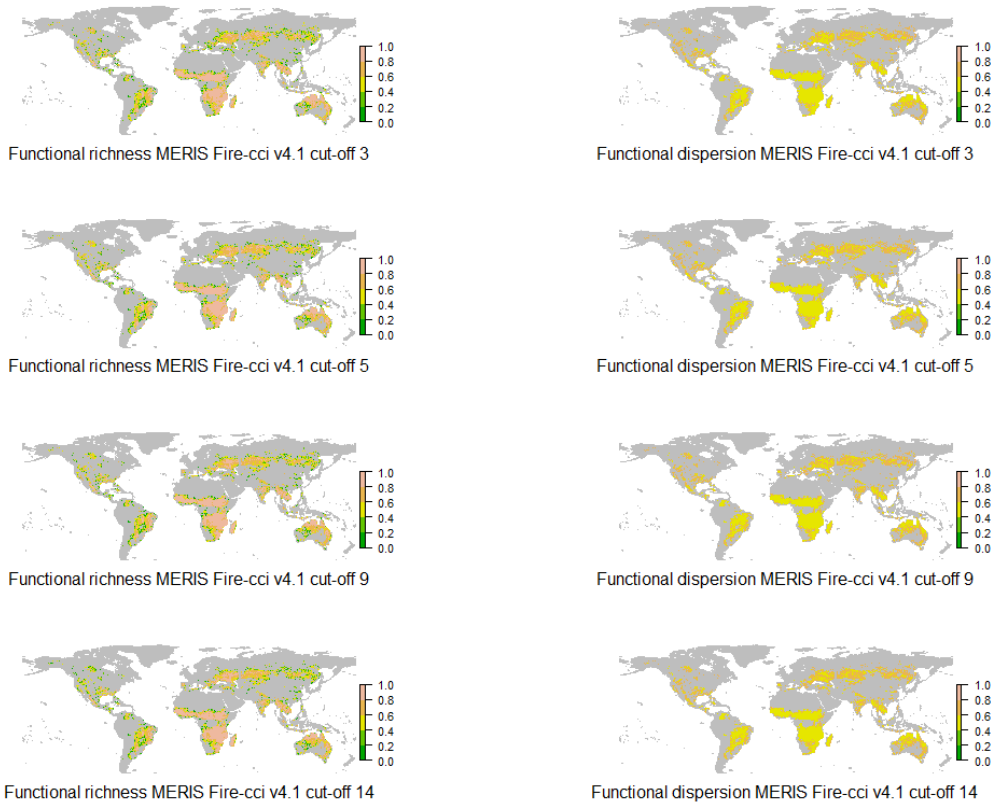


**Figure 26:** Functional Richness (FRic; (Left) and Functional Dispersion (FDis; Right) obtained from MERIS Fire\_cci v4.1 (FireCCI41) cut-off 3, 5, 9 and 14.

Consequently, strong and statistically significant ( $p$ -values  $< 0.001$ ) bivariate relationships between FireCCI41 FRic cut-offs (3, 5, 9, and 14) and between FDis cut-offs (3, 5, 9, and 14) were found (Figure 27). Closer cut-off values experienced higher correlations indicating low differences between two subsequent cut-offs for both FRic and Fdis, but substantial differences when comparing extreme cut-offs values of 3 and 14.

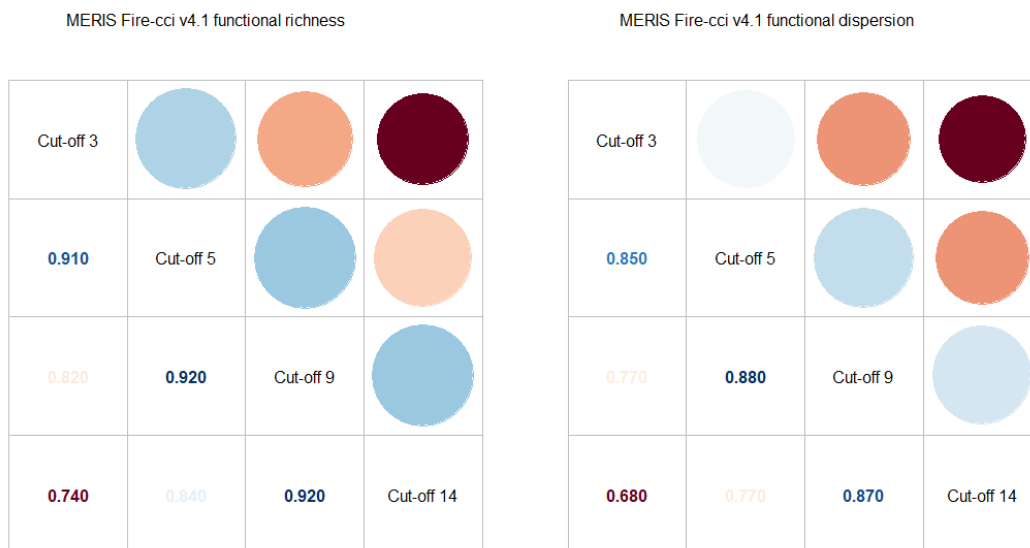


**Figure 27:**  $R^2$  ( $p$ -value  $< 0.001$ ) of the bivariate relationship of Functional Richness (FRic; Left) and Functional Dispersion (FDis; Right) obtained from MERIS Fire\_cci v4.1 (FireCCI41) at different cut-offs 3, 5, 9 and 14.

Likewise, the dissimilarity of the trait hyper-volumes between the FireCCI41 cut-offs 3, 5, 9 and 14 was mostly low (Figure 28) and  $\beta$ -div slightly decreased with medium and high cut-offs. High  $\beta$ -div was found mostly in the temperate and boreal forest driven by a general high Turn (e.g. dark purplish grid cells in Figure 29) indicating low overlap between trait hyper-volumes. Same pattern was observed in Asia and more sparsely over the south hemisphere when comparing extreme cut-offs.

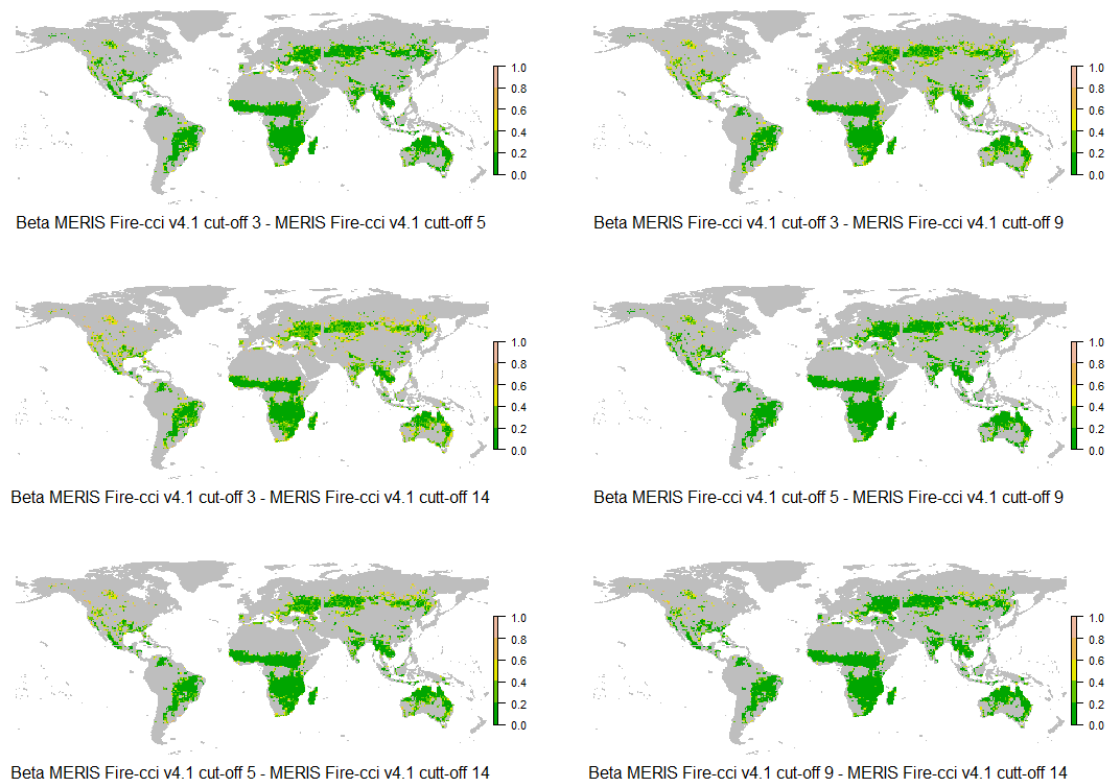


**Figure 28:** Functional  $\beta$ -diversity ( $\beta$ -div) maps at global scale obtained from MERIS Fire\_cci v4.1 (FireCCI41) cut-offs 3, 5, 9 and 14.

The dissimilarity between the FireCCI41 cut-offs is lower between contiguous cut-offs (Figure 28), suggesting that using extreme cut-offs may lead to high variability in the analysis of fire patches. A better matching between medium cut-offs is suggesting, that using cut-off 5 or 9 at global scale would lead to similar fire patch analysis (Figure 29).

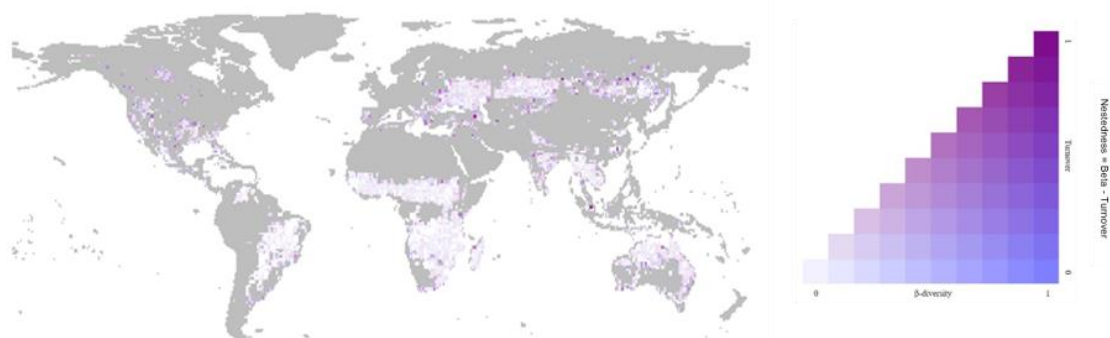


**Figure 29:** Colour composition of functional  $\beta$ -diversity ( $\beta$ -div), functional Turnover (Turn) and functional Nestedness (Nest) obtained from MERIS Fire\_cci v4.1 (FireCCI41) cut-off 5-9.

The intra comparison of the products based on MODIS BA products (MCD64A1 collection 6) showed a similar spatial pattern with the different cut-off thresholds (Figure 30) as found in FireCCI41. In distinction to FireCCI41, MCD64A1 collection 6 showed much less grid cells with low FRic in the south hemisphere. Low FRic was found mostly in the temperate and boreal forests, as well as in the southeast and equatorial Asia. Besides, MCD64A1 collection 6 showed much less grid cells with high FDis in the north hemisphere, being located mostly in the temperate forest and grassland.

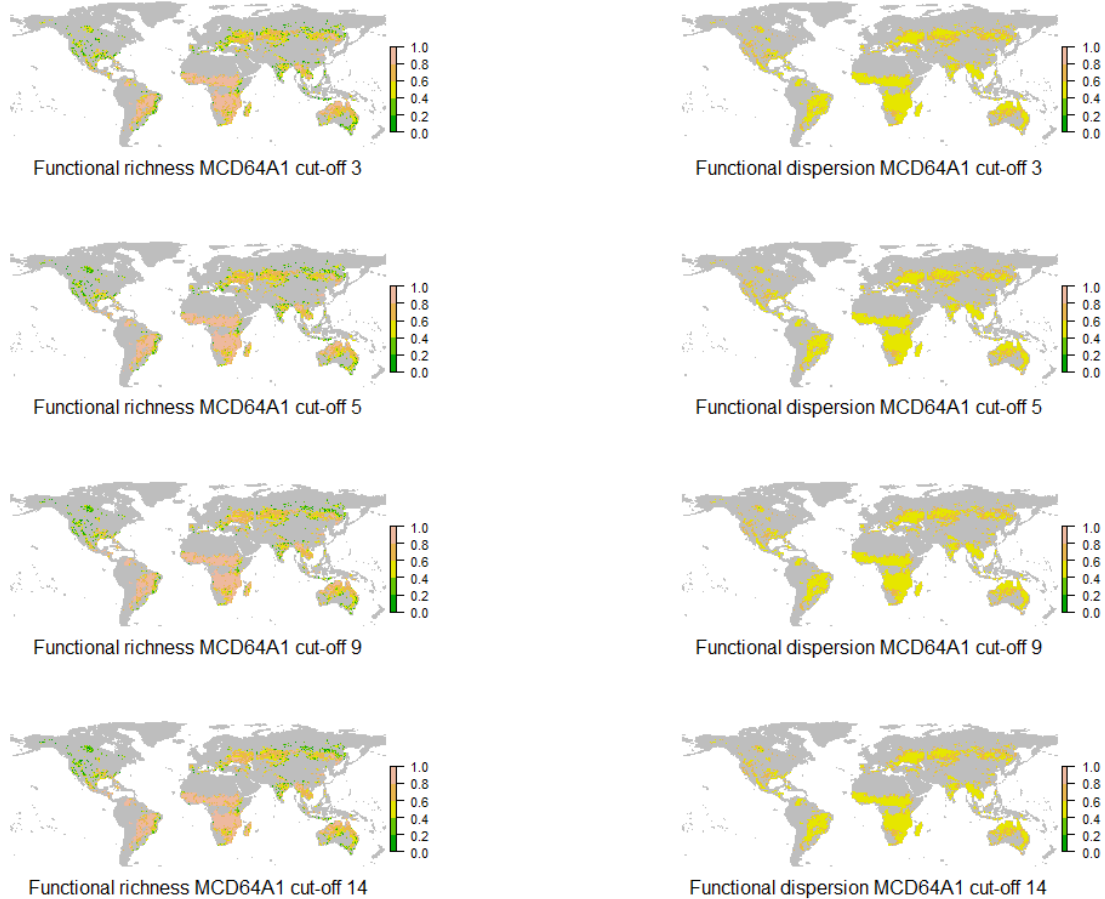


**Figure 30:** Functional Richness (FRic; (Left) and Functional Dispersion (FDis; Right) obtained from MCD64A1 collection 6 cut-off 3, 5, 9 and 14.

Thus, strong and statistically significant ( $p$ -values  $< 0.001$ ) bivariate relationships between MCD64A1 collection 6 FRic cut-offs (3, 5, 9, and 14) and between MCD64A1 collection 6 FDis cut-offs (3, 5, 9, and 14) were found (Figure 31). The spatial global pattern of FRic and FDis generated with cut-off 9 were the most correlated to cut-off 14, with respectively  $r^2$  0.97 and  $r^2$  0.95. The spatial global pattern of FRic and FDis generated with cut-off 3 were the least correlated to cut-off 14 for both FRic and FDis with respectively  $r^2$  0.74 and  $r^2$  0.68.

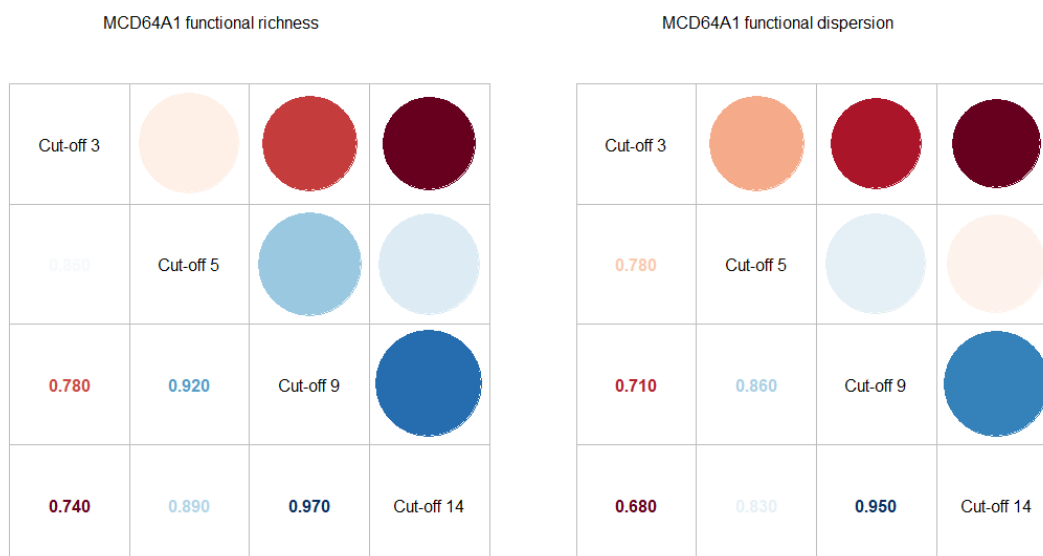


**Figure 31:**  $R^2$  ( $p$ -value < 0.001) of the bivariate relationship of Functional Richness (FRic; Right) Functional Dispersion (FDis; Left) obtained from MCD64A1 collection 6 at different cut-offs 3, 5, 9 and 14.

When comparing the dissimilarities between the MCD64A1 collection 6 cut-offs 3, 5, 9 and 14, we observed low (Figure 32)  $\beta$ -div slightly decreasing with high cut-offs. High  $\beta$ -div was found mostly in the temperate and boreal forests driven by high Turn (e.g. dark purplish grid cells in Figure 33) and locally a high Nest in central Canada (e.g. dark bluish grid cells in Figure 33).

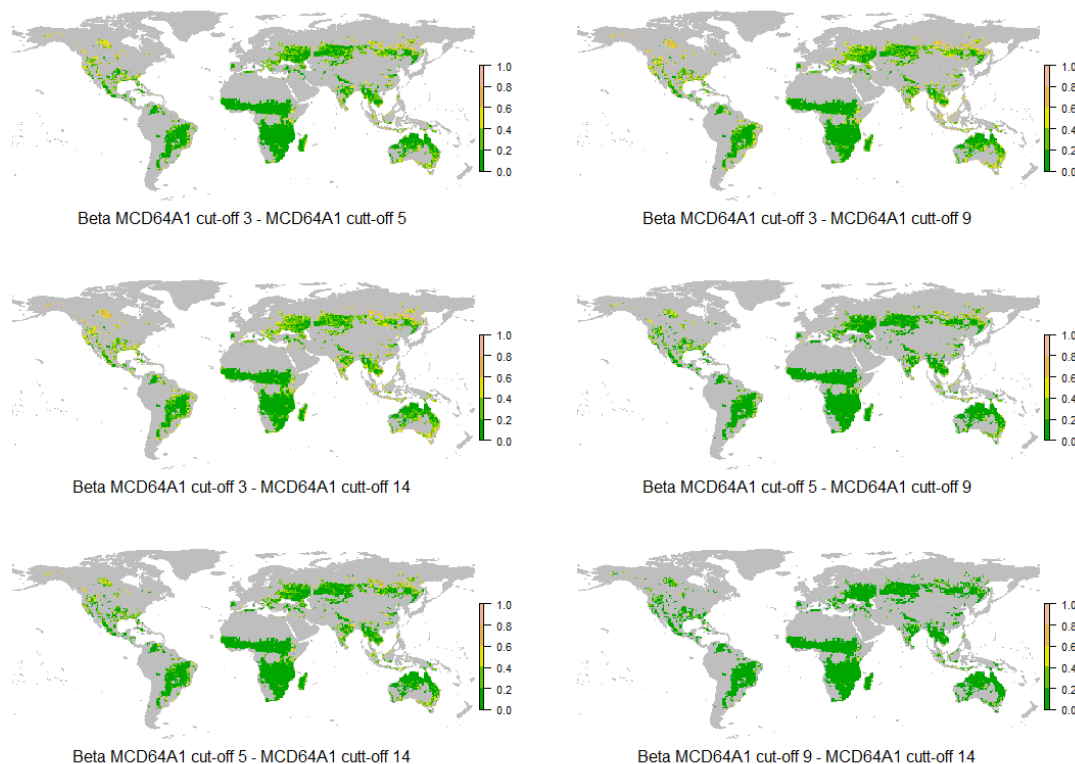


**Figure 32:** Functional  $\beta$ -diversity ( $\beta$ -div) maps at global scale obtained from MCD64A1 collection 6 cut-offs 3, 5, 9 and 14.

The dissimilarity between the MCD64A1 cut-off 3 and 5 is higher than when comparing FireCCI41 cut-offs, suggesting that given the shorter temporal resolution of MODIS, small cut-off values may generate more variability in fire patches construction than FireCCI41. On the contrary, the good match between higher cut-offs in MCD64A1 is suggesting that using cut-off 9 and 14 at global scale provide similar information in terms of fire shape (Figure 33) compared to FireCCI41 for which the differences between cut-offs 9 and 14 still relevant.

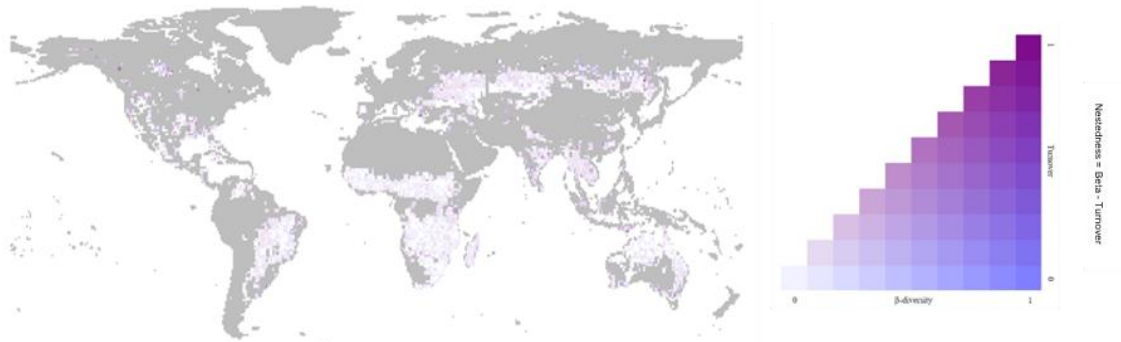


**Figure 33:** Colour composition of functional  $\beta$ -diversity ( $\beta$ -div), functional Turnover (Turn) and functional Nestedness (Nest) obtained from MCD64A1 collection 6 cut-off 9-14.

The inter comparison of the FRic and FDis generated from MERIS (FireCCI41) and MODIS (MCD64A1 collection 6) BA products with cut offs 3, 5, 9 and 14 showed weak but statistically significant ( $p$ -values  $< 0.001$ ) bivariate spatial relationships (Figure 34). For FRic, highest correlations ( $r^2 > 0.08$ ) were observed between MCD64A1 cut-off 3 with all cut-off values of FireCCI41 and, between FireCCI41 cut off 14 and all cut-off values of MCD64A1. This result suggests that low cut-offs used for fireCCI41 (experiencing the lowest temporal resolution) generate high discrepancies with MCD64A1 regarding extreme morphological traits.

For FDis, correlations are higher than FRic ( $r^2 > 0.25$ ) but still low, and they are almost similar whatever the cut-offs and the products. This suggests lower effects of cut-offs and products fire patches with average fire traits composing the hyper-volumes than on extremes as identified with FRic.



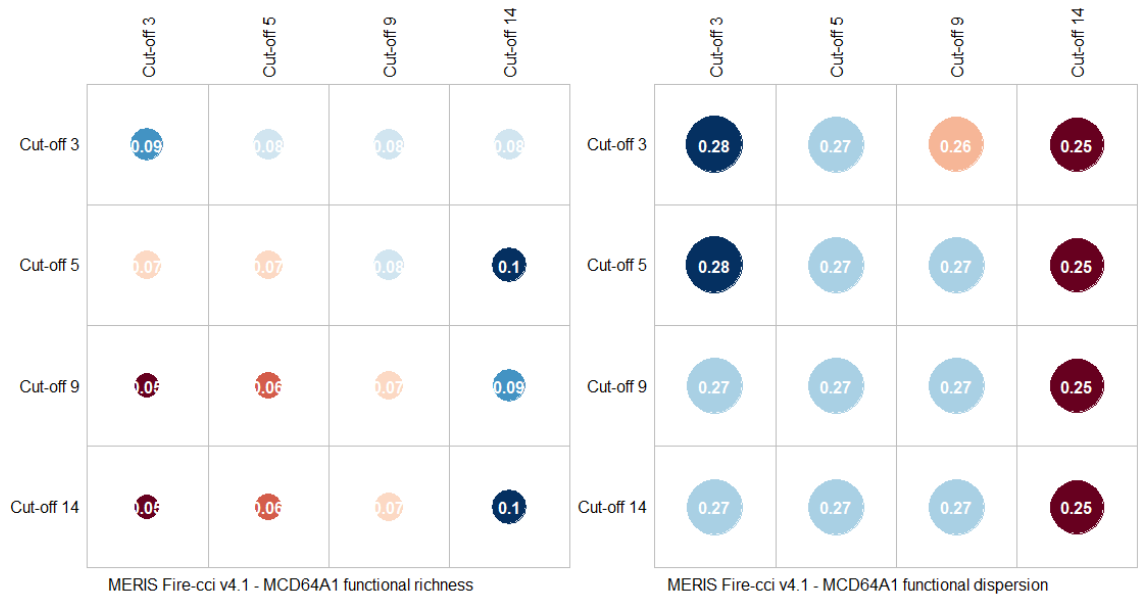


**Figure 34:**  $R^2$  (p-value < 0.001) of the bivariate relationship of Functional Richness (FRic; Left) Functional Dispersion (FDis; Right) obtained from MERIS Fire\_cci v4.1 (FireCCI41; Top) and MCD64A1 collection 6 (Left) at different cut-offs 3, 5, 9 and 14.

The dissimilarity between FireCCI41 and MCD64A1 collection 6 cut-offs 3, 5, 9 and 14 was diverse (Figure 35 and Figure 36). Low  $\beta$ -div was found in areas with a high burned area, while high  $\beta$ -div was found not only in areas with high fire activity, but also medium and low fire activity, a somewhat similar pattern and values as observed with the intra-product comparison. Fire patches generated by pixel-level burn date are then similarly sensitive to sensors and cut-off values.

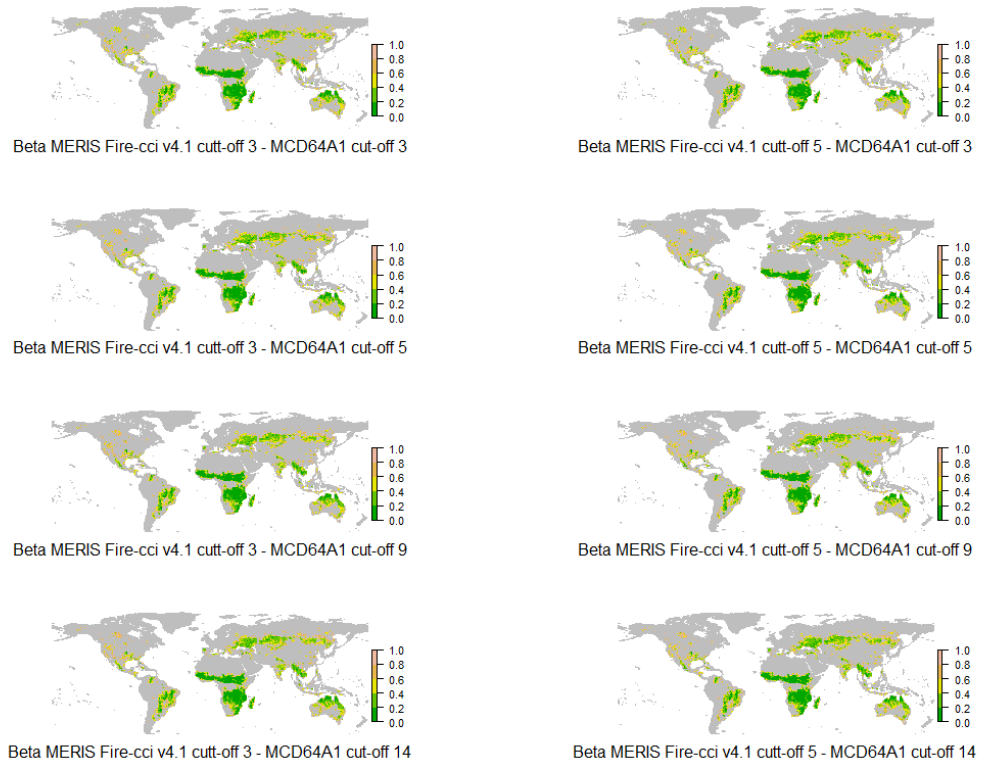


**Figure 35:** Functional  $\beta$ -diversity ( $\beta$ -div) maps at global scale obtained from MERIS Fire\_cci v4.1 (FireCCI41) cut-offs 3 (Left) and 5 (Right) and MCD64A1 collection 6 cut-offs 3, 5, 9 and 14.

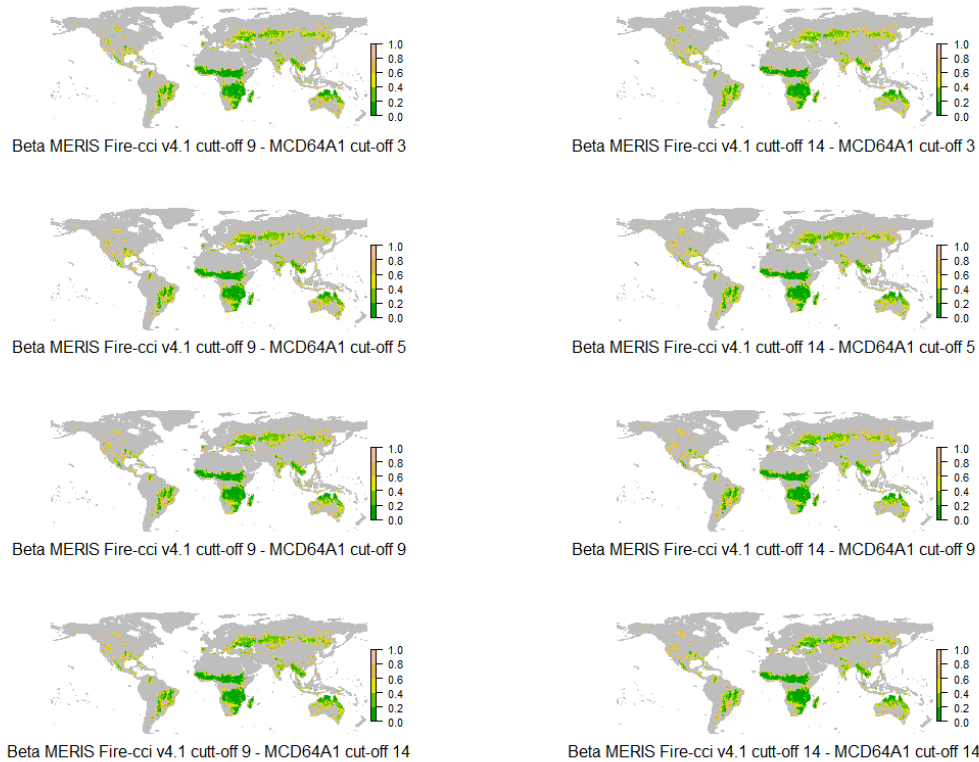


**Figure 36:** Functional  $\beta$ -diversity ( $\beta$ -div) maps at global scale obtained from MERIS Fire\_cci v4.1 (FireCCI41) cut-offs 9 (Left) and 14 (Right) and MCD64A1 collection 6 cut-offs 3, 5, 9 and 14.

High  $\beta$ -div located in tropical Asia, temperate and boreal forests as well as in the Australian savannas, was driven by a high Turn (e.g dark purplish grid cells in Figure 37), so that the fire trait hyper-volumes tend to only partly overlap. High  $\beta$ -div located in the tropical forest and savannas in the south hemisphere, was driven by a high Nest (e.g dark bluish grid cells in Figure 38), suggesting that the fire trait hyper-volume from one sensor is included in the other, with missing some fire types.

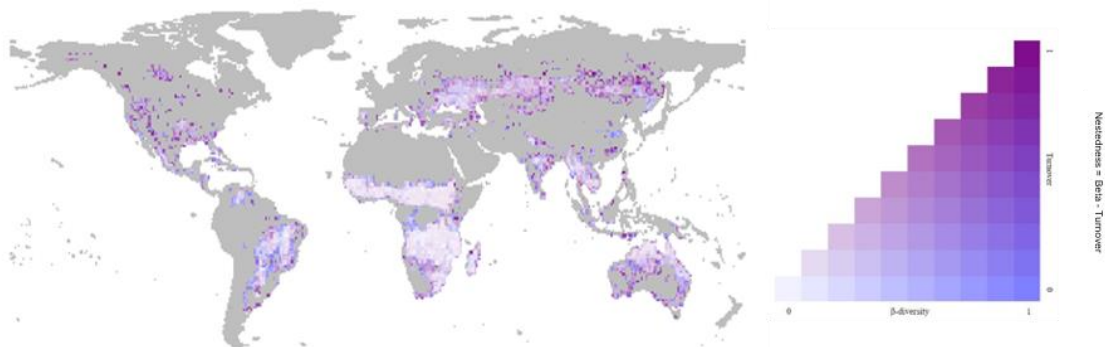


**Figure 39:** Colour composition of functional  $\beta$ -diversity ( $\beta$ -div), functional Turnover (Turn) and functional Nestedness (Nest) obtained from FireCCI41 cut-off 14 and MCD64A1 collection 6 cut-off 5.

Similarly when comparing the global spatial pattern between FireCCI41 and MCD64A1 collection 6 fire patches products, the mismatches between the products evidence the different characteristics of the BA products based on MERIS and MODIS sensors, but may be also the burn date uncertainties. For example, a high translation between the

	<b>Fire_cci</b> <b>Climate Assessment Report</b>		Ref.:	Fire_cci_D5.1_CAR_v1.4	
			Issue	1.4	Date
					Page

volumes may be related with extreme cases of fire morphological traits besides burn date uncertainties as in boreal forest, when fires may burn for long time and where ground fires may re-burn after a while. Thus, a high inclusion between the volumes may be related with the fact that fire patches based on MERIS are generally more fragmented than fire patches based on MODIS BA products, as in between tropical forest and savannas where fires tend to be large.

From this global scale analysis, the following conclusions can be obtained:

- The trait-based approach describing functional spaces of fire patch morphological traits reveal similar global patterns of patch assemblages between FireCCI41 and MCD64A1 collection 6, with peculiar correspondences between products regarding their cut-offs values.
- Diversity (FRic) of fire morphological traits is higher in areas of high burned area.
- Dispersion (FDis) of fire patches in the morphological traits space is higher in areas of low to medium burned area.
- Even if the general spatial pattern along the cut-offs is maintained, within FireCCI41 cut-offs, medium are the more similar ones, while within MCD64A1 collection 6, high ones are the more similar ones.
- Fire patches based on MERIS are more fragmented than patches based on MODIS.
- Fire patches derived from burned-date at the pixel level are similarly sensitive to sensors and cut-off values.
- The global relationships observed between MCD64A1 and FireCCI41 fire patches may change across regions, for example, in boreal or temperate forests in North America.

#### **4. Uncertainty on fire patch morphology: comparing the assemblage of patches between different BA products and between cut-off thresholds for a given BA product**

##### **4.1. Morphological traits and power law maps**

The resulting fire patch databases from the FireCCI41, FireCCI50 and SFD BA products were compared with the MCD45A1 collection 5 (only for FireCCI41) and MCD64A1 collection 6 products. The focus was put on fire frequency and 3 metrics from the database which are sufficient to represent most of the complexity of fire patch shapes: the fire size (computed from the standard deviation ellipse), the ellipse ratio and the shape index (from pixel data). For each of these quantities, their mean value and standard deviation in  $1^\circ \times 1^\circ$  grids were computed. Fire patches with less than 5 cells were removed, because they do not allow computing reliable fire morphological traits. Since the effective size (in hectares) of a 5-pixel fire decreases toward high latitudes, for each product all fire patches smaller than the area of a 5-pixel fire patch at nadir were removed. This corresponds to a fire size of 27 ha for FireCCI50, 45 ha for FireCCI41, and 107 ha for MODIS.

The relation between the fire frequency  $N_f$  and the fire size  $A_f$  was studied. Many studies have tried to explain fire size distribution with self-organized criticality (SOC) (Bak 1987, Malamud 1998, Clar et al. 1999). In these models, the relation between  $N_f$  and  $A_f$  follows a power law:

$$N_f = \alpha \cdot A_f^{-\beta}$$

where  $\alpha$  is a normalization constant and  $\beta$  is the exponent of the power law. SOC models predict a constant value of  $\beta$ , but numerous analyses have detected significant variations of this parameter at a global scale (Pueyo 2007, Hantson et al. 2015). It is therefore necessary to investigate potential discrepancies between different BA products and different patch reconstruction techniques.

For each fire patch database, the parameter  $\beta$  was fitted in a global  $1^\circ \times 1^\circ$  grid. For each cell, the following procedure was performed:

1. The profile histogram of  $N_f$  and  $A_f$  was produced, which is defined as the normalized number of fires  $N_f$  for different logarithmic bins of fire size.
2. A Poisson uncertainty equal to the square root of the number of fire patches in each size bins was attributed to each value of the profile histogram.
3. The power law was then fitted by using the Minuit minimization algorithm (<https://seal.web.cern.ch/seal/snapshot/work-packages/mathlibs/minuit/>, accessed March 2017), which provides an efficient way to realize chi-squared minimization.

An example of fit is displayed on Figure 40. The map of the uncertainty on  $\beta$ ,  $\sigma_\beta$ , and the chi-squared value were also produced because they are necessary to assess the quality of fit. Figure 41 shows the comparison of the  $\beta$  parameter when computed from  $A_{\text{ellipse}}$  or  $A_{\text{pixel}}$ . For FireCCI41,  $\beta$  is slightly higher when computed from the elliptical shape than when computed from the pixel shape. This difference is even higher for MCD45A1 collection 5 and MCD64A1 collection 6.

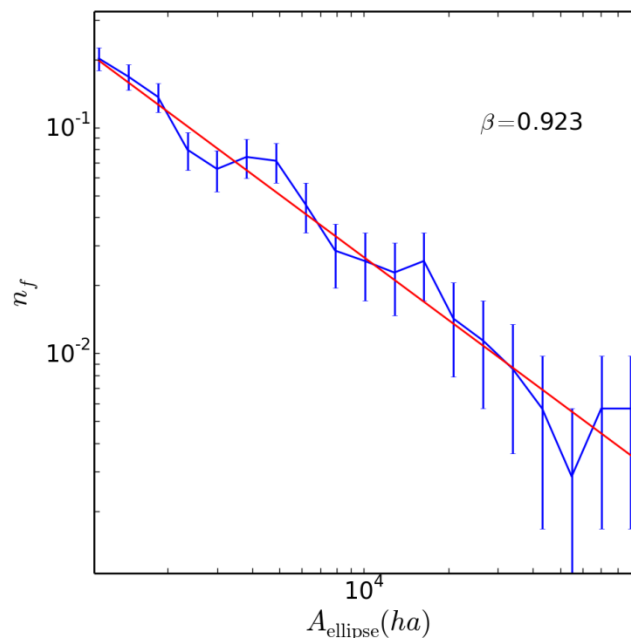


**Figure 40:** Example of a power law fit



Fire\_cci  
Climate Assessment Report

Ref.: Fire\_cci\_D5.1\_CAR\_v1.4

Issue 1.4 Date 16/11/2018

Page 42

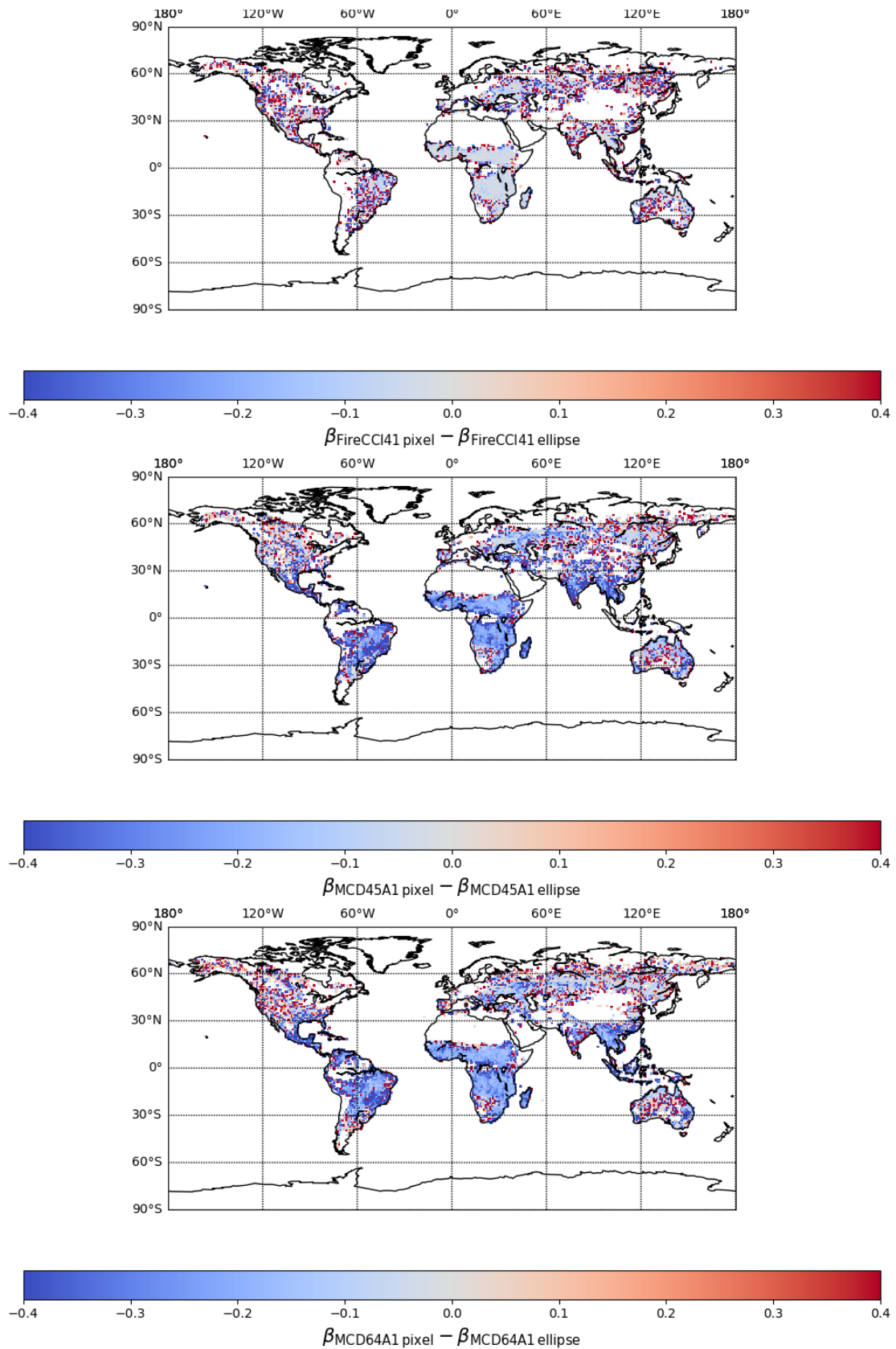


**Figure 41:** Difference between  $\beta$  parameter computed from  $A_{\text{ellipse}}$  and from  $A_{\text{pixel}}$  from FireCCI41 (top), MCD45A1 collection 5 (middle) and MCD64A1 collection 6 (bottom).





## 4.2. Comparison between BA global products

### 4.2.1. Comparison between FireCCI41, MCD45A1 and MCD64A1

Figure 42 displays the fire density maps for the FireCCI41, MCD45A1 collection 5 and the difference between the two products, for a cut-off value of 5. The maps for MCD64A1 collection 6, and the difference between this product and FireCCI41 are displayed in Figure 43. When the difference between FireCCI41 and one of the MODIS products is computed, the MODIS product was always restrained to the years 2005-2011. For all products, the pattern of fire density follows burned area: the highest values are reached in Africa (Northern (NHAF) and Southern (SHAF)), followed by South America (Southern Hemisphere (SHSA)), the northern part of Australia and central Eurasia. When comparing FireCCI41 and MCD45A1 collection 5 over the years 2005 to 2011, FireCCI41 exhibits a significantly higher fire patch density than MODIS for the aforementioned regions, excepted for the western part of SHAF and some areas in SHSA. This is probably due to the missing data in MERIS imagery for these regions. MCD45A1 also yields more fire patches in North America agricultural regions, in central Asia (CEAS) and in the NHAF regions close to the rainforest or the Sahelian region. The results are very similar when comparing FireCCI41 to the MCD64A1 collection 6 derived database, excepted for Central Asia and North America where the agreement is better than with MCD45A1. This could arise from missed burnt pixel seeds by the Fire\_cci algorithm. The 3-day time of overpass can lower the probability to match burned pixels detected by MERIS imagery with active fire pixels from MODIS if there is a strong delay between the two detections. This suggests that the temporal resolution of the sensors is an important parameter for detecting individual fire events when using a two-step algorithm approach to detect BA.

The resulting maps of the  $\beta$  parameters for MCD45A1 collection 5 and FireCCI41 are shown in Figure 44 with their uncertainties, the difference between the two products, and the level of agreement in number of standard deviation. The lower limit of the fit range of all products is 107 ha, and the upper limit is 100 000 ha for all products. The difference between the  $\beta$  parameter from the Fire\_cci and MCD45A1 collection 5 products is also shown. As for fire density, the structure of the  $\beta$  parameter is similar between the two fire patch datasets, with higher values in NHAF, SHAF, India, central Eurasia and southern Brazil. The high value of  $\beta$  means that the proportion of small fires with respect to the number of big fires is higher in these regions. The uncertainty on the  $\beta$  parameter closely follows the spatial distribution of fire density because a higher number of fires in a sub-cell yield a smaller Poisson uncertainty, and therefore, a smaller uncertainty on the  $\beta$  parameter. The value of the  $\beta$  parameter is globally higher (which corresponds to a steeper power law) for FireCCI41 than for MCD45A1 collection 5. Under the assumption that the probability of missing big fires is low, this means that, due to its better resolution, the FireCCI41 product detects a higher number of small fires than the MODIS product. The results are similar when switching MCD45A1 with MCD64A1.



fire  
cci

Fire\_cci  
Climate Assessment Report

Ref.: Fire\_cci\_D5.1\_CAR\_v1.4

Issue 1.4 Date 16/11/2018

Page 44

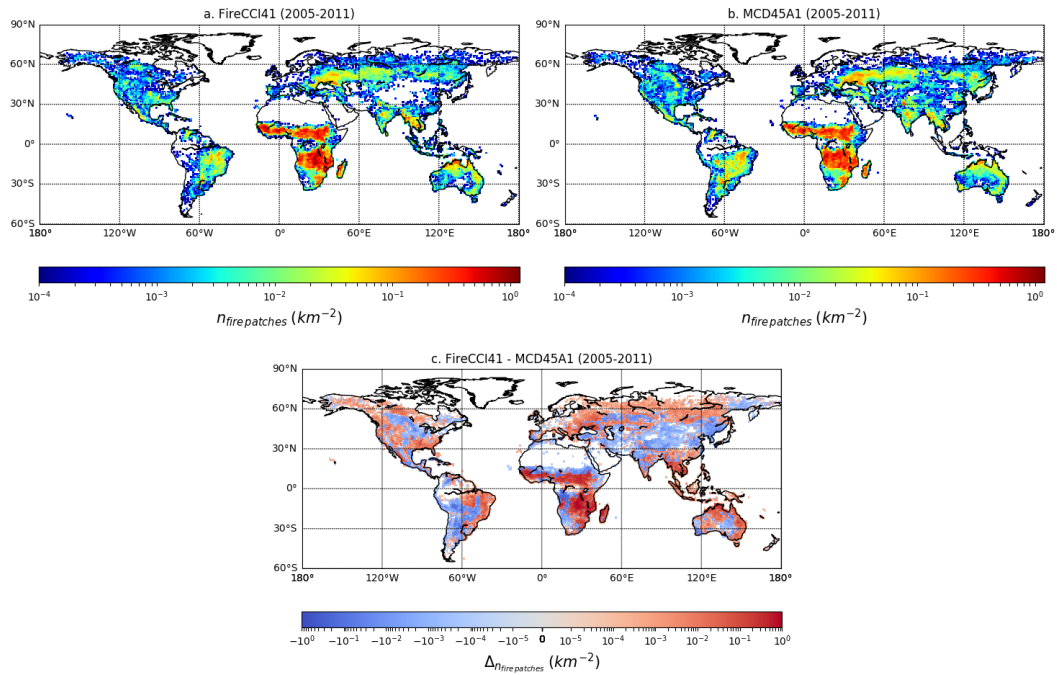


**Figure 42:** Fire density ( $km^{-2}$ ) for FireCCI41 (top left), and MCD45A1 collection 5 (top right). The difference between the two products is displayed for the years 2005-2011.

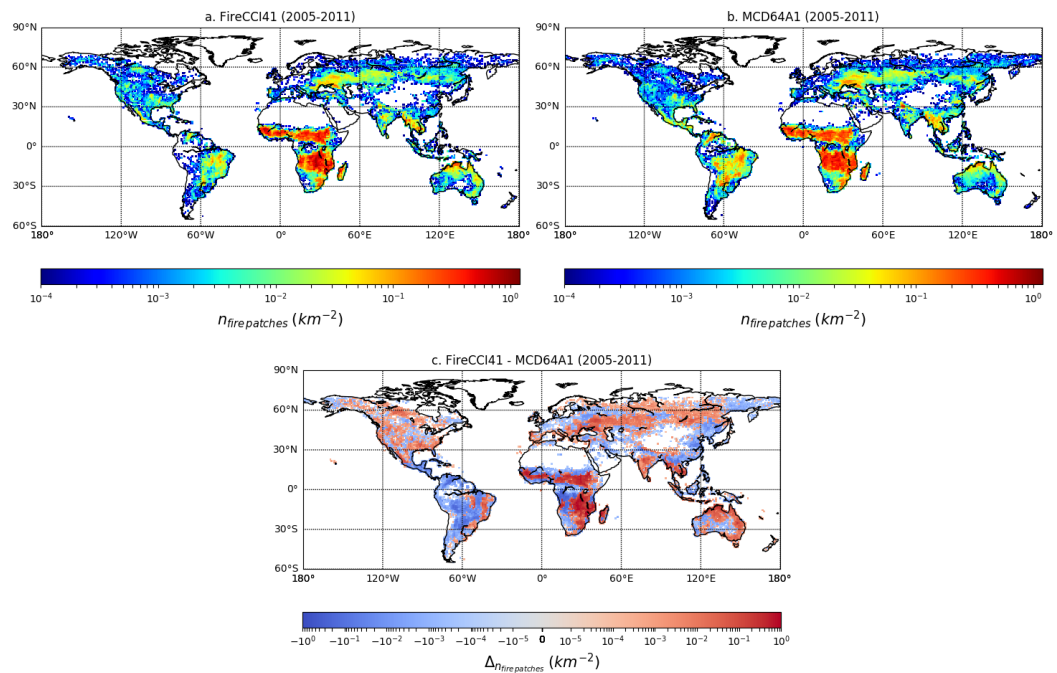
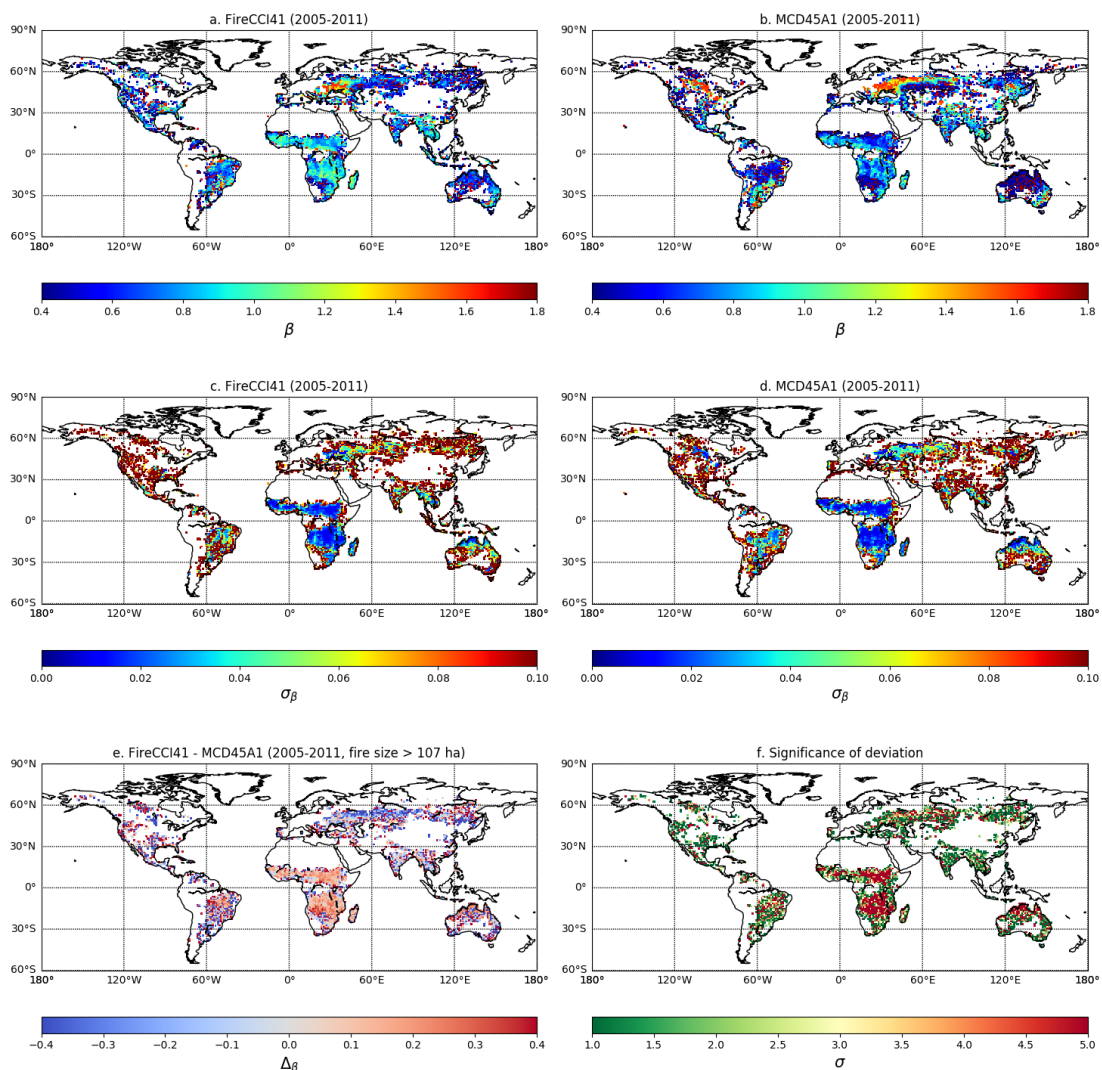


**Figure 43:** Same as **Figure 42**, with the MCD64A1 collection 6 product instead of MCD45A1 collection 5.

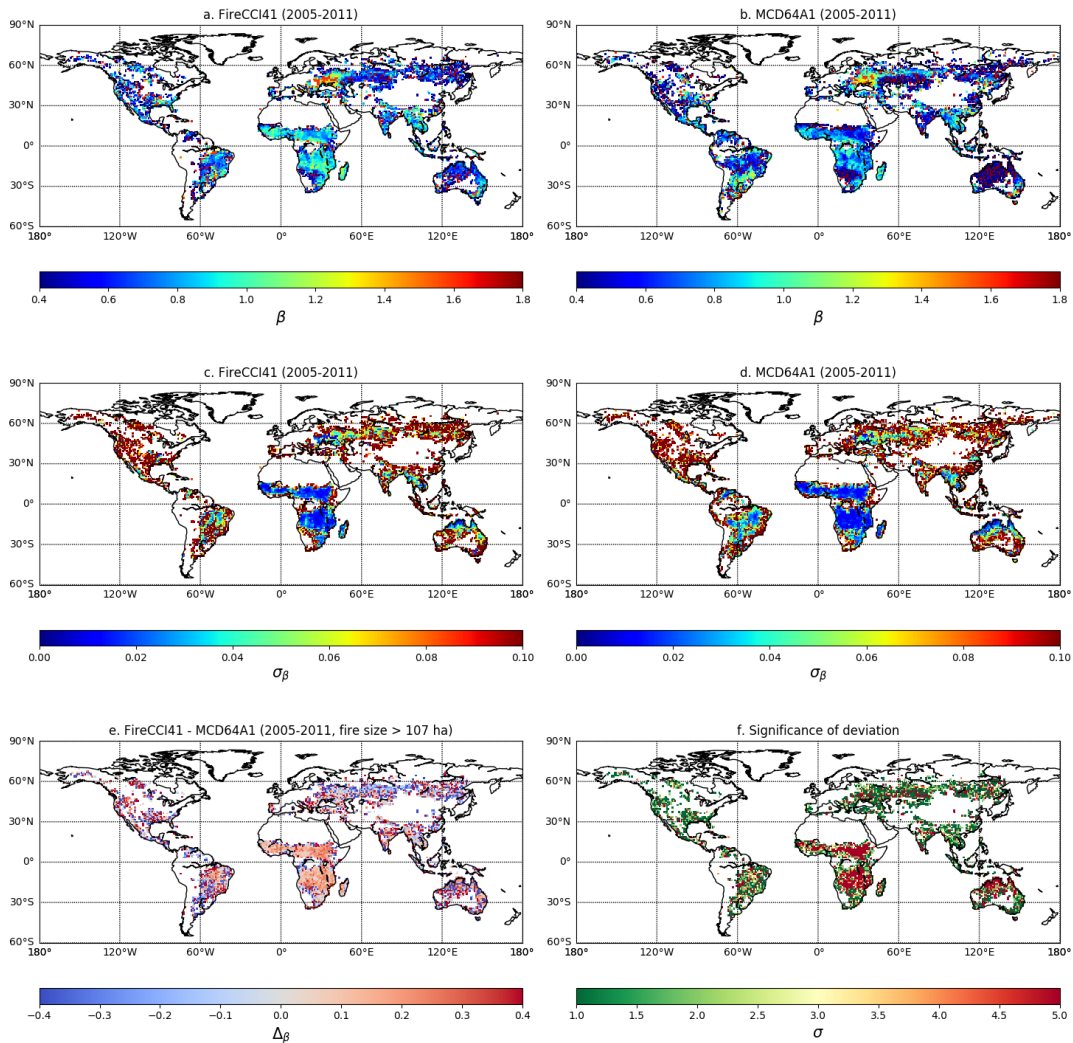
The tendency is inverted for croplands in central Eurasia and India for MCD45A1 collection 5, where the MODIS product presents a steeper power law than the FireCCI41 product. However, when FireCCI41 is compared to MCD64A1 collection 6 (Figure 45), the difference is reversed in India, and its amplitude is reduced in Central Eurasia. This effect is surprising because FireCCI41 is expected to detect more small

fires. However, most of the fire in central Eurasia originates from agricultural activities: such crop fires are small, controlled fires with a short duration time, and could therefore be easily missed by the two-steps approach of the Fire\_cci algorithm.

The level of agreement between the FireCCI41 and MCD45A1/MCD64A1 products is generally good, with most cells matching within 2 sigmas, except for Africa where the fitted  $\beta$  do not match even within 5 sigmas. It should be noted that we used Poisson uncertainties for the fit of the power law, which frequently gives an underestimation of uncertainties. This can degrade the diagnosed level of agreement between the two products.



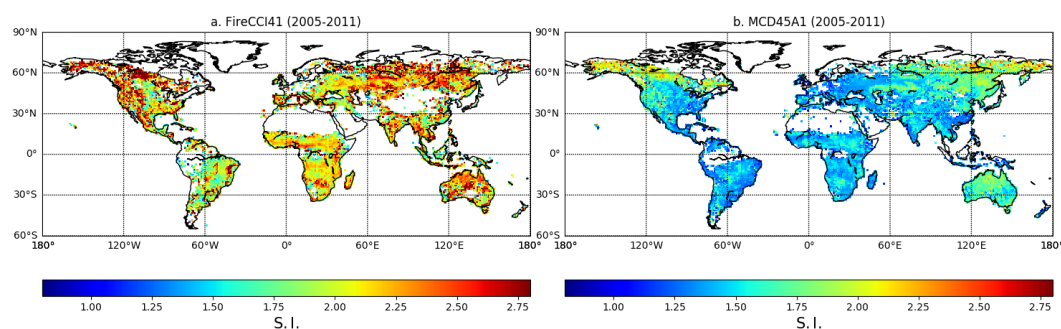
**Figure 44:** Map of  $\beta$  parameter for the FireCCI41 (2005-2011) product (top left) and its uncertainty (middle left), for the MCD45A1 collection 5 product (2000-2016) (top right) and its uncertainty (middle right), the difference between the two products (bottom left) and the level of agreement between the two products (bottom right). The power law is only computed when there are more than 10 detected individual fires in the cell.



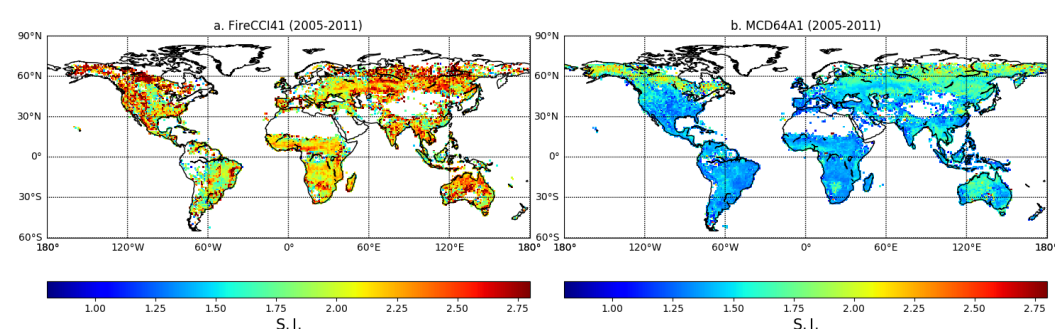
**Figure 45:** Same as **Figure 44**, with MCD64A1 collection 6 instead of MCD45A1 collection 5.

Figure 46 and Figure 47 show the shape index for all products. Fire patches smaller than 107 ha were removed from the FireCCI41 product (which corresponds to the 5-pixel fire size cut applied on the MODIS products) in order to compare the same size category between the two products. As expected, due to its better spatial resolution, and the ‘growing’ phase of the Fire\_cci algorithm, FireCCI41 detects more complex fire patches than any of the MODIS products. Nevertheless, the shape index pattern is very similar between the products, even for small-scale variations (NHAF, SHAF and Australia (AUST)). Fire patches are usually much more complex at high latitude (Boreal Asia (BOAS) and Boreal North America (BONA)). This effect probably arises from a projection effect, since high latitude pixels cover a smaller area than pixels located close to the equator. This results in the same fire patch being made up of more pixels at high latitudes, which can result in an artificially higher shape complexity.





**Figure 46:** Shape Index for the FireCCI41 product (top left), for the MCD45A1 collection 5 product (top right).



**Figure 47:** Same as Figure 47, with MCD64A1 collection 6.

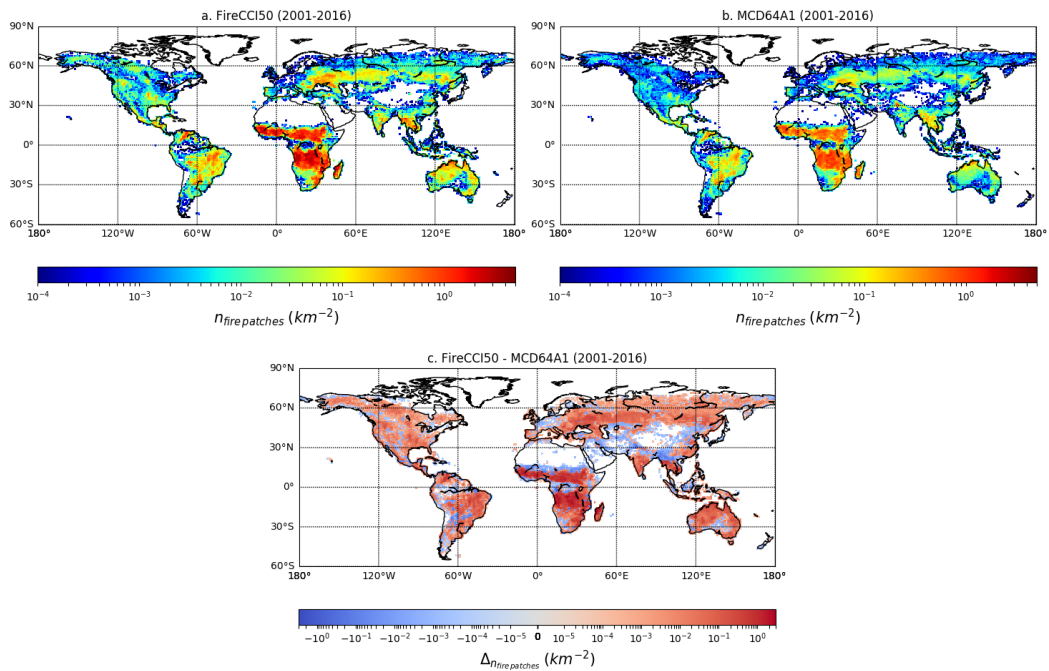
#### 4.2.2. Comparison between FireCCI50, FireCCI51 and MCD64A1

Following the same approach as for the comparison between FireCCI41 and MCD64A1, we compared the FireCCI50 and FireCCI51 fire patch databases with MCD64A1 (between 2001 and 2016). Figure 48 displays the results for the fire patch density, Figure 49 for the Shape Index, and Figure 50 for the fit of the power law. The results are similar than for the comparison with FireCCI41. Due to its better resolution, the FireCCI50 yields more individual fire patches than MCD64A1 in regions with high fire path density. In the areas where FireCCI41 detected significantly less fire patches than MCD64A1 (in some areas of SHAF and SHSA) because of missing data in MERIS imagery, the FireCCI50 also detects more fire patches than MCD64A1. The other areas where MCD64A1 detects more fires are also probably linked to missed burned pixel seeds by the algorithm.

The fitted  $\beta$  parameter is globally higher for FireCCI50 than for MCD64A1, meaning that FireCCI50 detects more small fires than MCD64A1. The tendency is reversed in central Eurasia, where the power is steeper for MCD64A1.

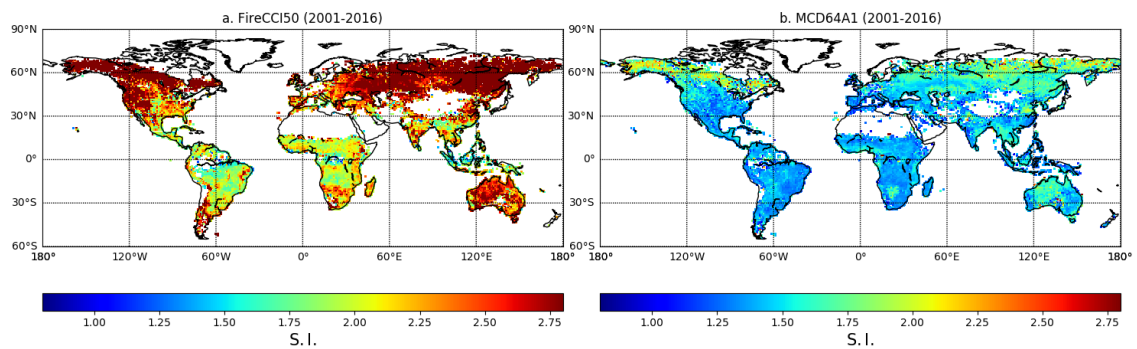
The general agreement is lower between MCD64A1 and FireCCI50 than between MCD64A1 and FireCCI41. This is not surprising, because we expect FireCCI50 to detect even more small fires than FireCCI41, explaining why the agreement of the fire size distribution is lower with MCD64A1.



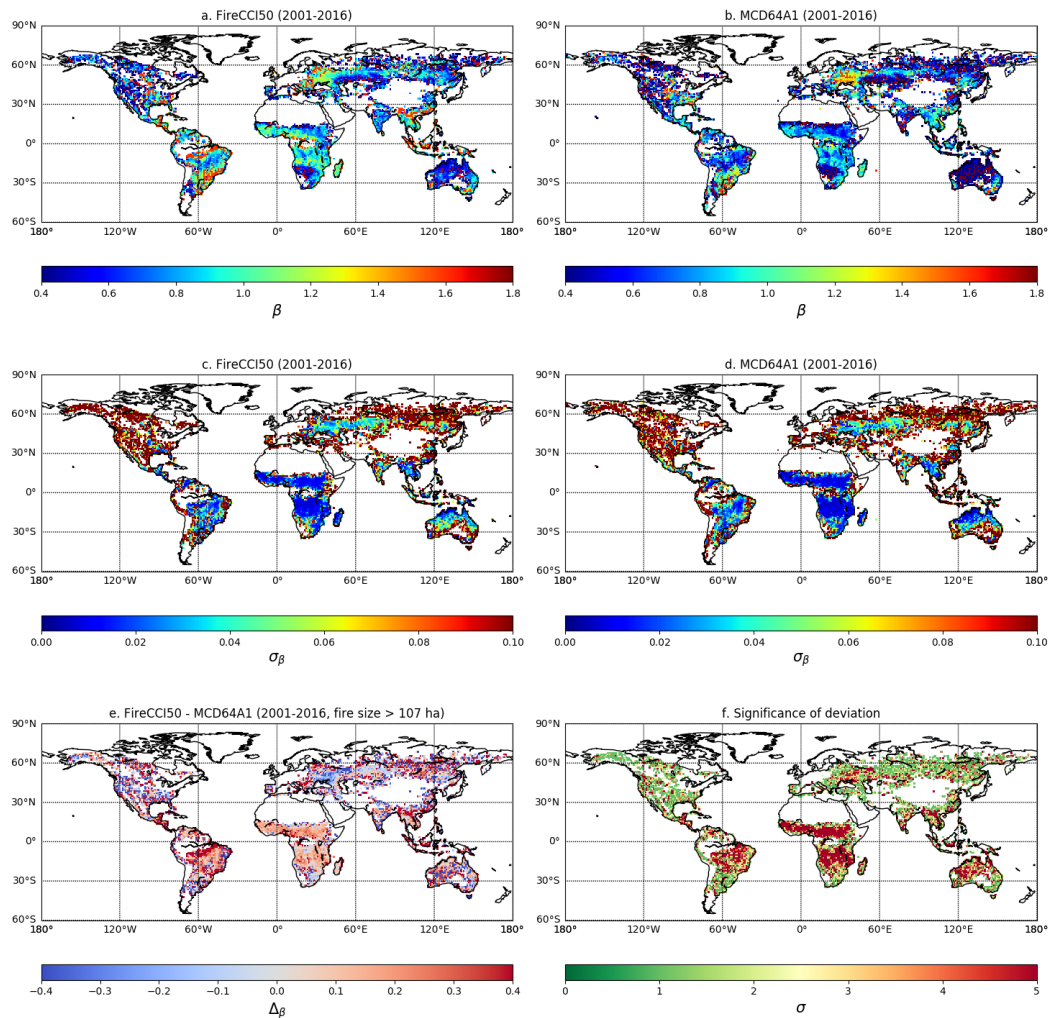


**Figure 48:** Same as **Figure 42** and **Figure 43**, with the FireCCI50 instead of FireCCI41.

Figure 49 shows the Shape Index for FireCCI50 and MCD64A1. As expected, the Shape Index is much higher for the Fire\_cci product, due to the better resolution and the choice of using a two-step algorithm.



**Figure 49:** Same as **Figure 46** and **Figure 47**, with FireCCI50 instead of FireCCI41. The 107 ha cut is applied.



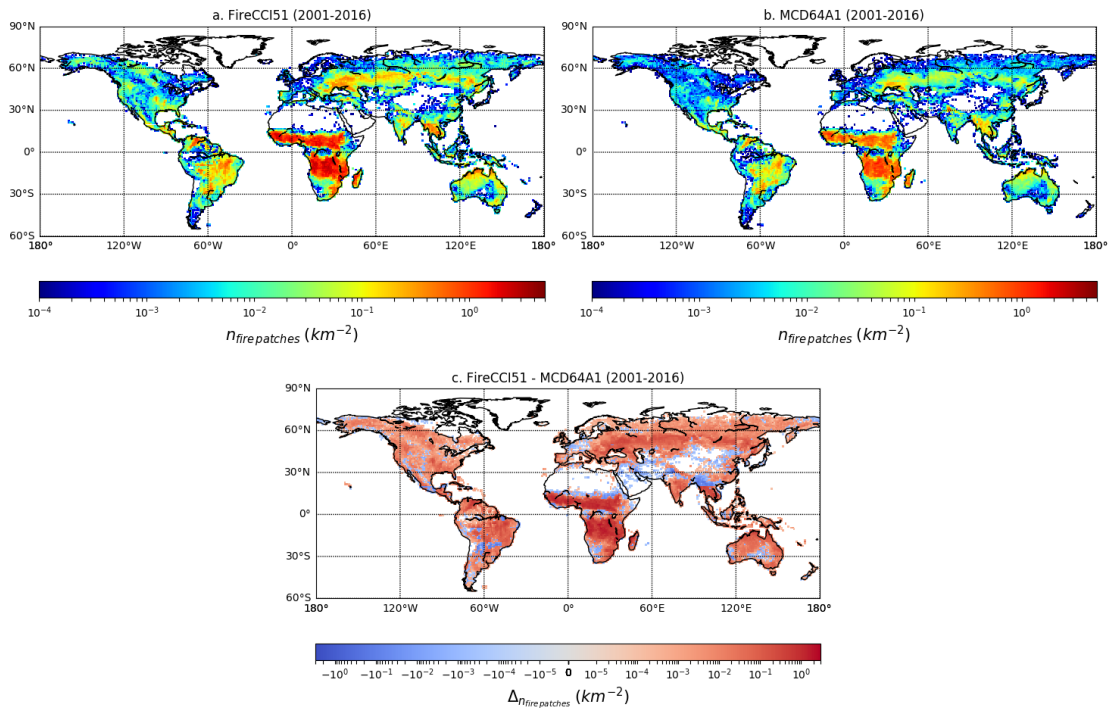
**Figure 50:** Same as **Figure 44** and **Figure 45**, with FireCCI50 instead of FireCCI41.

Figure 51 shows the density of fire events for FireCCI51 compared with MCD64A1. As expected, the results are similar than those obtained with FireCCI50, and FireCCI51 usually detects more individual fires than MCD64A1 everywhere on the globe thanks to its finer spatial resolution. As for FireCCI50, there are still some areas (in Central Asia and Sahel) where MCD64A1 detects more fires than FireCCI51, but these areas are much smaller than for FireCCI50.

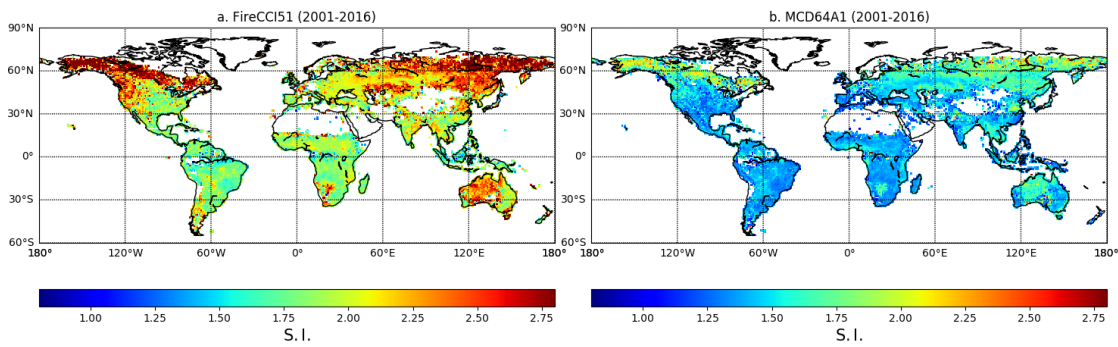
The agreement for the power law maps (Figure 52) is also better between FireCCI51 and MCD64A1 than between FireCCI50 and MCD64A1. The ameliorations are not only restricted to areas of limited agreement (i.e., Africa and South America), but impact the global fire size distribution of fire patches. Combining the results from Figure 51 and Figure 52, we can conclude that FireCCI51 detects more small fire patches than MCD64A1, since for larger fire patches (> 107 ha) the fire patch size distribution are in fair agreement with MCD64A1.

Figure 53 displays the average shape index of FireCCI51 compared with MCD64A1. As for FireCCI50, the higher resolution of FireCCI51 with respect to MCD64A1 yield

higher shape index at global scales (more complex fire patches). However, the values are slightly lower than for FireCCI50.



**Figure 51:** Same as Figure 41 and Figure 42, with FireCCI51 instead of FireCCI41.



**Figure 52:** Same as Figure 45 and Figure 46, with FireCCI51 instead of FireCCI41. The 107 ha cut is applied.

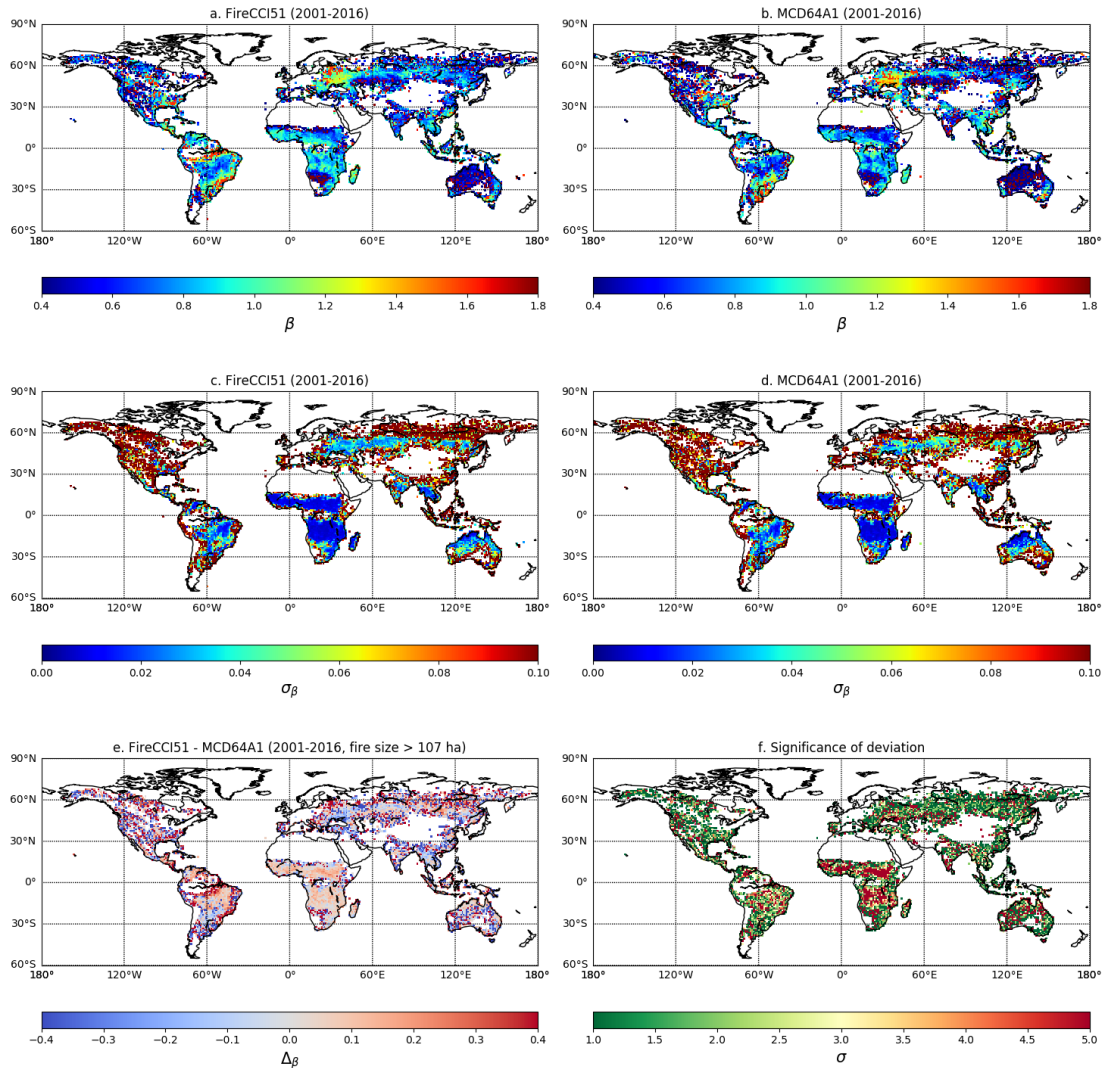


**Figure 53:** Same as Figure 31 and Figure 32, with FireCCI51 instead of FireCCI41.

### 4.3. Influence of the cut-off on fire morphological traits

Figure 54 shows the variation of the  $\beta$  parameter, shape index and ellipse ratio, averaged in each GFED4 region and for all products. For MCD45A1/MCD64A1, only the years 2005-2011 are displayed, and fires smaller than 107 ha are removed from FireCCI41. The results for the 4 cut-off values (3, 5, 9 and 14) are displayed.

A higher threshold yields a smaller  $\beta$ , because the flood-fill algorithm will group together smaller fires as one. This results in a reduction of the number of small fires and an augmentation of the number of big fires, therefore a less steep power law. The variation between different cut-off values is higher than the variation between FireCCI41 and MCD64A1 collection 6. This suggests that the reconstructed fire patch size is compatible between FireCCI41 and MCD45A1/MCD64A1, when comparing fires bigger than 107 ha.

The cut-off value has a limited influence on the complexity of the reconstructed patches. For the Shape Index, the difference between FireCCI41 and the 2 MODIS products is much higher than the variation between different cut-off values for the same product.





However, up to a normalization factor, the averaged values of Shape Index are compatible between all products, with higher values in BONA and BOAS (as discussed in Section 4.2), lower values in Equatorial Asia (EQAS), and constant values for the other GFED4 regions. For the Ellipse Ratio, the behaviour is quite similar to the Shape Index. Higher cut-off yields more elongated patches, and the Ellipse Ratio for the FireCCI41 product is globally higher than for the MODIS products.

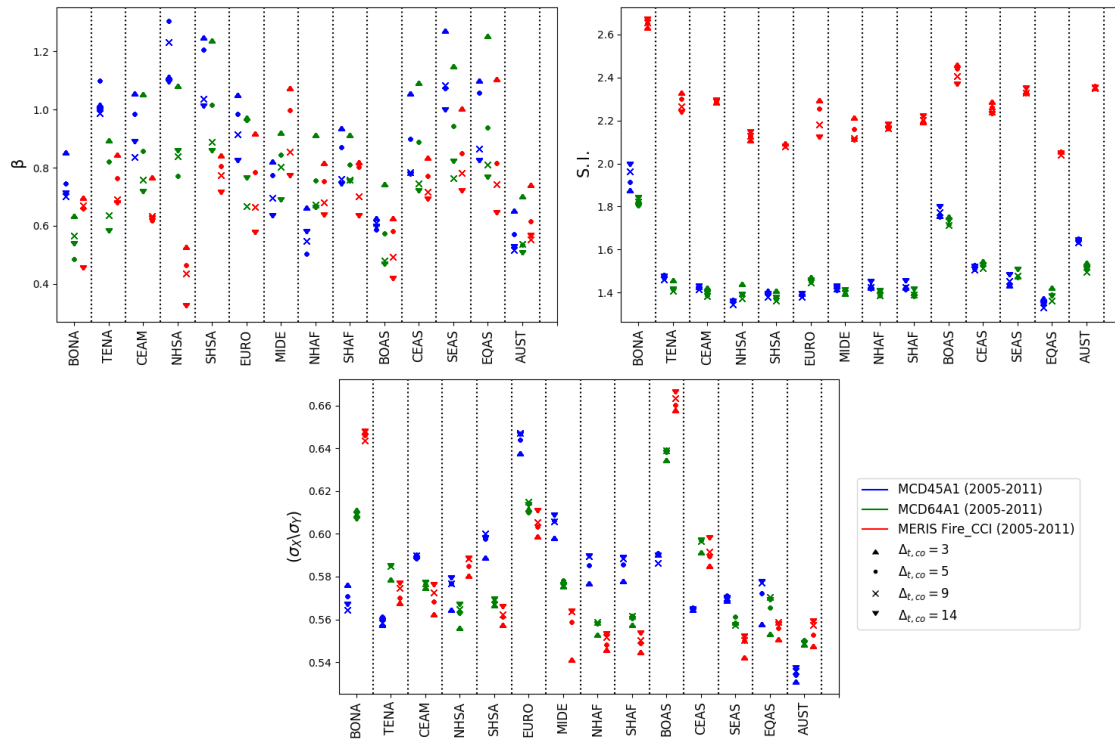


**Figure 54:** Averaged values of the  $\beta$  parameter (top left), Shape Index (top right) and Ellipse Ratio (bottom) for MCD45A1 collection 5 (blue), MCD64A1 collection 6 (green) and FireCCI41 (red). The results for 4 cut-off values are displayed.

#### 4.4. Fire patch morphological traits with the FireCCISFD10 BA product

Figure 55 to Figure 58 display the resulting  $0.25^\circ \times 0.25^\circ$  grid maps for the Small Fire Dataset (SFD) Fire\_cci v1.0 (FireCCISFD10) BA product for Northern Hemisphere Africa, from January to September 2016. The very high resolution of the Sentinel-2 sensors ( $20 \times 20$  m at nadir) allows the detection of very small fires that cannot be detected by MERIS or MODIS. As a result, the maps of fire morphological maps exhibit very clear structures, even on such a short time span.

Fire density (Figure 55) is higher in the tropical savannas of NHAF, and gradually diminishes toward the Sahelian region. Countries exposed to the higher number of fire events during the considered time period were Guinea, Sierra Leone, Benin, Togo, Central African Republic, South Sudan and Uganda. The beta parameter of the power law is also higher in savannas, and lower in the Sahel, but its small scale structure is slightly different from the fire density. The regions with higher beta parameter (Figure 56) follow closely the distribution of agricultural fires from Magi et al. 2012. The higher values for the beta parameter are reached in Cameroon, Togo and Benin, where Magi et al. have shown that more than 80% of the fires come from agricultural activities. Since agricultural fires are smaller than natural fires, this can result in a steeper power law in these regions.





fire  
cci

Fire\_cci  
Climate Assessment Report

Ref.:	Fire_cci_D5.1_CAR_v1.4		
Issue	1.4	Date	16/11/2018
		Page	53

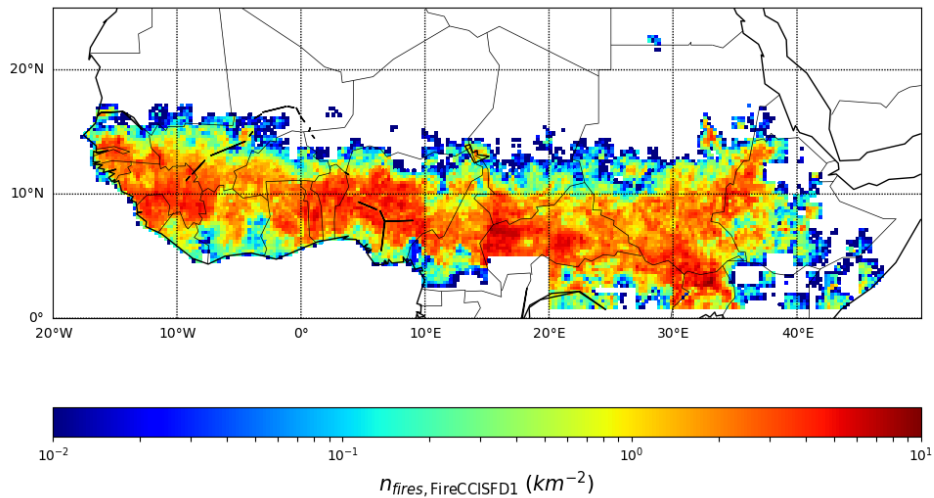


Figure 55: Fire density ( $\text{km}^{-2}$ ) for the FireCCISFD10 BA product (from January to September 2016)

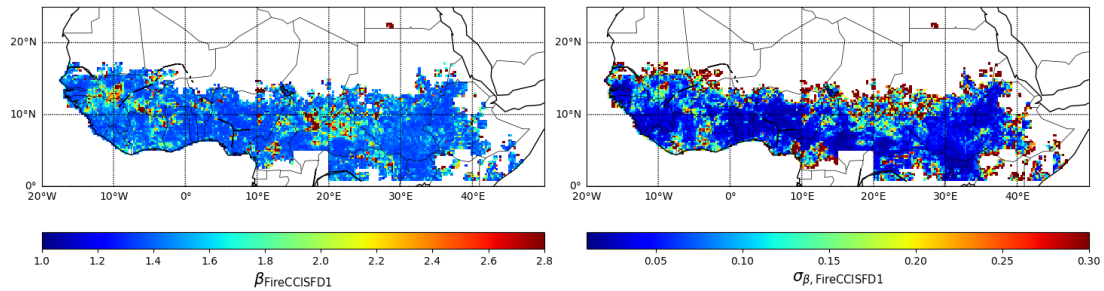


Figure 56: Beta parameter for the FireCCISFD10 BA product (from January to September 2016)

The Shape Index (Figure 57) also displays strong region patterns, with higher values in Cameroon, Central African Republic and South Sudan. It does not appear to be correlated with fire density and beta parameter. However, high values of Shape Index seem to be correlated with lower value of the Ellipse Ratio (Figure 58), which suggests that complex fire patches are more elongated than simpler fire patches.

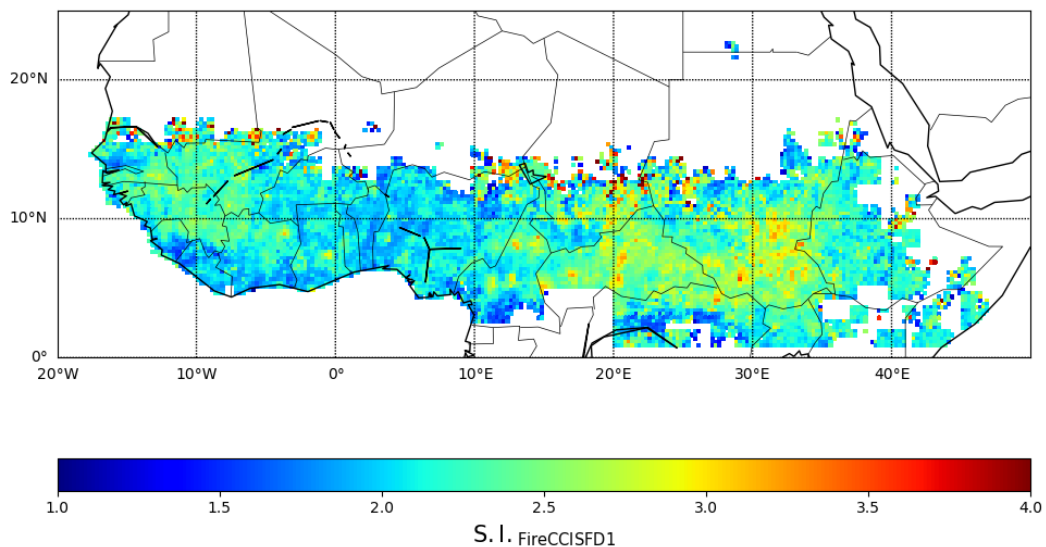


Figure 57: Shape Index for the FireCCISFD10 BA product (from January to September 2016)



fire  
cci

Fire\_cci  
Climate Assessment Report

Ref.:	Fire_cci_D5.1_CAR_v1.4		
Issue	1.4	Date	16/11/2018
		Page	54

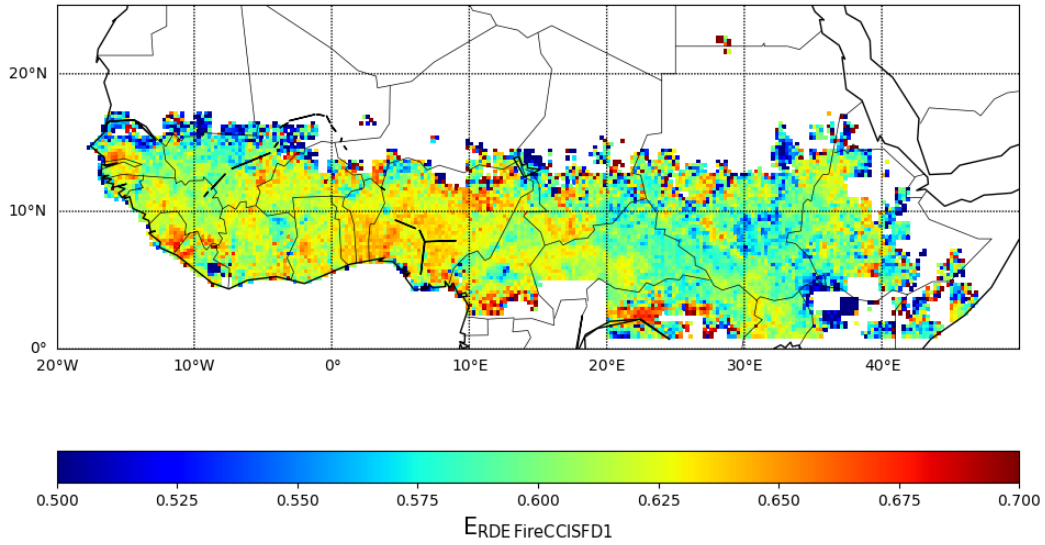


**Figure 58:** Ellipse Ratio for the FireCCISFD10 BA product (from January to September 2016)

Figure 59 to Figure 62 shows the maps for the FireCCISFD10 and MCD64A1 products during their overlapping time series. As expected, the density of fire patches is much higher for the FireCCISFD10 product (Figure 59), in all cells. The  $\beta$  parameter of the power law is also steeper in these areas, meaning that the FireCCISFD10 product performs better than MCD64A1 at detecting small fire patches. This explains why the level of agreement of  $\beta$  between the two products is limited.

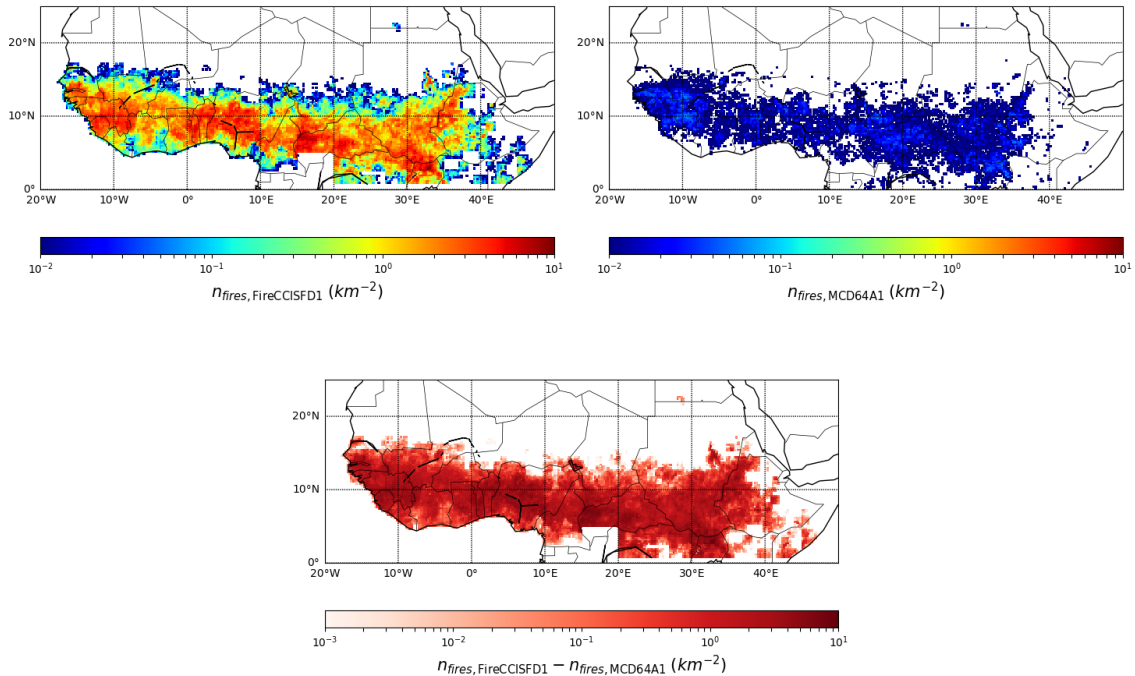


**Figure 59:** Fire density ( $km^{-2}$ ) for the FireCCISFD10 product (top left), MCD64A1 collection 6 (top right). The difference between the two products is displayed during the time span covered by the FireCCISFD10 product. For the sake of product inter-comparison, only fires bigger than 107 ha are displayed.

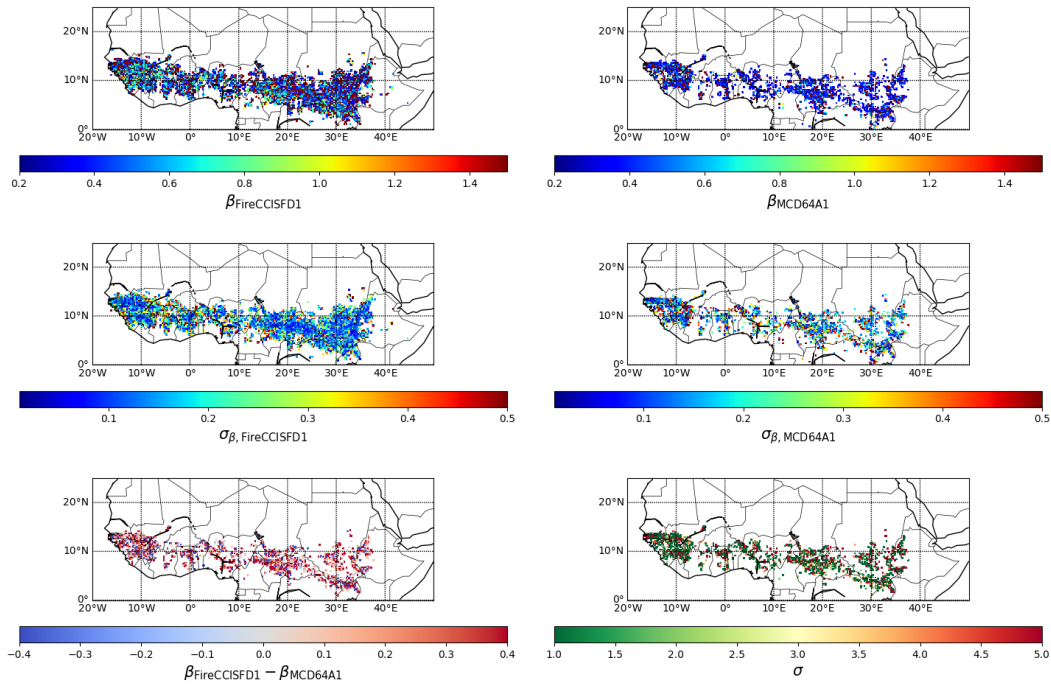


**Figure 60:** Map of  $\beta$  parameter for the FireCCISFD10 product (top left) and its uncertainty (middle left), for the MCD64A1 collection 6 product (top right) and its uncertainty (middle right). The difference between the two products (bottom left) and the level of agreement between the two products (bottom right) are also displayed. The power law is only computed when there are more than 10 detected individual fires in the cell.

Averaged values of Shape Index are much higher for the FireCCISFD10 product than for the MCD64A1 product, because its high resolution allows detecting accurate fire patch perimeter. However, the variations of Shape Index within each survey do not follow the same pattern. For example, FireCCISFD10 clearly detects more complex fire shapes in Sudan than MCD64A1.

On the other hand, Figure 62 shows that the averaged Ellipse Ratio is similar between the two products: all cells are in agreement within 1 sigma for fire bigger than 107 ha. The absence of clear geographical pattern of Ellipse Ratio in the FireCCISFD10 product after removing the fire patches smaller than 107 ha might suggest that only the elongation of small fires is sensitive to climatic or environmental factors.

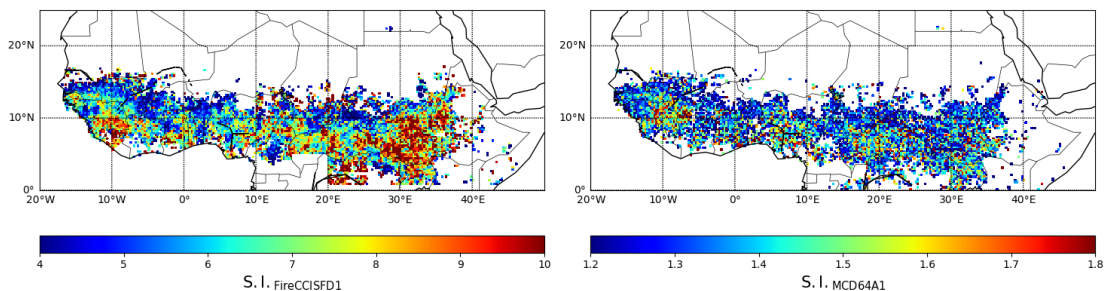


**Figure 61:** Maps of Shape Index for the FireCCISFD10 product (left) and the MCD64A1 Collection 6 product (right). Only fires bigger than 107 ha have been used to compute the maps.

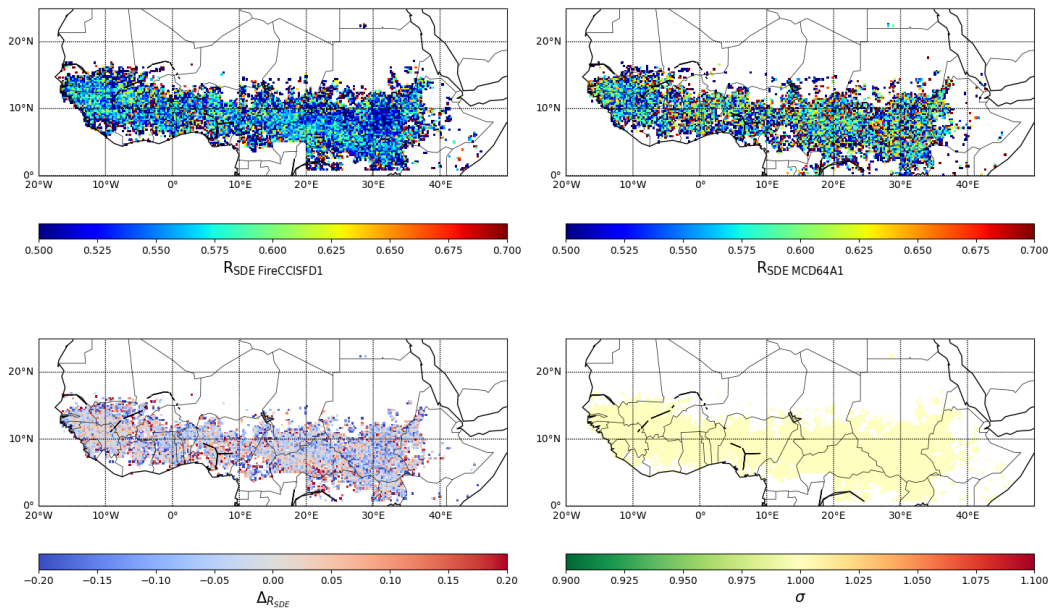


**Figure 62:** Maps of Ellipse Ratio for the FireCCISFD10 product (top left) and the MCD64A1 Collection 6 product (top right). The difference between the two products (bottom left) and the level of agreement (bottom right) are also displayed. Only fires bigger than 107 ha have been used to compute the maps.

## 5. Looking for relationships between different driving factors and fire size

### 5.1. Relationship between fire intensity and fire size

In this section, the relationship between fire intensity (FI) and fire size (FS) was analysed. To retrieve fire intensity information for each derived fire patches, the MCD14ML global product was used (Giglio et al. 2006), which provides the list of geographic coordinates of individual active fire pixels detected by the MODIS sensor on the Terra and Aqua satellites for the period 2000-2017 with a resolution of 1x1km, along with their Fire Radiative Power (FRP). FRP is used here as a proxy of fire intensity (Wooster et al. 2005, 2013). To associate active fire pixels with fire patches, the following procedure was used:

1. for a given fire patch, all active fire pixels that belong to the ellipse fitted over the fire patch were determined, which means that their centres (x, y) follow the equation:

$$\frac{\left((x - x_0)\cos(\theta) + (y - y_0)\sin(\theta)\right)^2}{a^2} + \frac{\left((x - x_0)\cos(\theta) + (y - y_0)\sin(\theta)\right)^2}{b^2} < 1$$

where (x<sub>0</sub>, y<sub>0</sub>) is the centre of the standard deviation ellipse (SDE), θ is the clockwise rotation angle of the semi-minor axis with respect to the north, a is the semi-major half-axis and b is the semi-minor half-axis. Since the side of an active fire pixel is 1km, we also consider that an active fire pixel located at a distance of 1km or less from the area covered by the SDE belong to the fire patch.

2. The detection date of the active fire pixel must lie between the minimum and maximum burn date of the fire patch. To account for possible timelag between the detection of an active fire pixel and of burned area, a 30-days buffer is used.

Once all active fire pixels have been associated with fire patches, the average fire intensity is computed for each fire patch. The matching sometimes fails to associate active fire pixel to any fire patch. The number of mismatch decreases as the cut-off raises. This effect suggests that, for low cut-off value, a real fire event can be split in smaller fire patches by the flood-fill algorithm.

In order to ensure that the results do not depend on the cut-off value, the analysis has been performed for MCD64A1 (Figure 63 and Figure 64) and FireCCI41 (Figure 65 and Figure 66) using the most extreme cut-off values (namely 3 and 14). For FireCCI50 and FireCCI51, we used the fire patch database obtained with a cut-off of 5 days (Figure 67 and Figure 68). The median, 25<sup>th</sup> and 75<sup>th</sup> percentiles of fire size for different fire intensity bins are displayed, and their colour represents the median minimum burn date of the fire patches contained in each fire intensity bins.

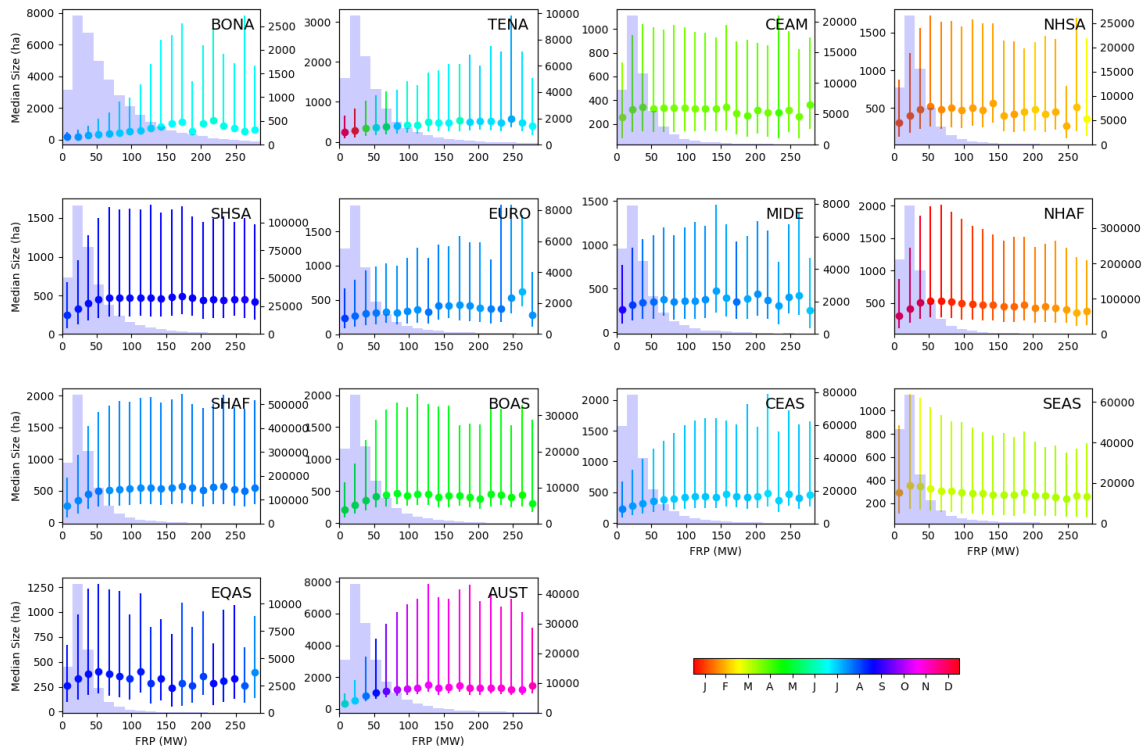


**Figure 63:** Median fire size (from MCD64A1,  $co=14$  days) vs fire intensity from the MCDML14 datasets. The error bars show the 25<sup>th</sup> and 75<sup>th</sup> percentiles of fire size. The colour of the dots and error bars represent the median burn date of fire patches in each bins. The background bars (associated with the right scale on the plots) represent the histograms of the number of fire patches in each FRP bins.





fire  
cci

# Fire\_cci Climate Assessment Report

Ref.: Fire\_cci\_D5.1\_CAR\_v1.4

Issue 1.4 Date 16/11/2018

Page 58

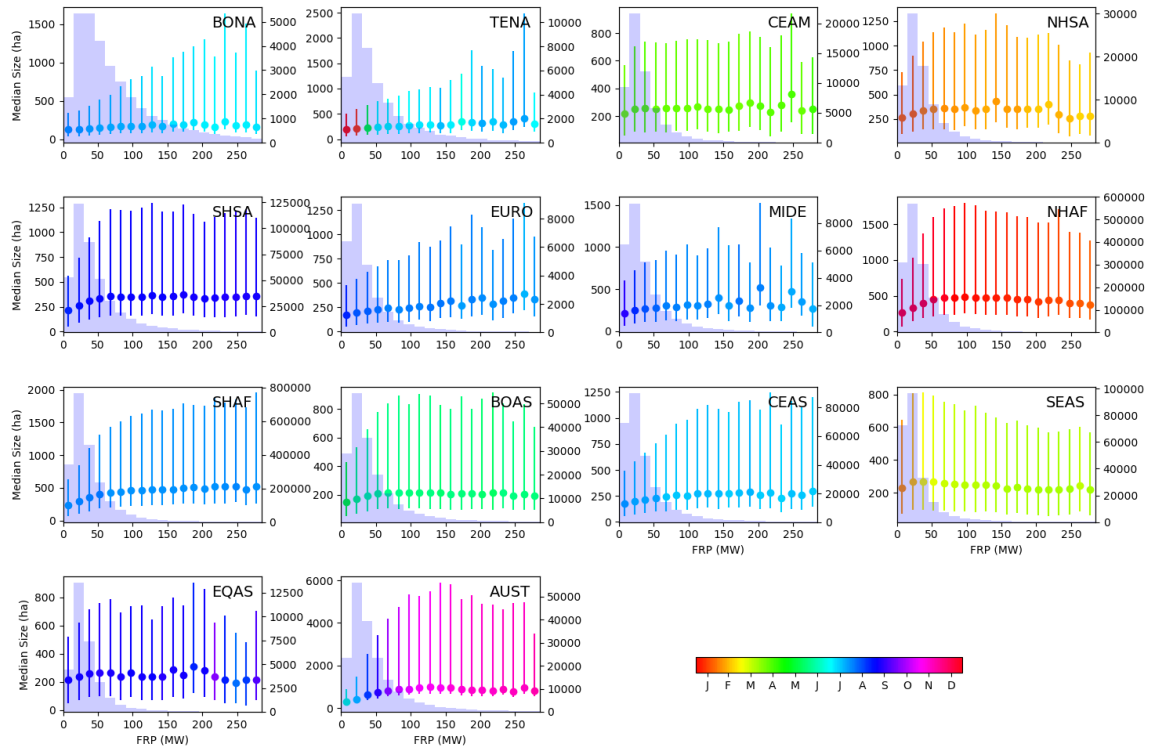


Figure 64: Same as Figure 63, with  $co=3$  days.

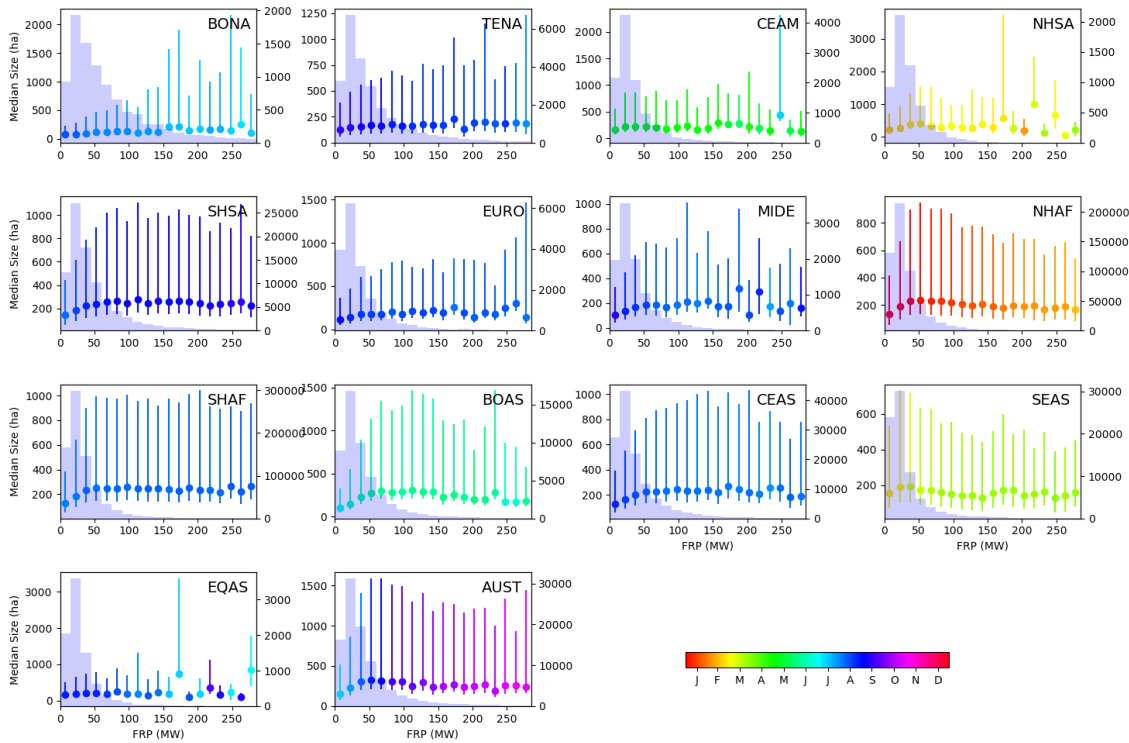


Figure 65: Same as Figure 63, with FireCCI41 (2005-2011).



fire  
cci

# Fire\_cci Climate Assessment Report

Ref.: Fire\_cci\_D5.1\_CAR\_v1.4

Issue 1.4 Date 16/11/2018

Page 59

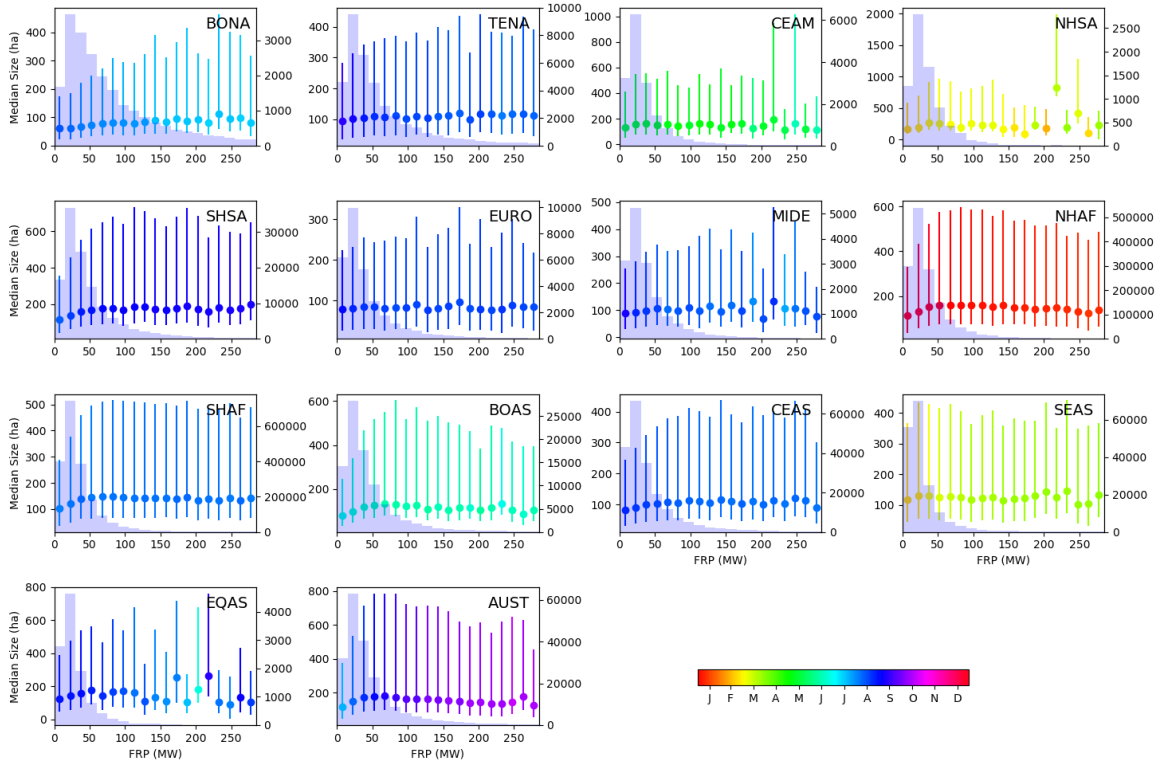


Figure 66: Same as Figure 63, with FireCCI41 (2005-2011) and co=3 days.

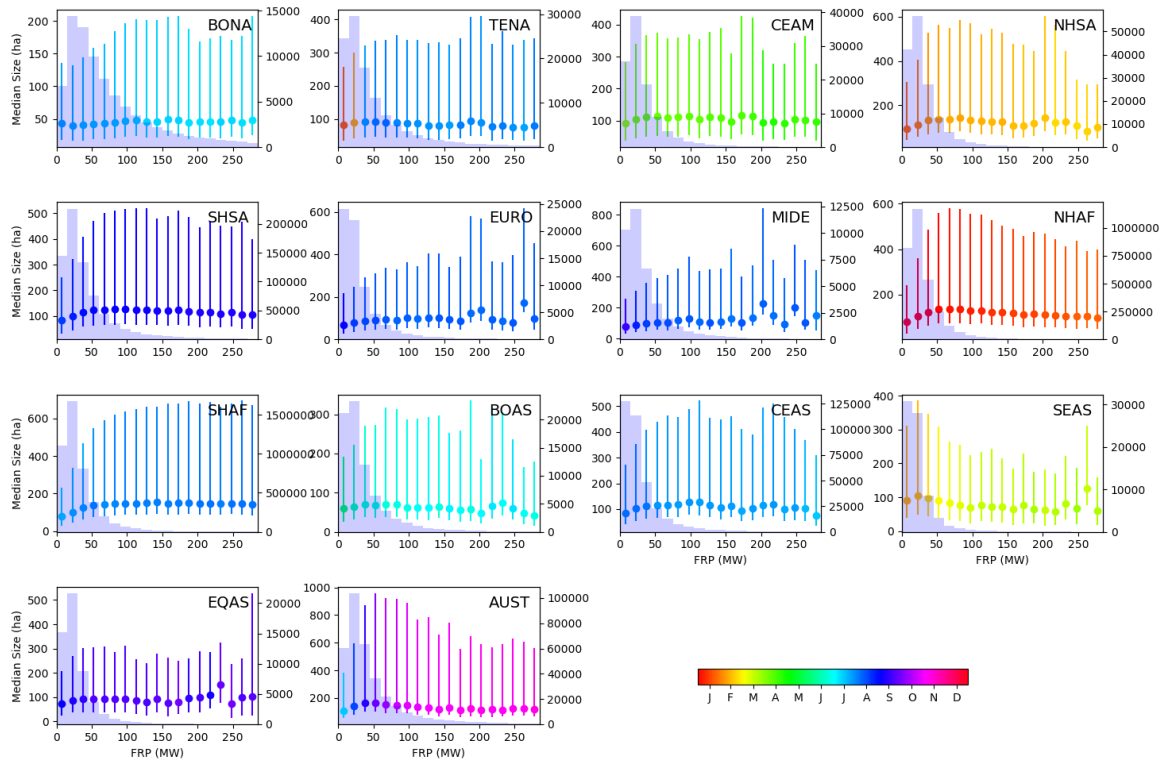


Figure 67: Same as Figure 63, with FireCCI50 and co=5 days.

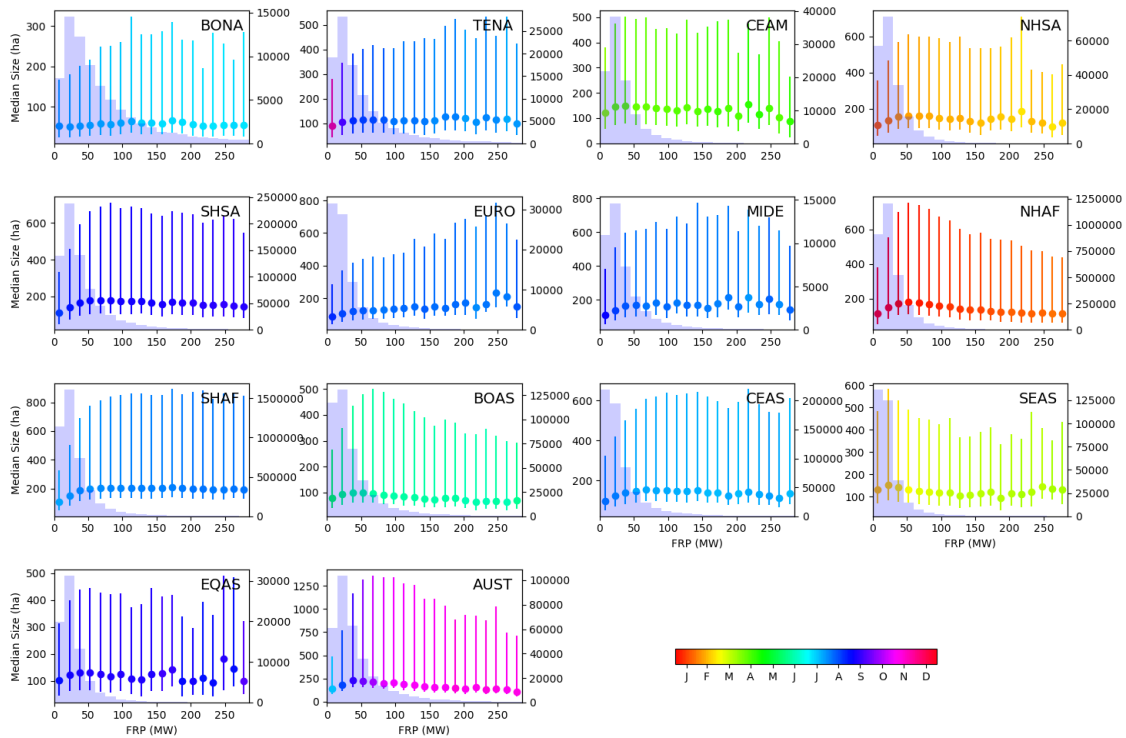
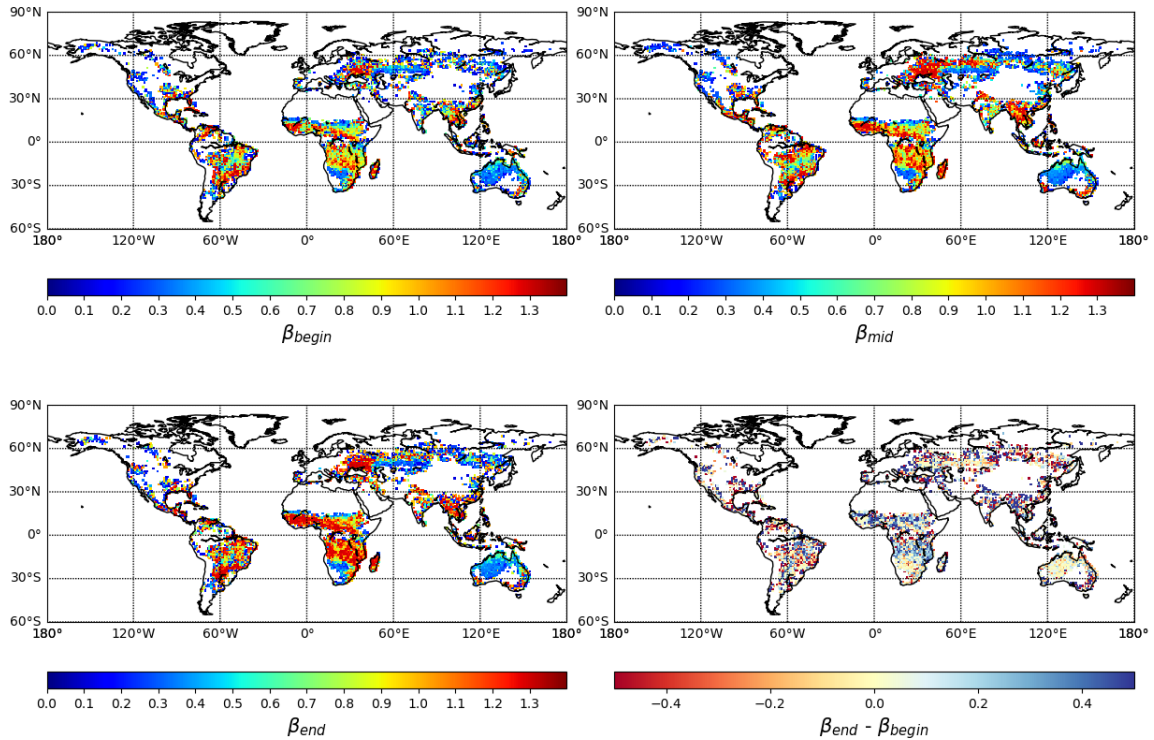


Figure 68: Same as Figure 63, with FireCCI51 and  $co=5$  days.

For MCD64A1 and a cut-off of 14 days (Figure 63), a humped relationship between fire size and fire intensity is observed for the equatorial regions of GFED (CEAM, EQAS and SEAS). At low fire intensity values, the median and quantiles of fire size first increase with fire intensity. A threshold is then reached at low to intermediate fire intensity. Fire patches associated with high fire intensity have a higher median burn date, meaning that they tend to occur later in the fire season. In NHAF, NHSA, SHAF, SHSA, and AUST, the relationship between the median and quantiles of FS vs FI is similar than the one observed for equatorial biomes. However, the maximum fire size is usually reached at higher intensity threshold, and the decrease after the threshold is more gradual. The relationship is similar in BOAS. By contrast, in BONA, TENA, EURO, and CEAS, fire size constantly increases with intensity and only reaches a maximum value at very high intensity. The results are similar with FireCCI41, FireCCI50, and FireCCI51, except for AUST, where the fire intensity is reached earlier than for MCD64A1. In addition, for FireCCI50 and FireCCI51, the slope between fire size and fire intensity for BONA and TENA is smaller than for MCD64A1 and FireCCI41.

The evolution of the  $\beta$  parameter along the fire season is shown in Figures Figure 69 to Figure 72. In each 1x1 degree cell, the fire season has been split in 3 temporal periods: the early fire season (the 4 months before the month with highest fire activity), the middle fire season (corresponding to the month with the highest fire activity) and the late fire season (the 4 months after the month with the highest fire activity). For each period and in each cell, the corresponding  $\beta$  parameter (namely  $\beta_{begin}$ ,  $\beta_{middle}$  and  $\beta_{end}$ ) have been computed, and are displayed for MCD64A1, FireCCI41 and FireCCI51. For both products, the  $\beta$  parameter increases at the end of the fire season, meaning that a highest proportion of small fires happened at the end of the fire season. These results are

in agreement with the change of median burn date from Figure 63 to Figure 68, which also show that fire size is significantly smaller in the late season in SEAS and NHAf.



**Figure 69:** Values of  $\beta_{begin}$ ,  $\beta_{middle}$  and  $\beta_{end}$  for MCD64A1 (co=14 days), and differences between  $\beta_{begin}$  and  $\beta_{end}$ .

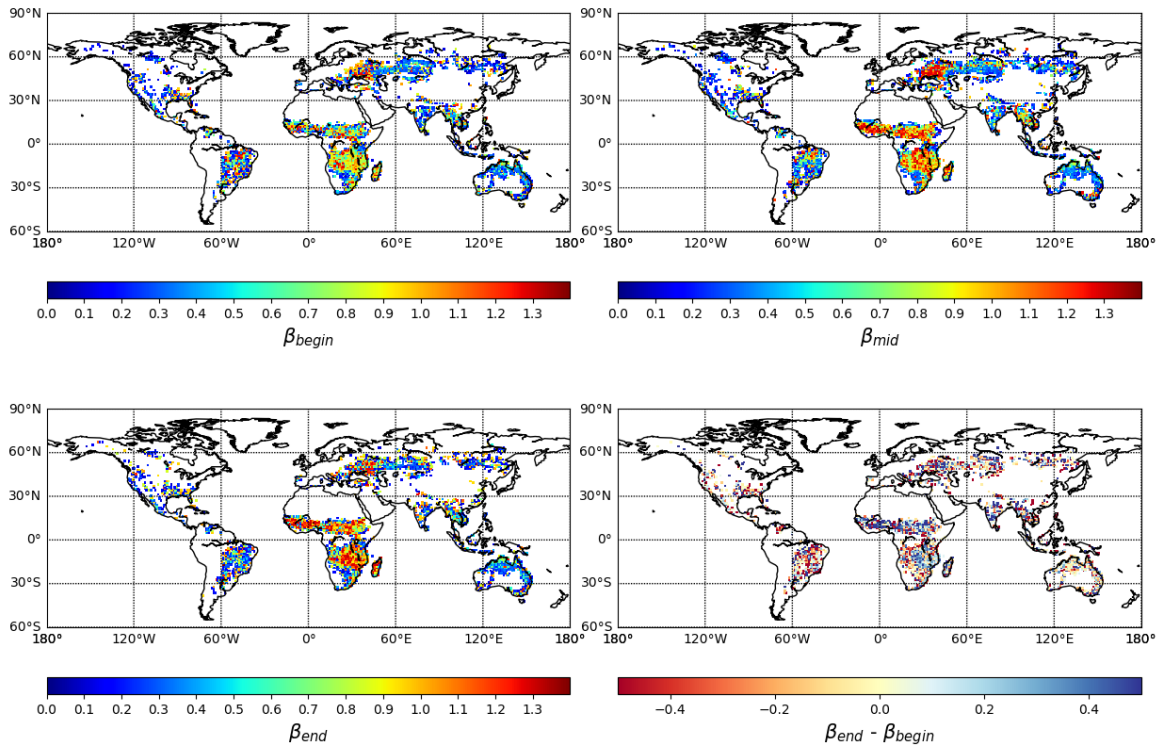


**Figure 70:** Values of  $\beta_{begin}$ ,  $\beta_{middle}$  and  $\beta_{end}$  for FireCCI41 (co=14 days), and differences between  $\beta_{begin}$  and  $\beta_{end}$ .



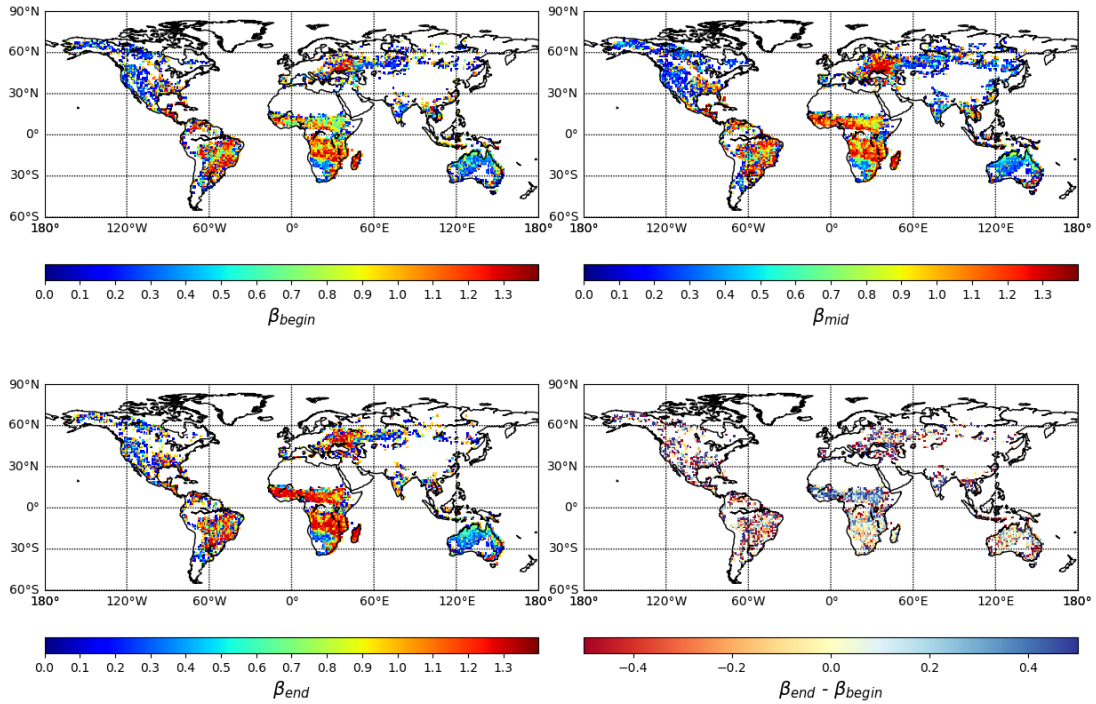


Figure 71: Values of  $\beta_{begin}$ ,  $\beta_{middle}$  and  $\beta_{end}$  for FireCCI150 (co=5 days), and differences between  $\beta_{begin}$  and  $\beta_{end}$ .

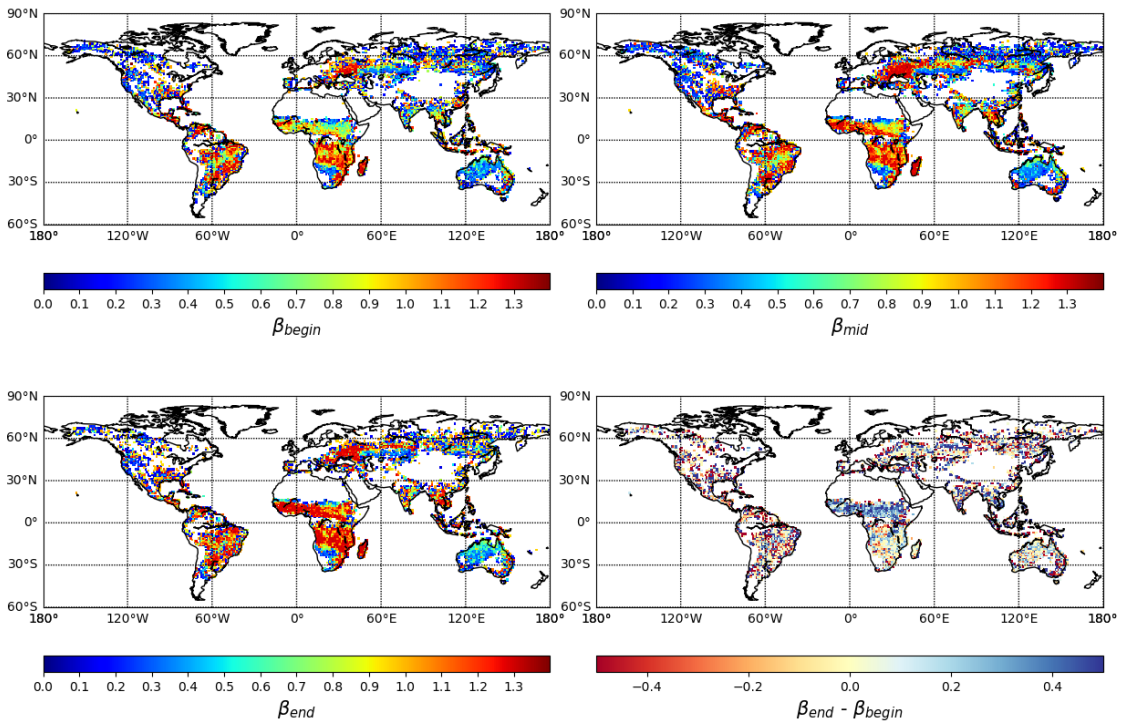


Figure 72: Values of  $\beta_{begin}$ ,  $\beta_{middle}$  and  $\beta_{end}$  for FireCCI151 (co=5 days), and differences between  $\beta_{begin}$  and  $\beta_{end}$ .

Rothermel's equation is used to model fire rate of spread in most process-based DGVMs (Rothermel 1972, Thonicke et al. 2010, Yue et al. 2014). In this model, the rate of spread scales with wind velocity, landscape slope, and fire intensity. It has been tested on experimental and localized fires, which do not account for the real complexity





of the fuel array. For tropical and equatorial GFED regions, our results clearly show that, toward the end of the fire season, fire size reach a limit as fire intensity continue to increase, probably because the fuel becomes dryer (Sedano and Randerson 2014). This suggests that larger fires hit some natural or artificial barriers (roads, fragmentation of landscape due to agriculture).

## 5.2. Influence of wind speed and wind orientation on fire patch geometry and orientation

CRUNCEP reanalysis data was used (<https://rda.ucar.edu/datasets/ds314.3/>, accessed September 2018) which provides in a  $0.25^\circ \times 0.25^\circ$  grid the U and V-wind speed components every 6 hours. We computed at each fire patch position the mean wind speed  $\bar{v}_{wind}$  between the minimum and maximum burned date of the patch. Figure 73 shows the evolution of fire size with  $\bar{v}_{wind}$ . For all continents, we clearly see a decrease of fire size with wind speed when higher wind speeds are reached: this result is in agreement with the findings of Lasslop et al. (2015). It is important to investigate this effect further since it is not accounted for in fire propagation models, and could yield an overestimation of burned area.

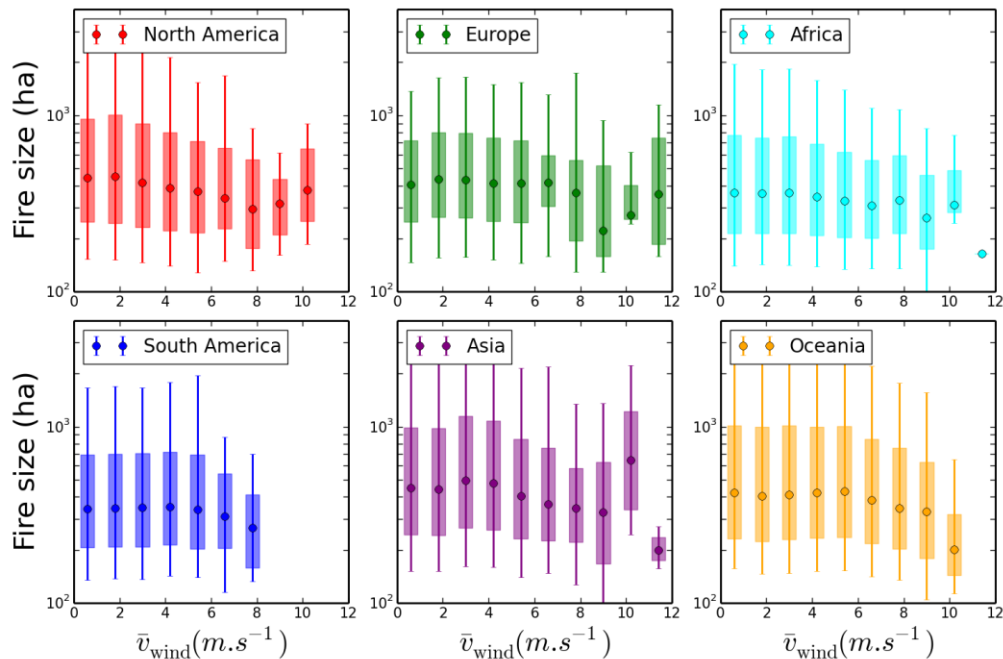


**Figure 73:** Fire size (derived from the fitted ellipse) versus mean wind speed (in  $m.s^{-1}$ ) from the minimum BD to the maximum BD.

In order to study if the patch orientation follows wind orientation, the mean angle of the wind orientation within the burned date span was also computed, weighted by the value of the wind speed. This allows recovering a main wind direction for each fire patch. The correlation coefficient  $r$  was measured from linear regression between wind direction and the orientation of the ellipse  $\theta$ , in a  $1^\circ \times 1^\circ$  grid. In order to limit the loss of signal due to the uncertainty on patch orientation, this study was limited to patches of intermediate size (bigger than 500ha and smaller than 2000ha), since bigger fire are less likely to exhibit a unique fire propagation orientation, and since the uncertainty on smaller fires can be large because of omission and commission errors. The resulting map, displayed on Figure 74, shows no positive correlation between  $\theta$  and wind orientation. However, it has to be kept in mind that NCEP wind data accuracy is very



limited, and that can explain why the analysis failed to find a clear correlation with fire patch orientation.

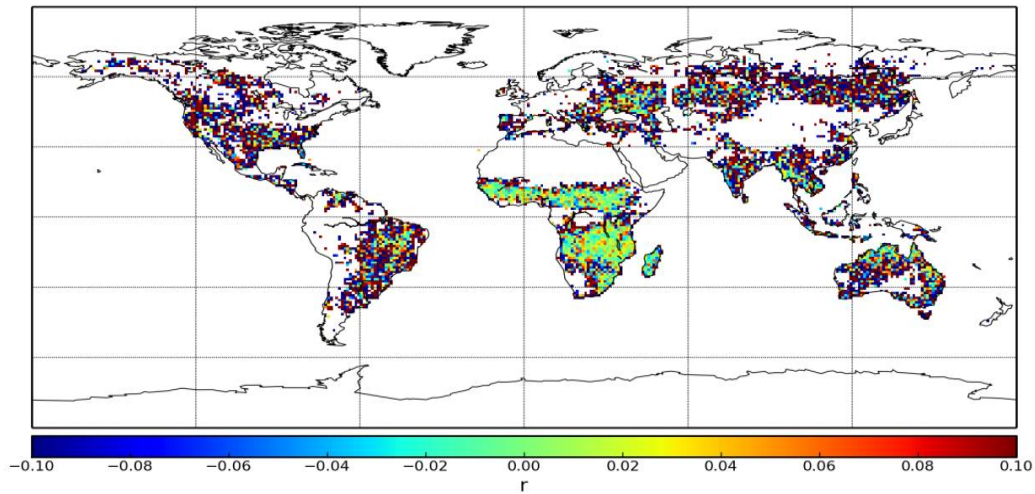


Figure 74: Correlation factor  $r$  between wind orientation and ellipse orientation.

### 5.3. Burned Pixel-derived fire patch morphology as an indicator of spreading process and their environmental drivers

We finally tested the benefit of pixel-level burned area data generated by global remote sensing to derive fire patch morphology, and how the morphological features of fire patches could be the witness of differential spreading processes across biomes, a key information for the improvement of fire modules in DGVMs. We focused our analysis in savannas, the most fire-prone biome worldwide, to determine if regional climate or other environmental variables were leading to specific fire patch morphology.

We based this research on the previously FRY database (Laurent *et al.*, 2018) of global fire patch morphology, derived from the pixel-level burned area data FireCCI41. Describing the morphology of fire patches relies on the landscape indices used for landscape description, and widely described in the FRAGSTATs Software (McGarigal and Marks, 1995). For each single fire patch, FRY database measured fourteen morphology features classified in 6 categories: Size, Complexity, Orientation, Elongation, Propagation and Fire Intensity (Table 2). We selected fire patches located in tropical savannas and grasslands between 25°N and 25°S latitudes in Africa, Australia and South America. We excluded fires smaller than 300 ha to increase the robustness of the complexity features based on early results of Nogueira *et al.* (2016) in tropical South America. In total, we included 2.194.825 fire patches in the analyses.

The location of fire patches was referenced according to three sources of information: the GFED regions from the Global Fire Emissions Database (Giglio *et al.*, 2010), the pyrome regions (Archibald *et al.*, 2013) and the Global Anthromes classification (Ellis *et al.*, 2010). We completed the dataset by including the information on land cover according with MODIS Land Cover Global product (MCD12C1) for 2012 (Friedl *et al.*, 2010). We included five categories from the IGBP classification: woody savannas (class 8), savannas (class 9), grasslands (class 10), cropland (class 12) and mosaic of cropland and natural vegetation (class 14). We also included the percentage of tree cover based on the product MOD44B from MODIS (DiMiceli *et al.*, 2011). Finally, we added the

information of the yearly mean wind speed and direction from the CRUNCEP dataset (Viovy, 2018) providing daily north-south (v) and east-west (w) wind components.

**Table 2:** Description of the morphology of fire patches features (updated from Nogueira et al. 2016)

Feature category	Feature	Definition	Units
<b>Size</b>	Area (A)	Surface area of the patch	ha.km <sup>-2</sup>
	Core area (C)	Surface of area of the internal part of a patch delimited by a boundary located 500m inside its actual boundary	
	Perimeter (P)	Length of the perimeter of the patch	M
<b>Complexity</b>	Perimeter-Area ratio	$\frac{P}{A}$	
	Shape Index (SI)	$SI = \frac{P}{A^{0.5}}$	
	Fractal Dimension Index (FD)	$FD = \frac{2 \ln(P)}{\ln(A)}$	
	APE ratio (APE)	$APE = \frac{Area\ Ellipse}{Area}$	
<b>Orientation</b>	Theta angle	Sinus of azimuthal angle of the longest axis of the fitted ellipse	degree
<b>Elongation</b>	Ellipse ratio	Degree of divergence between a perfect circle and an elliptical shape	1 = Circle, 0 = Ellipse
	Eccentricity	Degree of divergence between a perfect circle and an elliptical shape	1 = Ellipse, 0 = Circle
<b>Propagation</b>	ROSL	Rate of spread linear along the longest ellipse axis	Linear m.day-1
	ROSa	Rate of spread based on daily area burned	ha.day-1
<b>Fire Intensity</b>	FRP	Satellite derived fire radiative power	

We first evaluated the differences in the mean values of the five selected fire patch morphological features for the different GFED regions (Australia, North Hemisphere Africa, South Hemisphere Africa, North Hemisphere South America and South Hemisphere South America) and land cover type (box plot of Figure 73). To get this information, we built a global 2° x 2° grid and we assigned every fire patch to a grid cell (site = 731 grid cells). We calculated the median value for each selected fire patch morphological feature in each grid cell. To explain the spatial variation in the fire patch morphology patterns on global savannas and grasslands, we averaged the quantitative environmental variables for each grid cell (Tree cover, Mean Annual Rainfall, Wind speed) and we calculated the proportion of each category of the quantitative environmental variables (Land Cover and Wind direction) for each grid cell. Wind direction was classified in 4 categories according to its deviation angle from the North: 0 (North-South), 0 - 45 (Northeast – Southwest), 45 - 90 (East-West) and 90 - 135 (Northwest – Southeast). We used the general assumption that fire spread follows an ellipse, for which the direction of the longest axis is driven by wind direction or topography, and the elongation (ratio between the longest and shortest axis) is driven by wind speed. This assumption is used in the theoretical fire spread process embedded in



global dynamic vegetation models (Hantson et al. 2016). Patch complexity is assumed to be affected by landscape fragmentation by natural and human causes, thus, areas with a high tree cover or cropland cover should have a higher complexity index values compared with areas where the herbaceous layer is more homogenous and continuous (e.g. Herbaceous savannas and grasslands areas). We expected thus strong response of a) Fractal dimension index to the percentage of tree cover and land cover type; b) ROSL (fire spread) to wind speed and land cover type; and c) theta to the prevailing wind direction. First, we formulated simple linear regression models to test the relationship between the dependent variable to the different predictor variables. We verified the normality and the homoscedasticity of Theta, ROSL and Fractal dimension index by building the quantile-quantile q-q plot and by plotting the residuals against the predicted values. When the assumptions of these models were confirmed, we compared the lineal models to Generalized Additive Models (GAM) and Generalized Additive Mixed Models (GAMM), which could better capture non-linear relations between the modelled. GAM allowed to use nonparametric smoothed functions to explain the response of the response variable to predictors by adding several explanatory variables. Because ROSL did not show a normal distribution and did not attain the assumption of the variance homogeneity, we fixed the variance structure with a Generalized Least Square (GLS) by using the *VarPower* function.

### 5.3.1. Fire patch pattern across continents

We observed a low variation in the *Area* and *Ellipse ratio* when we compared the five GFED regions (Figure 75A, B). In the five GFED regions, fire patch area was smaller on cropland and mosaic of cropland and native vegetation in contrast with savanna, woody savanna and grassland (Figure 75A). We observed a high variation between regions and land cover for *Theta* with a higher Theta angle in Australia and South Hemisphere in Africa, particularly in croplands for Australia and for the five land cover classes in South Hemisphere in Africa in comparison with the North Hemisphere of this continent (Figure 75C). In the North Hemisphere in Africa and South America, *Theta* was lower on grasslands in comparison with savannas and woody savannas, in contrast with the South Hemisphere for both continents where Theta was higher on grasslands (Figure 75C).

For Fractal dimension index we found higher values on woody savanna and croplands for the five regions, indicating a higher complexity of fire patches on these two land cover classes (Figure 75D). In the South Hemisphere in Africa and South America the complexity was similar for savannas and grasslands while this feature was higher for savannas on the North Hemisphere for both continents and for Australia (Figure 75D). Finally, we found the highest variation in the propagation rate with higher values of ROSI on grasslands for the five regions indicating the fastest fire propagation for this vegetation type and the lower values of this feature on the cropland/natural vegetation mosaic indicating the slowest propagation rate (Figure 75E). Comparing the five regions, we observed the fastest propagation rate in Australia and the lowest propagation in both hemispheres in South America, particularly in croplands and cropland/natural vegetation mosaics (Figure 75E).

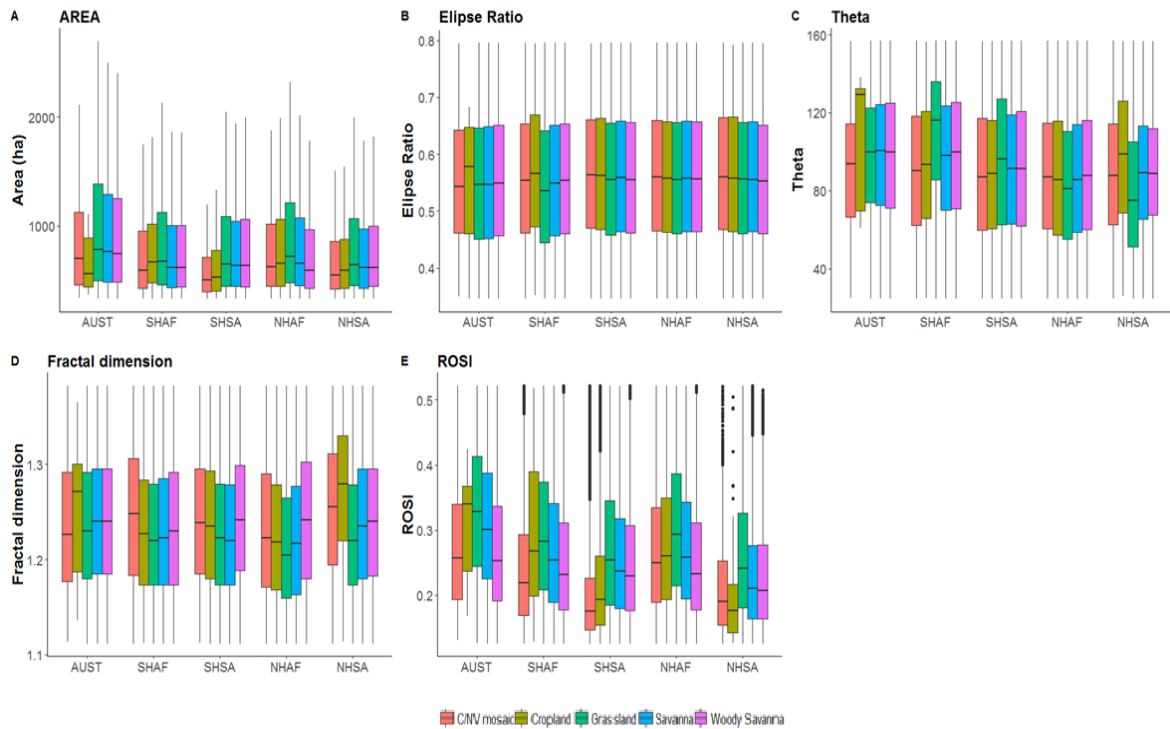


**Figure 75.** Box-and-whisker plots of the distribution of the fire patch morphological features by GFED regions from the Global Fire Emissions Database (Ellis et al., 2010) and by Land cover from MODIS Land Cover Global product (MCD12C1) for 2012 (Friedl et al., 2010).

### 5.3.2. Drivers of fire patch pattern

From the five morphological traits analysed, we observed a variation of Theta angle, ROSL and Fractal dimension index by GFED region and land cover type (Figure 75). When we explored the drivers of these variation, we found that the highest values of theta in Australia and SHAF (Figure 76A) are associated to a Northwest-Southeast prevailing wind direction ( $\sim 135^\circ$ ), while theta mean values near to  $90^\circ$  or slightly lower on SHSA and the Northern regions in Africa and South America were associated to East-West (for SHSA) and Northeast-Southwest (for NHAF and NHSA) prevailing wind direction (Figure 76A and B). In fact, the GAMM including the mean wind direction and the GFED regions explained 37% of the variation of Theta angle, confirming our initial assumptions in which wind direction determine the fire scar orientation, being the best model compared with the lineal model, GLM and GAM (Figure 76C).

For ROSL, we found the highest fire spread rate in Australia associated to the highest wind speed on this continent (Figure 76D and E). Looking at the effect of wind speed on fire spread rate, we found that wind speed explained less than 1% of its variance. However 20% is explained by the differences of wind speed between GFED regions and 25% when we added the effect of land cover type (Figure 76C). This percentage was improved to 58% when we added both factors (land cover and GFED regions) as explanatory variables in a GAMM, and to 70% when we fixed the structure of the variance in a GLS, being our best model to explain the variation of ROSL on savannas and grasslands across continents. Moreover, we observed that ROSL was inversely proportional to ellipse ratio (Figure 77A) indicating that high ROSL values are associated to an elliptical fire shape (low ellipse ratio) while low ROSL values are more associated to circle fire shape.



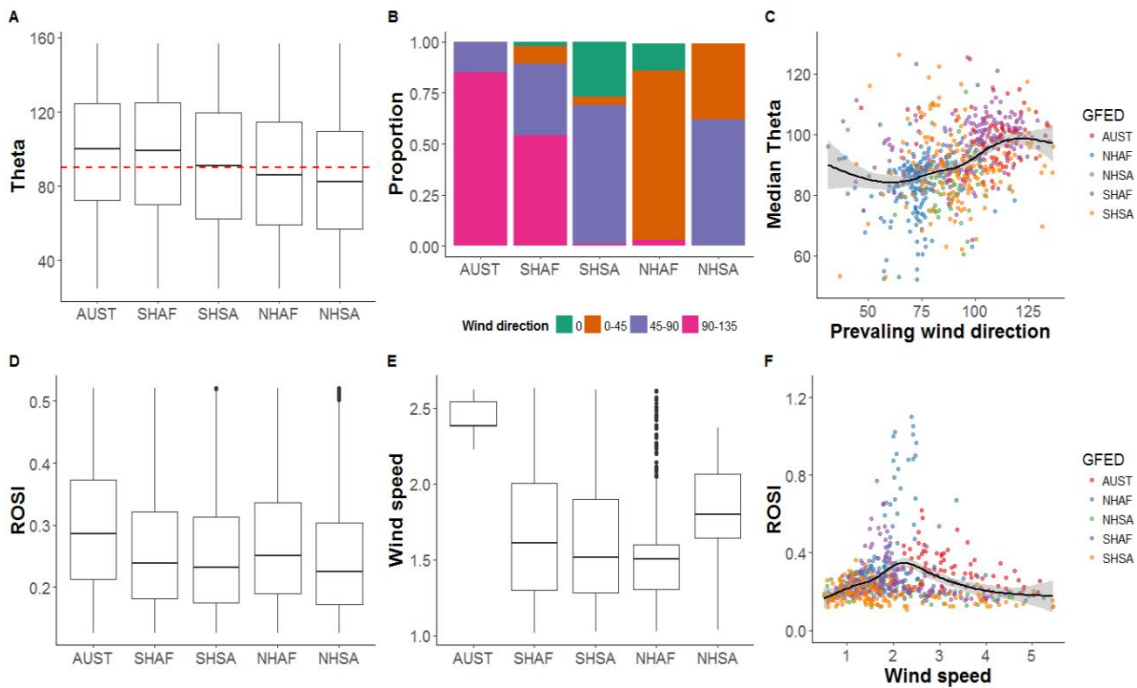


**Figure 76:** A. Box-and-whisker plot of theta angle of fire scars by GFED region. Red line cut the y-axis at 90°. B. Proportion of prevailing wind direction by GFED region. C. Model generalized additive model (GAM) fit of theta angle relationship with the prevailing wind direction across GFED regions. D. Box-and-whisker plot of ROSI (fire spread) by GFED region. E. Box-and-whisker plot of wind speed by GFED region. F. Model generalized additive model (GAM) fit of ROSI relationship with wind speed across GFED regions.

Finally, Fractal dimension index responded to the increase of tree cover and the land cover, which explained 10% and 13% of its variation respectively when included independently in the lineal models. The complexity of fire patch increased rapidly between 0-10% of tree cover (high slope), while this increase was lower between 10 and 30% (lower slope) (Figure 77B). We found few areas above 35% of tree cover. The contribution of the inclusion of the GFED regions in the models was very low, indicating that the differences between regions were less significant.

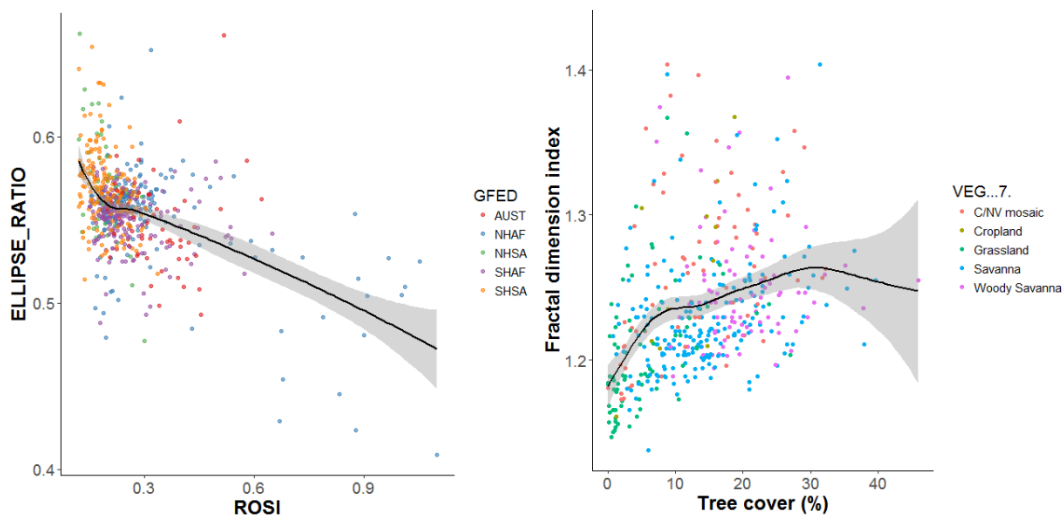


**Figure 77:** A. Relationship between ellipse ration and ROSI. B. Fractal dimension index variation in function of tree cover percent.



## 6. Conclusion

The first global fire patch databases were generated using the data from MERIS and MODIS sensors and a regional one for Northern Hemisphere Africa from SENTINEL-2 data. This was done by using a flood-fill algorithm to reconstruct the fire patches, and by extracting different pixel-level statistics. A standard deviation ellipse was also computed to assess the orientation of the fire patches and for further benchmarking of fire modules.

The FireCCI41 and MCD64A1 collection 6 pixel level products were evaluated at the continental level in North America (boreal and temperate biomes), in a novel approach capturing the morphological features of fire patches, as indicators of fire spread processes to be used and modelled in DGVMs. The conclusion is that the continental variations in the diversity of fire types seem to be conserved with the global remote sensing products when compared to local forest services. However, missing fires in the central plains, and systematic bias in some trait values (fire size and elongation) were observed for the Boreal part of the continent, a similar result to what was obtained for Brazilian savannas. The hypothesis on the conservation of fire morphological features in the products is then partially fulfilled. We believe the continental pattern to be conserved, so empirical relationship between fire shape types and environmental variables can be extracted. But still, biases in some traits (fire size and elongation) do exist and should be quantified for better model benchmarking.

Following the same trait-based approach used in North America, FireCCI41 and MCD64A1 collection 6 were intra and inter compared. From the intra comparison, we can conclude that even if the global pattern is conserved across the cut-offs, they may have a higher impact by regions. From the inter comparison, we can conclude that the diversity of both products matched better when using medium-high cut-offs, and smaller for the dispersion of fires patches. Therefore, the selection of cut-offs should be based on the goal of the study. When the goal is to explore the global major variability, extreme cut-offs should be selected. When the goal is to study the global patterns, the cut-offs that better matched both products can be considered with more certainty.

An inter-comparison at global scale was performed between the fire patch databases obtained from MCD45A1 collection 5.1, MCD64A1 collection 6, FireCCI41, FireCCI50 and FireCCI51. The level of agreement between all the products is good: the density of individual fire events and the power law distribution of fire size indicates that the thinner the resolution, the better the ability of the product to detect small fire events. The only exception arises from some differences in South America where MERIS images are missing, and from Sahel and central Asia. The higher spatial resolution of the Fire\_cci products also allows reconstructing fire patches with higher shape complexity. Nevertheless, the structure of fire size was well-conserved between the two surveys, and the fire patch complexity is similar between the global products up to a normalization factor. We obtained similar results with FireCCI50 and FireCCI51. However, for the FireCCI51 product, we noticed that the areas where MCD64A1 still detect more fire patches are strongly reduced, and that the fire size distribution for larger fires are in much better agreement than for FireCCI41 and FireCCI50. It was also shown that, even if the value of the cut-off modifies the geometric features of the fire patches, its effect was much smaller than the differences between different global datasets.

	<b>Fire_cci</b> <b>Climate Assessment Report</b>		Ref.:	Fire_cci_D5.1_CAR_v1.4	
			Issue	1.4	Date
					Page

The first maps of fire morphological traits using the high spatial resolution FireCCISFD10 BA product for Northern Hemisphere Africa were also provided. For the SFD derived fire patch database, the slope of the power law is steeper in agricultural regions, which means that the FireCCISFD10 detects a higher number of small fires than in other regions. This is expected since agricultural fires are usually small and controlled fires. The FireCCISFD10 BA product also exhibits a clear anti-correlation between the elongation of the fire patch and the fire patch complexity. A comparison with MCD64A1 was performed, but the limited time series covered by the SFD data and the necessity to restrain the comparison to fires big enough to be detected by MCD64A1 render difficult the comparison with MCD64A1. The results are however very encouraging, with the FireCCISFD10 product being able to detect more small fire patches than MCD64A1, and to reconstruct accurate fire patch perimeters. The derived fire patch databases can be used to go beyond BA for the benchmarking of fire modules, which are able to separate fire ignition from fire propagation.

The last part of the report was centred on the research of potential drivers of fire patch morphology using the FireCCI41, FireCCI50, FireCCI51 and MCD64A1-derived fire patch database. First, correlation between fire size and fire intensity (from MCD14ML) was investigated. We showed that fire size followed a humped relationship with fire intensity for equatorial and tropical biomes. Fire size and fire intensity are proportional only for small/less intense fires. This suggests that large fire size is limited, probably by landscape fragmentation. Most DGVMs are able to reduce BA at the end of the fire season through limitation of available fuel, but they usually do not account explicitly for landscape fragmentation. Such an effect can impact the seasonality of predicted BA, and it should be included in most DGVMs. Using NCEP data, it could be seen that fire size tends to decrease with high wind speed: this effect is not yet accounted for in fire modules. However, it was not possible to find any correlation between fire orientation and wind orientation, but this can originate from the low accuracy of the NCEP data. All these results are very encouraging since they proved that the global fire patch databases can be used to investigate drivers for fire patch morphology at a global scale.

## 7. References

- Albini, F.A. 1976. Computer-based models of wildland fire behaviour. An user's manual. Ogden (UT): US Forest Service.
- Alexander, M.E. Estimating the length-to-breadth ratio of elliptical forest fire patterns. pp. 287-304 Proc. 8th Conf. Fire and Forest Meteorology, 1985.
- Archibald, S., Lehmann, C.E.R., Gómez-Dans, J.L. & Bradstock, R.A. Defining pyromes and global syndromes of fire regimes. Proceedings of the National Academy of Sciences of the United States of America, 110, 6442–7, 2013.
- Bak, P.; Tang, C.; Wiesenfeld, K. Self-organized criticality: An explanation of the 1/f noise. Phys. Rev. Lett 59(4), 381-384, 1987.
- Barros, A. M. G.; Pereira, J.M.C.; Lund U.J. Identifying geographical patterns of wildfire orientation: A watershed-based analysis. Forest Ecology and Management, 264:98 - 107, 2012.
- Barros A. M. G.; Pereira, J. M. C.; Moritz, M. A.; Stephens, S. L. Spatial characterization of wildfire orientation patterns in California. Forests, 4(1):197–217, 2013.
- Bond, W. J.; Woodward, F. I. ; Midgley, G. F. The global distribution of ecosystems in a world without fire. New Phytologist, 165(2):525–538, 2005.

	<b>Fire_cci</b> <b>Climate Assessment Report</b>	Ref.:	Fire_cci_D5.1_CAR_v1.4		
		Issue	1.4	Date	16/11/2018
				Page	71

- Bond-Lamberty, B. ; Peckham, S. D. ; Ahl, D. E. ; Gower, S. T. Fire as the dominant driver of central Canadian boreal forest carbon balance. *Nature*, 450:89–92, November 2007.
- Burgan, R.E.; Rothermel, R.C. 1984. BEHAVE: fire behaviour prediction and fuel modelling system. Ogden (UT): US department of Agriculture, Forest Service.
- Cary, G.J.; Keane, R.E.; Gardner, R.H.; Lavorel, S.; Flannigan, M.D.; Davies, I.D.; Li, C.; Lenihan, J.M.; Rupp, T.S.; Mouillot, F. Comparison of the sensitivity of landscape-fire-succession models to variation in terrain, fuel pattern and climate. *Landscape Ecology* 21, 121–137, 2006.
- Chuvieco, E.; Yue, C.; Heil, A.; Mouillot, F.; Alonso-Canas, I.; Padilla, M.; Pereira, J. M.; Oom D.; Tansey, K. A new global burned area product for climate assessment of fire impacts. *Global Ecology and Biogeography* 25(5), 619-629, 2016.
- Clar, S.; Drossel, B. ; Schenk, K. ; Schwabl, F. Self-organized criticality in forest-fire models. *Physica A: Statistical Mechanics and its Applications*, 266(1–4), 153 – 159, 1999.
- Ellis, E.C., Klein Goldewijk, K., Siebert, S., Lightman, D. & Ramankutty, N. Anthropogenic transformation of the biomes, 1700 to 2000. *Global Ecology and Biogeography*, 19, no-no, 2010.
- DiMiceli, C.M., Carroll, M.L., Sohlberg, R.A., Huang, C., Hansen, M.C. & Townshend, J.R.G. Annual Global Automated MODIS Vegetation Continuous Fields (MOD44B) at 250 m Spatial Resolution for Data Years Beginning Day 65, 2000 - 2010, Collection 5 Percent Tree Cover, University of Maryland, College Park, MD, USA, 2011.
- Friedl, M.A., Sulla-Menashe, D., Tan, B., Schneider, A., Ramankutty, N., Sibley, A. & Huang, X. MODIS Collection 5 global land cover: Algorithm refinements and characterization of new datasets. *Remote Sensing of Environment*, 114, 168–182, 2010.
- Giglio, L., Csiszar, I., and Justice, C. O.: Global distribution and seasonality of active fires as observed with the Terra and Aqua MODIS sensors. *Journal of Geophysical Research*, 111, G02016, doi:10.1029/2005JG000142, 2006
- Giglio, L.; Loboda, T.; Roy, D. P.; Quayle B.; Justice, C. O. An active-fire based burned area mapping algorithm for the MODIS sensor. *Remote Sensing of Environment*, 113(2):408 – 420, 2009.
- Giglio, L.; Randerson, J. T.; van der Werf, G. R. Analysis of daily, monthly, and annual burned area using the fourth-generation global fire emissions database (GFED4). *Journal of geophysical research: Biogeosciences*, vol. 118, 317–328, doi:10.1002/jgrg.20042, 2013.
- Giglio, L., Schroeder, W., Justice, C.O. The collection 6 MODIS active fire detection algorithm and fire products. *Remote Sensing of Environment* 178, 31-41, 2016
- Giglio, L., Randerson, J.T., van der Werf, G.R., Kasibhatla, P.S., Collatz, G.J., Morton, D.C. & DeFries, R.S. Assessing variability and long-term trends in burned area by merging multiple satellite fire products. *Biogeosciences*, 7, 1171–1186, 2010.
- Hantson, S.; Pueyo, S.; Chuvieco, E. Global fire size distribution is driven by human impact and climate. *Global Ecology and Biogeography*, 24(1), 77–86, 2015.
- Hantson, S.; Arneeth, A.; Harrison, S. P.; Kelley, D. I.; Prentice, I. C.; Rabin, S. S.; Archibald, S.; Mouillot, F.; Arnold, S. R.; Artaxo, P.; Bachelet, D.; Ciais, P.; Forrest, M.; Friedlingstein, P.; Hickler, T.; Kaplan, J. O.; Kloster, S.; Knorr, W.; Lasslop, G.; Li, F.; Mangeon, S.; Melton, J. R.; Meyn, A.; Sitch, S.; Spessa, A.;

	<b>fire</b> <b>cci</b>	<b>Fire_cci</b> <b>Climate Assessment Report</b>		Ref.:	Fire_cci_D5.1_CAR_v1.4	
		Issue	1.4	Date	16/11/2018	
				Page	72	

- van der Werf, G. R.; Voulgarakis, A.; Yue, C. The status and challenge of global fire modelling. *Biogeosciences*, 13(11):3359–3375, 2016.
- Lasslop, G.; Hantson, S.; Kloster S. Influence of wind speed on the global variability of burned fraction: a global fire model's perspective. *International Journal of Wildland Fire*, 24(7), 989-1000. 10.1071/WF15052, 2015.
- Laurent, P., Mouillot, F., Yue, C., Ciais, P., Moreno, M.V., and Nogueira, J.M. FRY, a global database of fire patch functional traits derived from space-borne burned area products. *Scientific data*, 5, p.180132, 2018.
- Levine, N. Crimestat III: A spatial statistics program for the analysis of crime incident locations (version 3.3). Ned Levine and Associates: Houston TX/ National Institute of Justice: Washington, DC, 2010.
- Loepfe L.; Rodrigo, A.; Lloret, F. Two thresholds determine climatic control of forest fire size in Europe and Northern Africa. *Regional Environmental Change*, 14(4), 1395–1404, 2014.
- Magi, B. I., S. Rabin, E. Shevliakova, and S. Pacala. Separating Agricultural and Non-Agricultural Fire Seasonality at Regional Scales. *Biogeosciences* 9, no. 8: 3003–12, doi: 10.5194/bg-9-3003-2012, 2012.
- Malamud, B. D.; Morein, G.; Turcotte, D. L. Forest fires: An example of self-organized critical behavior. *Science*, 281(5384), 1840–1842, 1998.
- Mason, N. W. H.; Mouillot, D.; Lee, W. G.; Bastow Wilson, J. Functional richness, functional evenness and functional divergence: The primary components of functional diversity. *Oikos* 111(1), 112 – 118, 2005.
- McGarigal, K. and Marks, B.J. FRAGSTATS: spatial pattern analysis program for quantifying landscape structure, Gen. Tech. Rep. PNW-GTR-351. Portland, OR: U.S. Department of Agriculture, Forest Service, Pacific Northwest Research Station. 122 p., 1995.
- Mouillot, F.; Schultz, M. G.; Yue, C.; Cadule, P.; Tansey, K.; Ciais, P.; Chuvieco, E. Ten years of global burned area products from spaceborne remote sensing—a review: Analysis of user needs and recommendations for future developments. *International Journal of Applied Earth Observation and Geoinformation*, 26:64 – 79, 2014.
- Nogueira, J.M.P.; Ruffault, J.; Chuvieco, E.; Mouillot, F. Can we go beyond burned area in the assessment of global remote sensing products with fire patch metrics? *Remote Sensing*, 9(1), 7, 2016.
- Oliva, P.; Martín, P.; Chuvieco, E. Burned area mapping with meris post-fire image. *International Journal of Remote Sensing*, 32(15), 4175–4201, 2011.
- Oliveira, S.L.J.; Campagnolo, M.L.; Price, O.F.; Edwards, A.C.; Smith, J.R.; Pereira, J.M.C. Ecological implications of fine scale fire patchiness and severity in tropical savannas of northern Australia. *Fire Ecol.* 11, 10–31, 2015.
- Oom D.; Silva, P.C.; Bistinas, I.; Pereira, J.M.C. Highlighting biome specific sensitivity of fire size distributions to time-gap parameters using a new algorithm for fire event individuation. *Remote Sensing*, 8(8), 663, 2016.
- Pueyo, S. Self-organised criticality and the response of wildland fires to climate change. *Climatic Change*, 82(1), 131–161, 2007.
- Ramo, R.; Heil, Angelika; Chuvieco, E. ESA CCI ECV Fire Disturbance: D4.1.3 Product Intercomparison Report (PIR), version 1.4. 2014. Available at: <http://www.esa-fire-cci.org/documents>





- Román-Cuesta, R. M.; Gracia, M.; Retana, J. Factors influencing the formation of unburned forest islands within the perimeter of a large forest fire. *Forest Ecology and Management*, 258(2), 71 – 80, 2009.
- Rothermel, R. C. A mathematical model for predicting fire spread in wildland fuels. USDA Forest Services. Research Paper INT-115, 1972.
- Roy, D.P.; Boschetti, L.; Justice, C.O.; Ju, J. The collection 5 MODIS burned area product - Global evaluation by comparison with the MODIS active fire product. *Remote Sensing of Environment* 112, 3690–3707, 2008.
- Schleuter, D.; Daufresne, M.; Massol, F.; Argillier, C. A user's guide to functional diversity indices. *Ecological Monographs* 80(3), 469-484, 2010.
- Sedano, F. and Randerson, J. T.: Multi-scale influence of vapor pressure deficit on fire ignition and spread in boreal forest ecosystems. *Biogeosciences* 11, 3739–3755, 2014.
- Thonicke, K. et al. The influence of vegetation, fire spread and fire behaviour on biomass burning and trace gas emissions: results from a process-based model. *Biogeosciences* 7, 1991–2011, 2010.
- van der Werf, G. R.; Randerson, J. T.; Giglio, L.; Collatz, G. J.; Mu, M.; Kasibhatla, P. S.; Morton, D. C.; DeFries, R. S.; Jin, Y.; van Leeuwen, T. T. Global fire emissions and the contribution of deforestation, savanna, forest, agricultural, and peat fires (1997–2009). *Atmospheric Chemistry and Physics*, 10(23):11707–11735, 2010.
- Villéger, S.; Mason, N. W. H.; Mouillot, D. New multidimensional functional diversity indices for a multifaceted framework in functional ecology. *Ecology*, 89(8), 2290-2301, 2008.
- Villéger S.; Grenouillet, G.; Brosse, S. Decomposing functional beta-diversity reveals that low functional b-diversity is driven by low functional turnover in European fish assemblages. *Global Ecol. Biogeogr.* 22, 671–681, 2013.
- Viovy, N. CRUNCEP Version 7 - Atmospheric Forcing Data for the Community Land Model, 2018.
- Wooster, M. J., Roberts, A. F., Perry, G. L. W. and Kaufman, Y. J.: Retrieval of biomass combustion rates and totals from fire radiative power observations: FRP derivation and calibration relationships between biomass consumption and fire radiative energy release. *Journal of Geophysical Research* 110, 2005.
- Wooster, M. J., Roberts, G., Smith, A. M. S., Johnston, J., Freeborn, P., Amici, S. and Hudak, A. T.: Thermal Remote Sensing of Active Vegetation Fires and Biomass Burning Events. *Thermal Infrared Remote Sensing*. C. Kuenzer and S. Dech, Springer Netherlands. 17:347-390, 2013.
- Yue, C. et al. Modelling the role of fires in the terrestrial carbon balance by incorporating SPITFIRE into the global vegetation model ORCHIDEE – Part 1: simulating historical global burned area and fire regimes. *Geosci. Mod. Development* 7, 2747–2767, 2014.



## 8. Annex 1: Acronyms and abbreviations

A	Patch Surface Area (m <sup>2</sup> )
AUST	Australia
BA	Burned Area
BD	Burned Date
BOAS	Boreal Asia
BONA	Boreal North America
β-div	β-diversity
CA	Patch core area (m <sup>2</sup> )
CAR	Climate Assessment Report
CCI	Climate Change Initiative
CEAM	Central America
CEAS	Central Asia
CMUG	Climate Modelling User Group
CNFD	Canadian National Fire Database
CRAN	Comprehensive R Archive Network
CWFIS	Canadian Wildland Fire Information System
DGVM	Dynamic Global Vegetation Model
E	Eccentricity
ECV	Essential Climate Variables
ESA	European Space Agency
EQAS	Equatorial Asia
EURO	Europe
FD	Fractal Dimension
FDis	Functional Dispersion
FDiv	Functional Divergence
FEve	Functional Evenness
FI	Fire intensity
FOri	Functional Originality
FRic	Functional Richness
FRP	Fire Radiative Power
FS	Fire Size
FSpe	Functional Specialization
GAM	Generalized Additive Models
GAMM	Generalized Additive Mixed Models
GeoMAC	Geospatial Multi-Agency Coordination
GFED4	Global Fire Emissions Database 4
GLS	Generalized Least Square
ID	Individual Burned Patches
LC_cci	CCI Land Cover project



fire  
cci

**Fire\_cci**  
**Climate Assessment Report**

Ref.: Fire\_cci\_D5.1\_CAR\_v1.4

Issue 1.4 Date 16/11/2018

Page 75

MCD45A1	MODIS Collection 5 Burned Area Product
MCD64A1	MODIS Collection 6 Burned Area Product
MERIS	Medium Resolution Imaging Spectrometer
MIDE	Middle East
MODIS	Moderate Resolution Imaging Spectroradiometer
mSD	Mean Square Deviation
NCEP	National Centers for Environmental Prediction
Nest	Functional Nestedness
NHAF	Northern Hemisphere Africa
NHSA	Northern Hemisphere South America
P	Patch Perimeter (m)
PCoA	Principal Coordinates Analysis
RGB	Red-Green-Blue
ROSL	Rate of spread linear along the longest ellipse axis
SDE	Standard Deviation Ellipse
SEAS	Southern Asia
SFD	Small Fire Dataset
SHAF	Southern Hemisphere Africa
SHSA	Southern Hemisphere South America
SI	Shape Index
SOC	Self-organised Criticality
TENA	Temperate North America
TO	Tocantin State, Brazil.
Turn	Functional Turnover
UTM	Universal Transverse Mercator
US	United States
VCF	Vegetation Continuous Fields
WGS84	World Geodetic System 1984
WRS2	Worldwide Referencing System 2